# Development of biosensor systems for the detection of anti-cancer drugs and prostate cancer

A thesis submitted in fulfilment of the requirements

for the degree of

**DOCTOR OF PHILOSOPHY**

of

**RHODES UNIVERSITY**

By

**DANIEL MWANZA**

**ORCID ID**

**0000-000-030676-3255**

March 2022

**DEDICATIONS**

*Dedicated to my mum, wife and siblings*

**ACKNOWLEDGEMENTS**

Firstly, I would like to thank the Almighty Creator of the universe and they that dwell in it for the blessing of life. I express my lifetime gratitude to my supervisor, Prof. Philani Mashazi. Your hearty efforts to guide and give direction to this scientific journey cannot be thanked enough. Your patience with me and consistent encouragement gave me strength to keep moving forward. Thank you so much for your valuable time you put in reviewing progress reports, manuscripts and this thesis because without your inestimable input this thesis would have not been possible. I am very much thankful to my co-supervisor, Dist. Prof. Tebello Nyokong, for offering me a rare opportunity to work under your supervision. I am grateful for all the time you spared to attend to the needs of my work and for your invaluable holistic support in my growth as an academic.

I wish to extend my gratitude to Prof. Solomon Tesfalidet for all the support you gave me whilst on the exchange program at Umea University. I really learnt a lot from you that has contributed to the successful completion of this thesis. Your humility and kindness gave me hope, not only in science but in life as a whole.

Special thanks to you Sereilakhena Phal for making my stay and work at Umea feel at home. Your help with MATLAB and multivariate data analysis will always be appreciated.

Many thanks to the Institute of Nanotechnology Innovation, DST/Mintek NIC for the Ph.D. scholarship and Sandisa Imbewu for an extension fund.

Many gratitude to my mother, uncle, aunty and my wife for all the support and encouragement. Long life to you all.

I am also thankful to the Rhodes University Chemistry staff and postgraduate students of the chemistry department for all the support.

I acknowledge our nanobiosensor research group for all the helpful discussions during and after presentations. This thesis is a product of those times, thank you.

**ABSTRACT**

Rapid, low-cost and accurate point-of-care analytical devices are highly required for the detection of cancer biomarkers for the early diagnosis and determination of anti-cancer drugs for monitoring of cancer-related diseases. This thesis focused on the development of biosensor systems for the detection of anti-cancer drug, methotrexate (MTX) and prostate cancer biomarker, prostate-specific antigen (PSA).

Ultrasensitive electrochemical immunosensors were fabricated by covalent immobilization of polyclonal anti-MTX and monoclonal anti-PSA antibodies onto glassy carbon, screen-printed carbon and gold electrodes which were pre-modified with isophthalic acid (IPA) thin monolayer film. A methodology based on the steric hindrance by 1,3-substituted aryldiazonium salt was adopted to enable the electrografting of IPA thin monolayer film on electrode surfaces. The antibodies were immobilized onto the IPA thin monolayer film via carbodiimide chemistry to form a sensing or analyte capture surface.

For the detection of MTX, the analytical performance of the non-Faradaic electrochemical impedance spectroscopy (EIS) immunosensor was validated using singular value decomposition (SVD). The non-Faradaic EIS detection of PSA was validated using Nyquist plots of total capacitance, complex capacitance calculated from the imaginary part of impedance, and the capacitance acquired from the circuit fitting.

The detection of PSA was further studied using colorimetric sensing platform which was developed by forming a sandwich immunoassay. For the immunoassay detection, the anti-PSA captured monoclonal antibodies were immobilized onto the microwell plates. The sensing signal was obtained from bioconjugating the anti-PSA antibody polyclonal onto glucose-encapsulating nanoliposomes (GENLs-anti-PSA-pAb). The preparation of glucose - encapsulated nanoliposomes were evaluated for their potential to release glucose in a controlled manner using Triton-X 100 or acidic phosphate buffer saline (PBS, pH 5.0). The detection of PSA (in a sandwich manner) was correlated to the concentration of glucose quantified using horseradish peroxidase (HRP), Pd|PdO nanoparticles, and personal glucose meter.

The immunosensors developed in this work exhibited high stability, selectivity, low detection limits, and a wide linear range which was suitable for screening of both PSA and MTX.

**TABLE OF CONTENT**

## LIST OF ABBREVIATIONS

| | |
|---|---|
| 5-DIPA | 5-Diazonium Isophthalic Acid |
| ACN | Acetonitrile |
| Ag | Silver |
| AuE | Gold Electrode |
| BSA | Bovine Serum Albumin |
| CE | Counter Electrode |
| CHEMS | Cholesterol Hemisuccinate |
| CHO | Cholesterol |
| $C_{nFC}$ | Non-Faradaic Capacitance |
| CV | Cyclic Voltammetry |
| DC | Direct Current |
| DLS | Dynamic Light Scattering |
| DRE | Digital Rectal Exam |
| EIS | Electrochemical Impedance Spectroscopy |
| ELISA | Enzyme-Linked Immuno Assay |
| ERR% | Electro-Reduction Response Percent |
| FTIR | Fourier Transformation Infrared |
| GCE | Glassy Carbon Electrode |
| GENLs | Glucose Encapsulating Nanoliposomes |
| GOx | Glucose Oxidase |
| HRP | Horseradish Peroxidase |
| IPA | Isophthalic Acid |

| | |
|---|---|
| LOD | Limit of Detection |
| LOQ | Limit of Quantification |
| mAb | Monoclonal Antibody |
| MTX | Methotrexate |
| NMR | Nuclear Magnetic Resonance |
| PBS | Phosphate Buffer Solution |
| pAb | Polyclonal Antibody |
| PCa | Prostate Cancer |
| PC | Phosphotyldicholine |
| PGM | Personal Glucose Meter |
| POCT | Point of Care Testing |
| PSA | Prostate-Specific Antigen |
| Pt | Platinum |
| RE | Reference Electrode |
| RMSD | Root Mean Square Deviation |
| RR% | Relative Response Percent |
| SVD | Singular Value Decomposition |
| $TBABF_4$ | Tetrabutylammoniumtetraflouroborate |
| TEM | Transmission Electron Microscopy |
| TMB | 3,3',5,5'-Tetramethylbenzidine |
| UV-vis | Ultraviolet-Visible Spectroscopy |
| WE | Working Electrode |
| XPS | X-ray Photoelectron Spectroscopy |

**LIST OF FIGURES**

## LIST OF TABLES

## LIST OF SCHEMES

## LIST OF PUBLICATION

Here is a list papers published or submitted for publication from this thesis and therefore will not be cited further:

1. **Daniel Mwanza**, Sereilakhen Phal, Tebello Nyokong, Solomon Tesfalidet, Philani Mashazi. Electrografting of isophthalic acid monolayer and covalent attachment of antibody onto carbon surfaces: Construction of capacitive biosensor for methotrexate detection. Electrochimica Acta 398 (2021) 139360.
   *Daniel contribution: Conceptualization, method development, data collection and analysis, writing of original manuscript.*
2. **Daniel Mwanza**, Omotayo Adeniyi, Solomon Tesfalidet, Tebello Nyokong, Philani Mashazi. Label-free Capacitive Immunosensor Based on a Stable Thin-film Monolayer of Isophthalic Acid for Detection of Prostate-Specific Antigen. **(In press).**
   *Daniel contribution: Conceptualization, method development, data collection and analysis, writing of original manuscript*
3. **Daniel Mwanza,** Nololo Mfamela, Omotayo Adeniyi, Tebello Nyokong, Philani Mashazi. Ultrasensitive detection of prostate-specific antigen using glucose-encapsulated nanoliposomes anti-PSA polyclonal antibody as detection nanobioprobes. Talanta 245 (2022) 123483.
   *Daniel contribution: Conceptualization, method development data collection and analysis, writing of original manuscript*

Other publications in collaboration during the duration and not in relation to this thesis:

1. O. Adeniyi, O. Nwahara O, **D. Mwanza**, T. Nyokong, P. Mashazi. Nanohybrid electrocatalyst based on cobalt phthalocyanine-carbon nanotube-reduced graphene oxide for ultrasensitive detection of glucose in human saliva. Sensors and Actuators B: 348 (2021) 130723.
2. S. Phal, K. Shimizu, **D. Mwanza,** P. Mashazi, A. Shchukarev, S. Tesfalidet. Electrografting of 4-carboxybenzenediazonium on glassy carbon electrode: The effect of concentration on the formation of mono and multilayers. Molecules, 25 (2020) 4575.

# CHAPTER 1

## 1 Introduction

Rapid, low-cost, and accurate point-of-care testing (POCT) devices for the detection of anti-cancer drugs and cancer biomarkers are highly required for the early diagnosis and monitoring of cancer and related diseases. In recent years, biosensor research has put much effort into the development of POCT devices [1]. POCT is a rapidly developing field involving near-patient, bedside, ancillary, or in-field testing. It enables a wide range of bioanalytes to be tested easily and quickly without the use of laboratory-based equipment or well-trained personnel [2]. Sensors and biosensors-based on electrochemical [3–7] and colorimetric [8–10] detection techniques have attracted great interest in the development of POCT devices. The personal glucose meters (PGMs) [5,11,12], and lateral flow tests (LFTs) [13] are the most successful examples of electrochemical and colorimetric biosensors developed as POCT devices. They can be used for the detection and monitoring of diseases such as prostate cancer and cancer drugs like methotrexate.

Prostate cancer (PCa) is the most frequently diagnosed cancer in men, accounting for about 1.4 million cases and 375,000 death worldwide in 2020 [14]. The detection of PCa at an early stage is vital for effective curative surgery and an improved survival rate. The five-year survival rate of metastatic PCa is less than 30%, while the survival rate is about 98% if detected early [15]. Digital rectum examination (DRE) and quantification of prostate-specific antigen (PSA) levels are the clinically approved methods for screening and diagnosis of PCa. However, the accuracy of DRE depends on the doctor's skill, and it is an invasive method thus making it unsuitable for mass screening of incipient cancer [16]. Also DRE detects the development or presence of a mass or tumour and cannot be used for early stage detection of prostate cancer. The quantification of serum PSA level is the most preferred method for early-stage detection and monitoring of relapse after treatment. It is a less invasive or non-invasive technique compared to DRE. A total PSA level of less than 4.0 $ng.mL^{-1}$ is present in the blood serum of a healthy man [17]. Elevated serological levels of PSA have been correlated with the development of prostate cancer. PSA levels in the diagnostic grey zone range from 4 to 10 $ng.mL^{-1}$ and indicate a 25 - 40% probability of developing prostate cancer. PSA levels greater than 10 $ng.mL^{-1}$ are a conclusive indication of PCa in about 67% of men [18]. Therefore,

monitoring the rate of increase in PSA levels is vital in the clinical diagnosis of PCa. With the emergent of precision medicine, these values may change from one person to the next. This neccessitates the requirement for the development of POCT for mass screening, baseline investigation and quantification of biomarkers. On such a basis, various PSA immunoassay systems, including enzyme-linked immunoassay (ELISA) [19], radioimmunoassay [20], mass spectroscopy [21], fluorescence immunoassay [22], chemiluminescence [23,24], and photoelectrochemical immunoassay [25,26] have been developed for the quantification of serological PSA levels. These methods are quite complicated due to expensive equipment, laborious procedures, long turn-around time, and the requirement of a specialized analyst, which limits their applicability at point-of-care [2]. Therefore, developing a portable POCT device to streamline the diagnostic process and ensure real-time, effective, and efficient patient care is still an unmet need in the clinical management of PCa.

On the other hand, methotrexate (MTX) is used as a first-line drug for the treatment of rheumatoid arthritis and other forms of cancer. It is an effective and relatively affordable drug [27]. However, MTX has been found to cause severe side effects such as gastrointestinal disorders, hepatic dysregulations, dermatitis, hematologic disorders, and nephrotoxicity pneumonitis [28–31]. In chemotherapy, the effective concentration range of MTX is limited to a relatively narrow therapeutic window. At low concentrations, the therapeutic activity toward cancer cells is poor while unacceptable toxicity toward healthy cells is observed at high concentrations. The dosage of MTX and its level in the blood needs to be regularly controlled and individualized to establish the dose-response and side effects [30]. This is an area that will be attractive towards personalized or precision medicine. There is therefore high demand for rapid and highly sensitive methods for monitoring MTX in real-time and online. Today, the measurement of MTX in blood samples is often conducted using techniques such as high-performance liquid chromatography (HPLC) [32], oxidative fluorimetry [33], electrospray ionization tandem mass spectroscopy (ESI-MS) [34], and capillary electrophoresis (CE) [35]. These techniques offer high accuracy, sensitivity, and selectivity, but they require highly skilled and trained personnel, a lot of biological samples, bulky instrumentation, and tedious sample preparation. This makes these techniques not amenable for on-site or POCT applications. Electrochemical and colorimetric biosensors have been known to be simple, portable, affordable, and can easily be mass produced for POCT applications.

Amongst the various electrochemical methods, electrochemical impedance spectroscopy (EIS) has emerged as a promising technique for biosensor development [36]. EIS offers the

possibility for the development of relatively cheap capacitive biosensors that can be miniaturized and used for in-situ analysis. Impedimetric biosensors are either Faradaic or non-Faradaic [3]. The Faradaic impedimetric biosensor comprises a redox probe (label) while the non-Faradaic impedimetric biosensors are label-free and may not need a reference electrode for potential monitoring. The biosensors that are based on non-Faradaic EIS are used to monitor the capacitive behaviour of the electrode in the presence of the biomolecule of interest [37]. Capacitive EIS biosensors are mostly affinity-based sensors, hence attractive for their ability to detect analytes at ultra-low concentrations with high selectivity and sensitivity without a need for sample pre-treatment [37,38]. Their construction involves the immobilization of the recognition or capture biomolecules as sensing elements on an electrode surface where dielectric changes are measured when an analyte bind (affinity). The challenges faced with the design of capacitive biosensorsare the immobilization of the recognition biomolecules onto the electrode surface in an oriented manner [37,39] for enhanced analyte interaction, and the relatively small capacitance changes after the binding of the target molecule [4]. These challenges can be solved by the formation of stable thin film as the anchoring blocks for immobilization of the recognition or capture biomolecule and the application of suitable data analysis tools.

Meanwhile, the colorimetric biosensors detect and monitor bioanalytes through color development as the target analytes interact with capture bioprobes [40]. The color intensity can be observed with the naked eye for presumptive diagnosis or the concentration of the target analyte can be quantified by using low-cost portable spectrophotometers. Conventional colorimetric biosensors are usually constructed based on enzyme catalyzed reactions to produce colored products from clear coloured substrates. For example, horseradish peroxidase (HRP) conjugated onto a detecting antibody used in sandwich immunoassay oxidizes a chromogenic substrate such as 3,3',5,5'-tetramethylbenzidine (TMB) into blue colored oxidation products confirming the presence of the target analyte [41]. The colorimetric biosensor are easy to use, can be produced at low-cost, and are highly portable [13,42]. However, the use of natural enzymes, such as horseradish peroxidase and alkaline phosphatase (ALP) enzymes make the cost of production high and has reduced stability in harsh conditions as it denatures easily. This makes a demand for the development of highly stable, sensitive enzyme-mimicking inorganic probes very attractive. Nanomaterials with enzyme mimicking activity have been shown to improve the development of colorimetric biosensors and these

materials have been reported to show high sensitivity, improved stability, and can be produced at a very low cost.

## 1.1 Aim

The overarching aim of this thesis was to develop biosensor systems that can detect methotrexate (MTX) as anti-cancer drugs in a complex sample matrix and prostate-specific antigen (PSA) as prostate cancer biomarker selectively and sensitively.

The specific aims were:

(a) To develop a label-free capacitive immunosensor by modifying carbon and screen-printed carbon electrode with a stable and electrografted thin monolayer film of isophthalic acid, and
(b) To immobilize anti-MTX monoclonal antibody as capture protein for non-Faradaic EIS detection of anti-cancer drug (MTX).

The specific objectives to achieve the above aims were to:

(i) Fabricate a controlled ultra-thin film of isophthalic acid by electrografting 5-diazonium isophthalic acid on the glassy carbon, and screen-printed carbon electrode surfaces.
(ii) Characterize the grafted IPA thin film and the immobilization of anti-MTX antibody monolayer using various surface sensitive techniques, such as cyclic voltammetry (CV), electrochemical impedance spectroscopy (EIS), and X-ray photoelectron spectroscopy (XPS).
(iii) Construct and evaluate the detection of MTX using the ultrasensitive non-Faradaic capacitance immunosensor.
(iv) Evaluate the analytical performance of the non-Faradaic impedimetric immunosensor towards the detection of MTX using singular value decomposition (SVD) for MTX and total capacitance and complex capacitance.
(v) Study the mechanism of interaction of the anti-MTX antibody with MTX using computational molecular dynamics (MD).

(c) To fabricate a label-free capacitive immunosensor based on a stable thin-film monolayer of isophthalic acid onto gold electrode.

(d) To immobilize anti-PSA monoclonal antibody for non-Faradaic EIS detection of PSA.

The specific objectives to achieve this first aims were to:

(i) Fabricate a controlled ultra-thin film of isophthalic acid (IPA) on the gold electrode surface using electrografting of 5-diazonium isophthalic acid and immobilization of anti-PSA monoclonal antibody via carbodiimide coupling chemistry.

(ii) Characterize the electrografted IPA monolayer using surface sensitive techniques such as cyclic voltammetry (CV), electrochemical impedance spectroscopy (EIS), and X-ray photoelectron spectroscopy (XPS).

(iii) Evaluate the analytical performance of the fabricated immunosensor towards ultrasensitive non-Faradaic capacitance detection of PSA.

(iv) Evaluate the analytical performance of the non-Faradaic impedimetric immunosensor towards the detection of PSA using total capacitance, complex capacitance, and double layer capacitance from circuit fitting for PSA detection.

(e) To develop an ultrasensitive comparative detection of PSA using glucose-encapsulated nanoliposomes (GENLs) bioconjugated with anti-PSA polyclonal antibody nanobioprobes.

The specific objectives to achieve the aim above were to:

(i) Prepare glucose-encapsulating nanoliposomes (GENLs) as nanobioprobes for enhanced signal transduction.

(ii) Characterize the prepared nanoliposomes using various analytical techniques for their morphology, size and amount of glucose encapsulated.

(iii) Use personal glucose meters (PGMs), horseradish peroxidase (HRP) and glucose oxidase (GOx) bienzymes, and Pd|PdO nanoparticles-glucose oxidase for the detection of PSA.

(iv) Compare the analytical performance of HRP-GOx bienzymes and palladium (Pd|PdO) noparticles, and PGM as transduction methods towards the detection of PSA using GENLs as nanobioprobes.

## 1.2 Thesis outline

This thesis has seven chapters with the first chapter comprising of the general introduction while the second chapter gives the background and literature review of the study. Chapter three to five are based on the scientific contribution of this thesis while chapter six is on the discussion of the results and findings of the thesis. The seventh chapter comprises of the conclusions of the thesis and future perspectives.

A brief thesis outline is as follows:

**Chapter 1: Introduction**

This chapter describes the importance of monitoring prostate-specific antigen (PSA) as a prostate cancer biomarker and methotrexate (MTX) as the model analyte for monitoring anti-cancer drugs. The chapter also highlights the current challenges faced by the systems currently used in the diagnosis of prostate cancer using prostate-specific cancer and the monitoring and management of anti-cancer drugs during treatment of cancer using MTX as a chemotherapeutic agent. This chapter further proposes possible solutions to the current methods as the identified niche area of research investigated in this thesis. Lastly, this chapter gives the outline of the thesis chapters and highlights of the aims and objectives of the study.

**Chapter 2: Literature review**

Chapter two provides the background for the detection and monitoring of PCa and MTX. It highlights the progress in the development of electrochemical impedance spectroscopy-based biosensors, the challenges and possible solutions. The chapter further highlights the current trends in the development of biosensing platforms for both MTX and PSA. The chapter also gives a brief background on the use of nanomaterials and nanobioprobes for the development of colorimetric biosensors.

**Chapter 3: Electrografting of isophthalic acid monolayer and covalent attachment of antibody onto carbon surfaces: construction of capacitive biosensor for methotrexate detection**

In chapter three, 5-diazonium isophthalic acid was successfully synthesized and electrografted onto glassy carbon (GCE) and screen-printed carbon (SPCE) electrodes. SPCE was used to demonstrate the fabrication of a miniature device and to compare it with a conventional GCE.

Chapter three further shows how isophthalic acid (IPA) electrografted thin film was used for the immobilization of polyclonal anti-methotrexate antibodies using carbodiimide activation chemistry to form antibody modified surfaces, GCE-IPA-anti-MTX-pAb and SPCE-IPA-anti-MTX-pAb. The non-ionic blocking polymer (BP) used for blocking the non-specific binding site was *N*-[tris(hydroxymethyl) methyl]-acrylamide polymer. The GCE-IPA-anti-MTX-pAb/BP and SPCE-IPA-anti-MTX-pAb/BP surfaces were used as capacitive biosensors for the detection of MTX in phosphate buffer pH 7.4 using electrochemical impedance spectroscopy (EIS). Finally, chapter three describes how the non-Faradaic EIS data was analyzed using singular value decomposition (SVD).

**Chapter 4: Label-free capacitive immunosensor based on a stable thin-film monolayer of isophthalic acid for detection of prostate-specific antigen**

Chapter four describes the design and development of a label-free capacitive immunosensor based on a stable thin film of isophthalic acid and covalent immobilization of monoclonal anti-PSA antibody for the detection of PSA. A methodology based on the steric hindrance of 1,3-substituted aryldiazonium salt was adopted so as to try and control the growth of the IPA thin film on the gold electrode surface. The chapter also reports the analytical performance of the developed sensor validated using Nyquist plots of capacitance generated from the complex impedance data; complex capacitance calculated from the imaginary part of the impedance plotted against the log of frequency; and capacitance as the double layer capacitance from the circuit fitting.

**Chapter 5: Ultrasensitive detection of PSA using glucose-encapsulated nanoliposomes bioconjugated with anti-PSA polyclonal antibody as detection nanobioprobes**

This chapter reports on the preparation and characterization of glucose encapsulating nanoliposomes, their pH sensitivity, and control release, and their use for the detection of PSA. The preparation of glucose-encapsulated nanoliposomes using different lipid compositions to obtain the ideal monodispersed liposomes is discussed. In addition, the preparation and characterization of palladium (Pd|PdO) nanoparticles and their application as peroxidase mimetics (nanozymes) for the colorimetric detection of PSA was also reported. Controlled release of encapsulated glucose was investigated using acidic pH or surfactant solutions. The chapter also describes the detection of PSA by correlating the concentration of the encapsulated glucose detected using HRP-GOx bienzymes, Pd|PdO nanoparticles, and personal glucose

meter (PGM). The advantages and disadvantages of each of the detection method were discussed.

**Chapter 6: Discussion**

This chapter will discuss the summary the major findings of the results of the thesis. It further describes the differences of the various methods used for the detection and the major findings of the thesis.

**Chapter 7: Conclusions and future perspectives**

This chapter reports on the conclusions arrived at in this thesis and highlights the future perspectives.

## 1.3 References


[1] P.B. Luppa, C. Müller, A. Schlichtiger, H. Schlebusch, Point-of-care testing (POCT): Current techniques and future perspectives, TrAC - Trends Anal. Chem. 30 (2011) 887–898.

[2] W. Jung, J. Han, J.W. Choi, C.H. Ahn, Point-of-care testing (POCT) diagnostic systems using microfluidic lab-on-a-chip technologies, Microelectron. Eng. 132 (2014) 46–57.

[3] R.A. Dorledo de Faria, L.G. Dias Heneine, T. Matencio, Y. Messaddeq, Faradaic and non-Faradaic electrochemical impedance spectroscopy as transduction techniques for sensing applications, Int. J. Biosens. Bioelectron. 5 (2019) 29–31.

[4] J.S. Daniels, Label-free impedance biosensors: opportunities and challenges, Electroanalysis. 19 (2008) 1239–1257.

[5] J. Tang, Y. Huang, H. Liu, C. Zhang, D. Tang, Novel glucometer-based immunosensing strategy suitable for complex systems with signal amplification using surfactant-responsive cargo release from glucose-encapsulated liposome nanocarriers, Biosens. Bioelectron. 79 (2016) 508–514.

[6] J. Cecchetto, F.C.B. Fernandes, R. Lopes, P.R. Bueno, The capacitive sensing of NS1 Flavivirus biomarker, Biosens. Bioelectron. 87 (2017) 949–956.

[7] A. Ebrahimi, P. Dak, E. Salm, S. Dash, S. V. Garimella, R. Bashir, M.A. Alam, Nanotextured superhydrophobic electrodes enable detection of attomolar-scale DNA

concentration within a droplet by non-Faradaic impedance spectroscopy, Lab Chip. 13 (2013) 4248–4256.

[8] R. Guo, Y. Wang, S. Yu, W. Zhu, F. Zheng, W. Liu, D. Zhang, J. Wang, Dual role of hydrogen peroxide on the oxidase-like activity of nanoceria and its application for colorimetric hydrogen peroxide and glucose sensing, RSC Adv. 6 (2016) 59939–59945.

[9] Y. Tao, M. Li, B. Kim, D.T. Auguste, Incorporating gold nanoclusters and target-directed liposomes as a synergistic amplified colorimetric sensor for HER2-positive breast cancer cell detection, Theranostics. 7 (2017) 899–911.

[10] R. Ren, G. Cai, Z. Yu, D. Tang, Glucose-loaded liposomes for amplified colorimetric immunoassay of streptomycin based on enzyme-induced iron (II) chelation reaction with phenanthroline, Sensors Actuators, B Chem. 265 (2018) 174–181.

[11] B. Lin, D. Liu, J. Yan, Z. Qiao, Y. Zhong, J. Yan, Z. Zhu, T. Ji, C.J. Yang, Enzyme-Encapsulated Liposome-Linked Immunosorbent Assay Enabling Sensitive Personal Glucose Meter Readout for Portable Detection of Disease Biomarkers, ACS Appl. Mater. Interfaces. 8 (2016) 6890–6897.

[12] J. Joo, D. Kwon, H.H. Shin, K.H. Park, H.J. Cha, S. Jeon, A facile and sensitive method for detecting pathogenic bacteria using personal glucose meters, Sensors Actuators, B Chem. 188 (2013) 1250–1254.

[13] M. Pohanka, Point-of-Care Diagnoses and Assays Based on Lateral Flow Test, Int. J. Anal. Chem. 2021 (2021) 6685619 (1-9).

[14] H. Sung, J. Ferlay, R.L. Siegel, M. Laversanne, I. Soerjomataram, A. Jemal, F. Bray, Global Cancer Statistics 2020: GLOBOCAN Estimates of Incidence and Mortality Worldwide for 36 Cancers in 185 Countries, CA. Cancer J. Clin. 71 (2021) 209–249.

[15] J.M. Mattsson, S. Ravela, C. Hekim, M. Jonsson, J. Malm, A. Närvänen, U.H. Stenman, H. Koistinen, Proteolytic activity of prostate-specific antigen (PSA) towards protein substrates and effect of peptides stimulating PSA activity, PLoS One. 9 (2014) 1–12.

[16] I.E. Tothill, Biosensors for cancer markers diagnosis, Semin. Cell Dev. Biol. 20 (2009) 55–62.

[17] H. Qi, M. Li, M. Dong, S. Ruan, Q. Gao, C. Zhang, Electrogenerated chemiluminescence peptide-based biosensor for the determination of prostate-specific antigen-based on target-induced cleavage of peptide, Anal. Chem. 86 (2014) 1372–1379.

[18] J. Meehan, M. Gray, C. Mart, C. Kay, D. Mclaren, A.K. Turnbull, Tissue- and Liquid-Based Biomarkers in Prostate Cancer Precision Medicine, J. Pers. Med. 11 (2021) 1–37.

[19] B. Acevedo, Y. Perera, M. Ruiz, G. Rojas, J. Benítez, M. Ayala, J. Gavilondo, Development and validation of a quantitative ELISA for the measurement of PSA concentration, Clin. Chim. Acta. 317 (2002) 55–63.

[20] A.S. Abu-Bakr El-Bayoumy, A.T. Hessien Keshta, K.M. Sallam, N.H. Ebeid, H.M. Elsheikh, B.E.S. Bayoumy, Extraction, purification of prostate-specific antigen (PSA), and establishment of radioimmunoassay system as a diagnostic tool for prostate disorders, J. Immunoass. Immunochem. 39 (2018) 12–29.

[21] E.W. Klee, O.P. Bondar, M.K. Goodmanson, S.A. Trushin, E.J. Bergstralh, R.J. Singh, N.L. Anderson, G.G. Klee, Serum concentrations of prostate-specific antigen measured using immune extraction, trypsin digestion, and tandem mass spectrometry quantification of LSEPAELTDAVK peptide, Arch. Pathol. Lab. Med. 138 (2014) 1381–1386.

[22] M. Kawatani, K. Yamamoto, D. Yamada, M. Kamiya, J. Miyakawa, Y. Miyama, R. Kojima, T. Morikawa, H. Kume, Y. Urano, Fluorescence Detection of Prostate Cancer by an Activatable Fluorescence Probe for PSMA Carboxypeptidase Activity, J. Am. Chem. Soc. 141 (2019) 10409–10416.

[23] S. Gutkin, O. Green, G. Raviv, D. Shabat, O. Portnoy, Powerful Chemiluminescence Probe for Rapid Detection of Prostate-Specific Antigen Proteolytic Activity: Forensic Identification of Human Semen, Bioconjug. Chem. 31 (2020) 2488–2493.

[24] M. Kim, K. Kim, J.H. Lee, A cost-effective and rapid aptasensor with chemiluminescence detection for the early diagnosis of prostate cancer, Microchem. J. 155 (2020) 104763 (1-8).

[25] X.P. Liu, N. Chang, J.S. Chen, C.J. Mao, B.K. Jin, Ultrasensitive photoelectrochemical immunosensor based on a g-$C_3N_4$/$SnS_2$ nanocomposite for prostate-specific antigen detection, Microchem. J. 168 (2021) 106337 (1-10).

[26] Y. Zhang, Y. Liu, R. Li, M. Saddam Khan, P. Gao, Y. Zhang, Q. Wei, Visible-light driven Photoelectrochemical Immunosensor Based on $SnS_2$@mpg-$C_3N_4$ for Detection of Prostate Specific Antigen, Sci. Rep. 7 (2017) 1–8.

[27] M.C.F.J. De Rotte, E. Den Boer, P.H.P. De Jong, S.M.F. Pluijm, M. Bulatović Ćalasan, A.E. Weel, A.M. Huisman, A.H. Gerards, B. Van Schaeybroeck, N.M. Wulffraat, J. Lindemans, J.M.W. Hazes, R. De Jonge, Methotrexate polyglutamates in erythrocytes

are associated with lower disease activity in patients with rheumatoid arthritis, Ann. Rheum. Dis. 74 (2015) 408–414.

[28] G.S. Alarcóan, I.C. Tracy, W.D. Blackburn, Methotrexate in rheumatoid arthritis. Toxic effects as the major factor in limiting long-term treatment, Arthritis Rheum. 32 (1989) 671–676.

[29] M.J.H. Wijnands, M.A. Van't Hof, M.A. Van Leeuwen, M.H. Van Rijswijk, L.B.A. Van De Putte, P.L.C.M. Van Riel, Long-term second-line treatment: A prospective drug survival study, Rheumatology. 31 (1992) 253–258.

[30] A.M. Boerbooms, P.J. Kerstens, J.W. van Loenhout, J. Mulder, L.B. van de Putte, Infections during low-dose methotrexate treatment in rheumatoid arthritis, Semin. Arthritis Rheum. 24 (1995) 411–421.

[31] W. Wang, H. Zhou, L. Liu, Side effects of methotrexate therapy for rheumatoid arthritis: A systematic review, Eur. J. Med. Chem. 158 (2018) 502–516.

[32] H. Li, W. Luo, Q. Zeng, Z. Lin, H. Luo, Y. Zhang, Method for the determination of blood methotrexate by high-performance liquid chromatography with online post-column electrochemical oxidation and fluorescence detection, J. Chromatogr. B Anal. Technol. Biomed. Life Sci. 845 (2007) 164–168.

[33] S. Chen, Z. Zhang, D. He, Y. Hu, H. Zheng, C. He, Flow-injection – electrochemical oxidation fluorimetry for determination of methotrexate, 22 (2007) 338–342.

[34] I. Rodin, A. Braun, A. Stavrianidi, O. Shpigun, A validated LC-MS/MS method for rapid determination of methotrexate in human saliva and its application to an excretion evaluation study, J. Chromatogr. B Anal. Technol. Biomed. Life Sci. 937 (2013) 1–6.

[35] M.C. Roach, P. Gozel, R.N Zare, Determination of methotrexate and its major metabolite, 7-hydroxymethotrexate, using capillary zone electrophoresis and laser-induced fluorescence detection, J. Chromatogr. 426 (1988) 129–140.

[36] T. Bertok, L. Lorencova, E. Chocholova, E. Jane, A. Vikartovska, P. Kasak, J. Tkac, Electrochemical Impedance Spectroscopy Based Biosensors: Mechanistic Principles, Analytical Examples, and Challenges towards Commercialization for Assays of Protein Cancer Biomarkers, Chem.Electro.Chem. 6 (2019) 989–1003.

[37] C. Berggren, B. Bjarnason, G. Johansson, Capacitive biosensors, Electroanalysis. 13 (2001) 173–180.

[38] C. Berggren, B. Bjarnason, G. Johansson, Instrumentation for direct capacitive biosensors, Instrum. Sci. Technol. 27 (1999) 131–140.

[39] M. Prodromidis, Impedimetric Biosensors and Immunosensors, Proc. 2nd Int. Semin. Anal. Sci. 8 (2007) 69–71.

[40] V.X.T. Zhao, T.I. Wong, X.T. Zheng, Y.N. Tan, X. Zhou, Colorimetric biosensors for point-of-care virus detections, Mater. Sci. Energy Technol. 3 (2020) 237–249.

[41] Immunochemistry Technologies LLC, HRP Redox Reaction Driven TMB Color Development, (2020). https://immunochemistry.com/educational-material/hrp-redox-reaction-driven-tmb-color-development/. (Date accessed: 20th December 2021).

[42] C. Fernández-Sánchez, C.J. McNeil, K. Rawson, O. Nilsson, Disposable noncompetitive immunosensor for free and total prostate-specific antigen based on capacitance measurement, Anal. Chem. 76 (2004) 5649–5656.

# CHAPTER 2

## 2 Literature review

This chapter provides the background of biosensing development for the detection and monitoring of prostate cancer biomarker called prostate-specific antigen (PSA) and methotrexate (MTX) as a model anti-cancer drug. It highlights the progress in the development of electrochemical impedance spectroscopy-based biosensors, the challenges, and possible solutions towards the immunosensing of PSA and MTX. The chapter also gives a brief background on the use of nanomaterials as drug nanocarriers and as enzyme mimetics or artificial enzymes for the development of a colorimetric immunosensors and their use in this work for the detection of PSA. Moreover, it provides a setting for the use of nanocarriers together with personal glucose meters for the digital monitoring of PSA.

### 2.1 Prostate cancer

Prostate Cancer (PCa) diagnosis, treatment, and monitoring are the various aspects of great interest to research due to the widespread of the disease, high mortality, and recurrence after treatment [1,2]. PCa is the second most common non-skin cancer in men. The International Agency for research on cancer, GLOBOCAN, estimated that 28 000 PCa deaths occurred in Africa in 2008 and predicted this number to double to 57 000 by 2030 [3]. On the other hand, it has been reported that the incidence of PCa will increase to 118,000 cases between 2025 and 2029 in Japan alone [4]. Hence, the development of diagnostic tools for the early detection of PCa will improve the diagnosis and management of the disease.

PCa starts in the prostate gland found in the male reproductive system. **Figure 2.1** shows (a) the pictorial representation of the position of prostate gland and (b) normal and cancer-affected prostate gland [5]. The prostate gland is found right below the bladder, in front of the rectum. The main function of the prostate gland is to produce the alkaline prostatic fluid that neutralizes the acidity of the vaginal tract and keeps the semen lifespan longer [6]. The cancer of the prostate normally emerges in elderly men with the rate of occurrence of 34% of men aged 50

years and 70% of men aged 80 years and above. Other risk factors for PCa include family history, race, and genome changes [7].

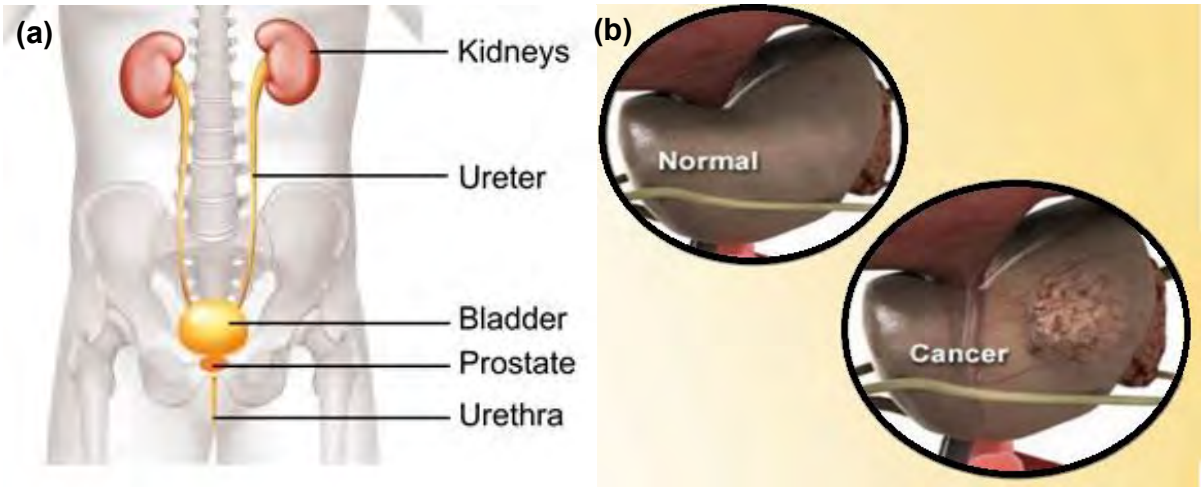


**Figure 2.1**: (a) Pictorial representation of the position of prostate and (b) normal and cancer-affected prostate gland [5].

### 2.1.1 Stages of prostate cancer

The stage of PCa plays an important role in the treatment and management of the disease. PCa is known to progress in four stages depending on the growth rate. The main stages of PCa are classified based on the size of the tumour and its spread. PCa is classified as stage 1 when the tumour cannot be felt by the medical doctor during the examination. When the tumour can be felt but has not yet spread to other organs, then PCa is said to be in stage 2. Stage 3 is appearing when the tumour has spread to nearby tissues and lastly when the tumour has spread to the bladder, PCa is classified as stage 4 as shown in **Fig. 2.2** [8].

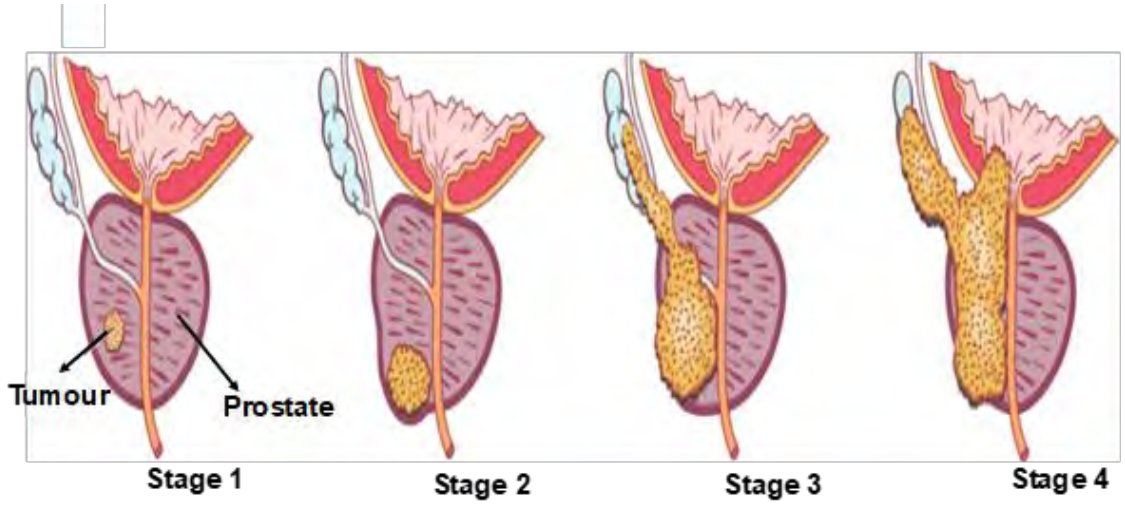


**Figure 2.2:** Illustration of the stages of prostate cancer based on the size and its spread [8].

Although PCa can be classified based on the tumour size and its spread, usually, the disease develops slowly and it is asymptomatic. Fast developing of PCa also occurs but this is less common. Early diagnosis of prostate cancer is vital in the treatment and curbing of the disease.

### 2.1.2 Diagnosis of prostate cancer

The diagnosis of PCa is commonly done by digital rectal exam (DRE) and the measurement of serum PSA. Literature has shown that DRE has remained the primary diagnostic method for the initial clinical examination of the prostate [9,10]. DRE procedure involves the experienced medical doctor performing a rectal examination to feel the exposed surface of the prostate gland [10]. The positive examination [11] is sometimes called the abnormal DRE results which appear when the growth of the prostate is felt [10]. This method of diagnosis of PCa has remained advantageous especially in men who do not secrete PSA. However, the DRE exam for the detection of prostate cancer is invasive and detects cancer in its late stages [2,3,12]. The recent advancement in prostate cancer detection is the antigen detection test using an immunologic method. This method detects prostate cancer antigen called the PSA.

PSA is a serine protease produced by both normal and malignant prostatic epithelium and is mainly secreted into seminal fluid, where it digests the gel-forming during the sexual event. However, small concentrations of PSA are released into the circulation system from the normal

prostate, and the concentration released increases in the presence of a prostatic disease [13]. Although the measurement of serum PSA for the diagnosis of PCa has been criticised for a lack of specificity, it still remains the most commonly used biomarker in PCa monitoring and management [14].

Recent research [15–19] has led to significant improvements in the tests for PSA due to the development of various detection methods. Although the detection of PSA presents some drawbacks regarding specificity, it is important to detect its concentration in human serum which can be useful in determining the presence of future risks of PCa. Different methods and strategies including electrochemical methods for the detection of PSA have been reported. Chuah et al. reported the use of modified gold-coated magnetic nanoparticles as 'dispersible electrodes' which act as selective capture vehicles for electrochemical detection of PSA [20]. Arya's group reported the use of Interdigitated microelectrodes (IDEs) functionalized with a cysteamine (Cys) self-assembled monolayer (SAM) to fabricate a sensitive, disposable, impedimetric biosensor for PSA detection [21]. Due to its intrinsic advantages, electrochemical detection of PSA has received significant attention recently. Electrochemical detection methods utilized recently for detection of PSA include impedimetric, amperometric, and potentiometric techniques. Most of these methods involve the use of the sandwich immunoassays approach in the design of the sensor [18]. Contrary to the use of DRE in the diagnosis of PCa, PSA tests are non-invasive, rapid, and can be miniaturized for point of care applications.

Herein, we present a label-free impedimetric immunosensor based on a stable thin monolayer film of isophthalic acid for detection of PSA. Ultrasensitive detection of PSA using glucose-encapsulated nanoliposomes bioconjugated with anti-PSA polyclonal antibody is also reported as nanobioprobes.

### 2.2 Anti-cancer drugs

Anti-cancer drugs also called anti-neoplastic drugs are chemical agents that are used to treat cancer [22]. Their history dates back to the 1940s when they were derived from toxins for chemical warfare and further developed for cancer treatment [23,24]. After the approval of nitrogen mustard mustine in 1949 by the U.S. Food and Drug Administration. Other drugs such as cyclophosphamide, chlorambucil, melphalan, bendamustine, and uramustine were also

developed. However, mustine was later discontinued as a therapeutic drug due to high toxicity. In the year 1953, 6-mercaptopurine and methotrexate (MTX) were approved as they were observed to inhibit cancer cell proliferation and growth. Since then MTX has been widely used for the treatment of several types of cancers including choriocarcinoma, carcinomas of head, neck, breast, lung, lymphocytic leukemia, sarcoma, trophoblastic tumor, testicular and bladder tumors, and psoriasis [22]. However, MTX has been found to cause several side effects such as gastrointestinal disorders, hepatic dysregulations, dermatitis, hematologic disorders, and nephrotoxicity pneumonitis [25–28] but still remain in use due to its effectiveness. During chemotherapy, the effective concentration range of MTX is limited to a relatively narrow therapeutic window. Hence, the dosage of MTX and its level in the blood needs to be regularly monitored, controlled, and individualized to establish the dose-response and side effects [28]. There is, therefore, high demand for rapid and highly sensitive methods for monitoring MTX in real-time and online. Also, this demand is increasing as the need for precision medicine is becoming crucial in clinical management of various diseases and thus avoiding current "one-size-fits-all" disease treatment regimes. As an emerging area of research interest, precision medicine allows for disease treatment to be personalized to each persons' biochemical nature.

### 2.2.1 Detection of MTX

**Scheme 2.1** shows the chemical structure of methotrexate (**1**) and the similar compound, folic acid coenzyme (**2**). The chemical structure of methotrexate is similar to the folic acid with several regions which contained pteridine ring, para-aminobenzoic acid and glutamic acid. The detection and monitoring of MTX in blood serum has been investigated by various research groups. Conventionally, the measurement of MTX in blood samples is often conducted using techniques such as high-performance liquid chromatography (HPLC) [29], oxidative fluorimetry [30], electrospray ionization tandem mass spectroscopy (ESI-MS) [31], and capillary zone electrophoresis (CZE) [32]. These techniques offer high accuracy, sensitivity, and selectivity, but they require highly trained personnel, large number of reagents, bulky instrumentation, and tedious sample preparation. This makes these techniques not amenable for on-site or point-of-care (POC) applications.

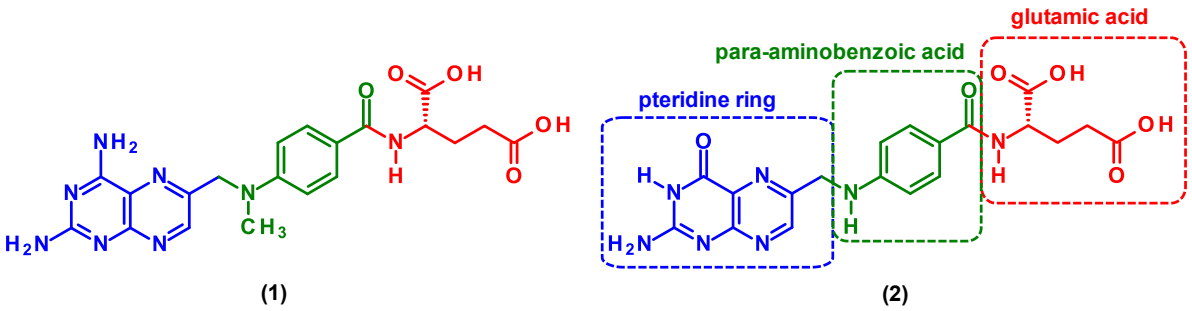


**Scheme 2.1:** Chemical structure of methotrexate (**1**) and folic acid coenzyme (2) with different regions indicated for their similarity with the methotrexate.

In this work, the construction of a capacitive biosensor for methotrexate detection was investigated. The use of electrografting of thin monolayer film and the covalent immobilization of monoclonal antibody was investigated.

## 2.3 Biosensors

A biosensor is an analytical device that measures biological or chemical reactions by generating signals proportional to the concentration of an analyte under investigation [33]. Biosensors are mainly applied for disease monitoring, drug discovery, and detection of pollutants, disease-causing micro-organisms, and biomarkers that are indicators of diseases in bodily fluids such as blood, urine, saliva, and sweat as shown in **Fig. 2.3** [34].

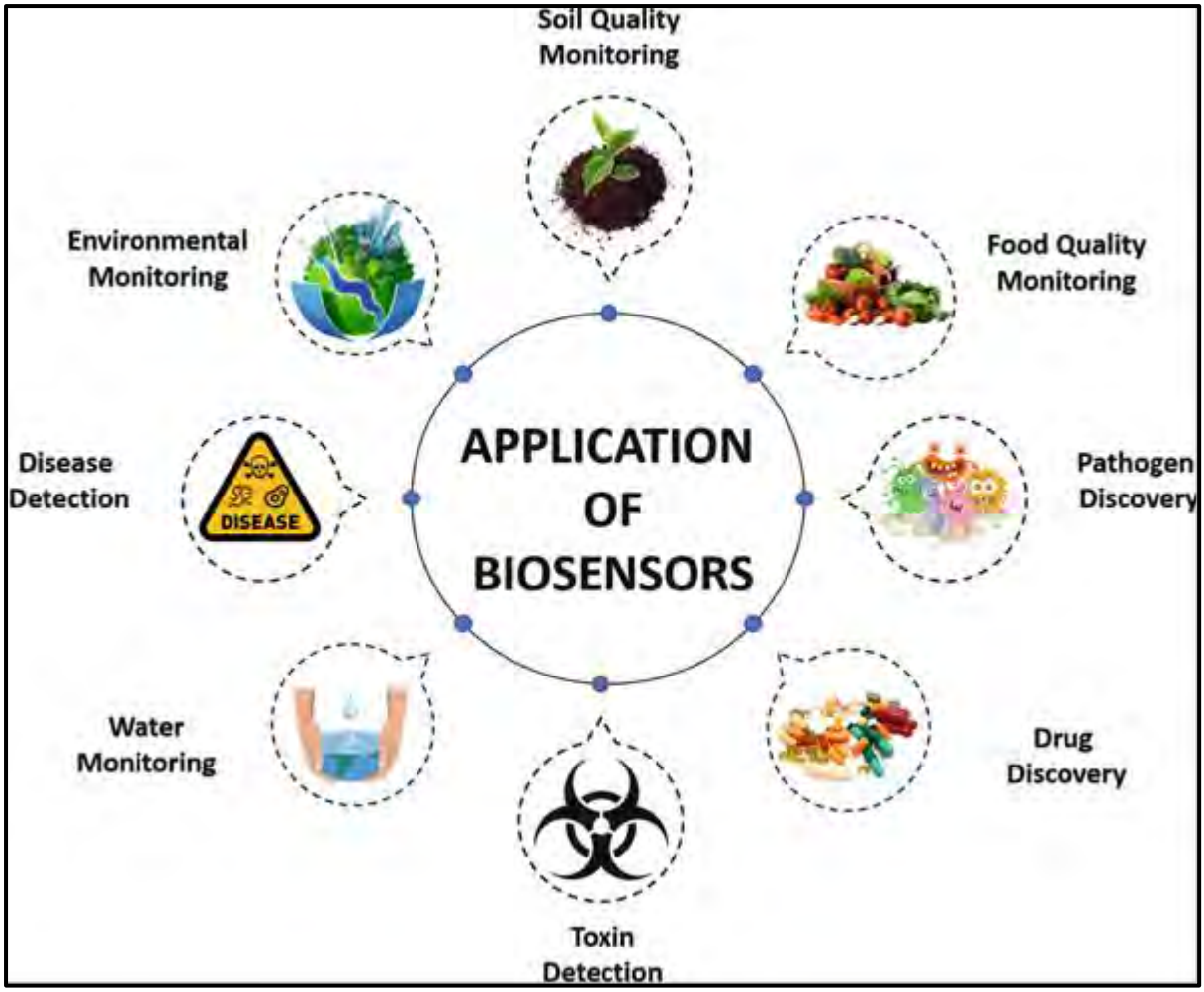


**Figure 2.3:** Major applications of biosensors [34].

A biosensor is mainly constructed with the recognition element also called the receptor attached onto the transducer for signal generation [35] as shown in **Fig. 2.4**. The recognition element is the component of the biosensor that interacts selectively and specifically with the bioanalyte of interest whilst, the transducer is the physicochemical detector that registers the changes during the biorecognition event into a quantifiable signal [33].

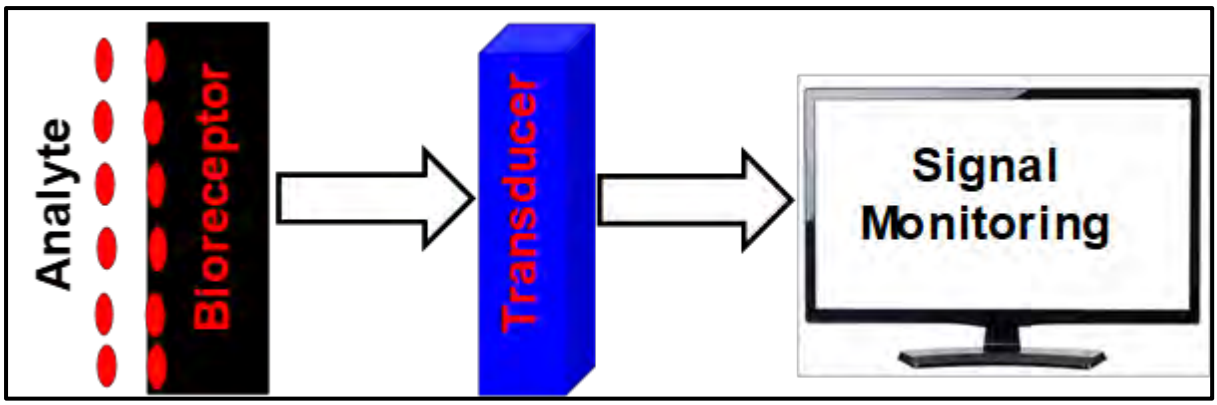


**Figure 2.4:** Major components of the biosensor.

Biosensors are usually classified depending on the bioreceptor and/or transduction method used [36]. The classification of biosensors based on the bioreceptor include enzyme, DNA, and aptamer biosensors. Whilst, the classification based on transducers include electrochemical, optical, and piezoelectric biosensors. The electrochemical signal of a biosensors can also be separated into potentiometric (for monitoring changes in potential), amperometric (monitoring the changes in current), conductometric (for changes in conducting properties), and impedimetric (impedance changes are monitored) [35]. This work investigates the use of electrochemical impedimetric and colorimetric biosensors and these will be discussed in details.

### 2.3.1 Impedimetric biosensors

An impedimetric biosensor is a type of electrochemical biosensor that has shown much promise for point-of-care testing applications due to low cost, ease of miniaturization, and label-free operation. Impedimetric biosensors can be operated in both Faradaic and non-Faradaic electrochemical impedance spectroscopy (EIS) [37]. The Faradaic EIS is performed in the presence of the redox probes and DC conditions are applied for the development of the electrochemical responses. This mode owes its name due to the current generated which obeys Ohm's law. The Faradaic current (I) is proportional to the number of electrons (n) transferred during the electrochemical reaction, and the flux of the electroactive molecules at the interface boundary (j) as shown in **Eq. (2.1)** [38]. F is Faraday's constant and A is electrode surface area.

$$I = nFAj \qquad \textbf{(2.1)}$$

In principle, the Faradaic EIS obtains impedance (Z) by applying sinusoidal potential, V(t), of small amplitude to an electrical circuit in which the resulting sinusoidal current, I(t), is measured through the circuit as shown in **Fig. 2.5**.

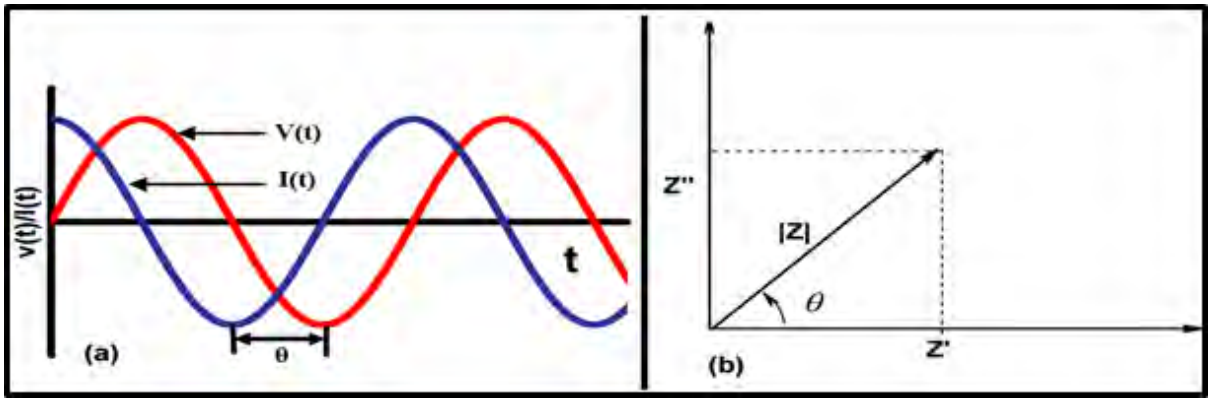


**Figure 2.5:** (a) Applied sinusoidal voltage, V(t), and a resulting sinusoidal current, I(t), response and (b) a vector representation of the real (Z′) and the imaginary (Z″) part of impedance (Z), showing the phase shift as $\theta$.

Therefore, Z is defined according to Ohm's law and can be expressed as shown in **Eq. (2.2):**

$$Z = \frac{V(t)}{I(t)} = \frac{V_0 \sin(\omega t)}{I_0 \sin(\omega t+\theta)} = Z_0 \frac{\sin(\omega t)}{\sin(\omega t+\theta)} \qquad \textbf{(2.2)}$$

and as a complex number, Z is expressed as shown in **Eq. (2.3):**

$$Z = \frac{V(t)}{I(t)} = Z_0 exp^{(j\theta)} = Z_0(cos\theta + jsin\theta) \qquad \textbf{(2.3)}$$

where, $Z$ (Ω) is the impedance, $Z_0$ impedance expressed as a magnitude of a vector, V(t) (V) is the sinusoidal potential at time t, I(t) (A) is the sinusoidal current at time t, θ is the phase shift, and $\omega$ (radians/s) is the radial frequency which can be defined as $\omega = 2\lambda f$, where $f$ is the frequency measured in Hz. Whilst, $j^2 = -1$.

**Equation (2.3)** is used to derive the complex impedance defined as shown in **Eq. (2.4):**

$$Z = Z' + jZ'' \qquad \textbf{(2.4)}$$

where, $Z' = Z_0(cos\theta) = |Z|cos\theta, and\ Z'' = Z_0 sin\theta = |Z|sin\theta$

The Impedance data is usually represented by the Nyquist plot, which is a plot of the imaginary part ($-Z''$, y-axis) versus the real part ($Z'$, x-axis) of impedance as shown in **Fig. 2.6(a)**. Impedance data may also be presented as the Bode plot in which the phase angle or the

magnitude of the impedance |Z| is plotted against the logarithm of frequency as shown in **Fig. 2.6(b).**

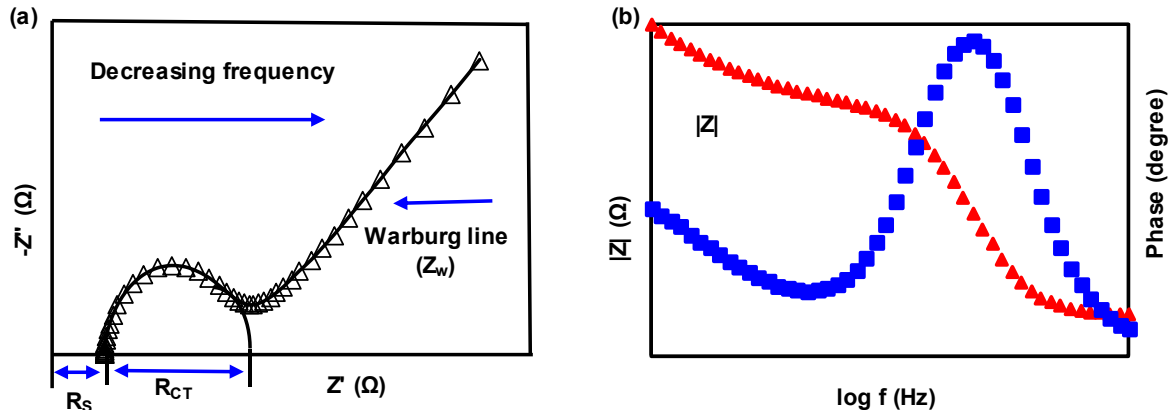


**Figure 2.6:** Impedance data representation (a) Nyquist plot, and (b) Bode plot, for the Randles electrochemical equivalent circuit with diffusion-limited behavior.

The impedance raw data obtained from an electrochemical experiment of a given electrode-materials system may be analyzed using an electrical equivalent circuit (EEC). These circuits are comprised of electrical elements like a capacitor (C) and resistance (R) to represent the electrochemical processes [39]. The capacitance of the electrochemical process, which is either the double-layer ($C_{dl}$) or the constant phase element (CPE) is caused by the excess charge at the electrode-electrolyte interface. The resistance within the circuit represents the electrical conductivity of the electrode-electrolyte electrochemical system being studied and that of the electrolyte in which the electrode is immersed. The most employed EEC in EIS is the Randles equivalent circuit shown in **Fig. 2.7(a).** In Randles equivalent circuit the solution or electrolyte resistance ($R_S$) is usually connected in series to a parallel combination of the charge-transfer resistance ($R_{CT}$) and the double layer capacitance ($C_{dl}$) in series as shown in **Fig. 2.7(a).** The component known as Warburg impedance ($Z_W$) is also shown in **Fig. 2.7** connecting in series with the $R_{CT}$. This is because Randles equivalent circuit takes into consideration the possibility of the reaction rate due to the diffusion mass transport phenomena of the electroactive species in the electrolyte solution [40]. **Figure 2.7(b)** shows the physical representation of the components at the electrode-electrolyte interface. It shows the species diffusing to the electrode surface to accept an electrode in the region involving the capacitance and the charge-transfer resistance. The reduced species diffuse back into solution away from the surface.

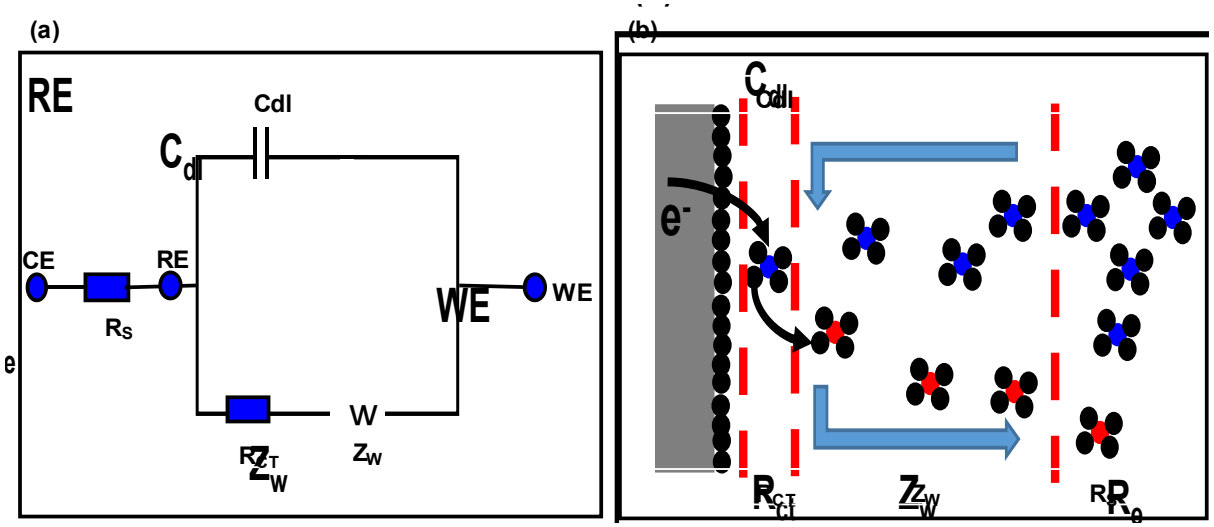


**Figure 2.7:** (a) Randles equivalent circuit for an electrochemical system with diffusion-limited behavior (b) physical representation of the circuit at the electrode-electrolyte interface.

Most of the Faradaic impedance biosensors measure the changes in charge transfer resistance ($R_{CT}$) as an indicator of bio-affinity, binding between the receptor (antibody) and the analyte (antigen) [41–43]. Usually, the increase in $R_{CT}$ is correlated to the increase in the concentration of an analyte [16,44,45]. Faradaic EIS immunosensors have been considered as very sensitive and selective biosensors due to lower limits of detection and high specificity. The strong selling point for Faradaic system is their label-free detection nature which offers direct changes during receptor-analyte interactions. However, the use of electroactive labels or redox probes has not made them amenable for point-of-care applications. In this thesis, non-Faradaic EIS immunosensors are reported and investigated as possible substitutes to the Faradaic immunosnsors.

On the contrary, the non-Faradaic EIS method does not require the use of electroactive labels or redox probes and also no need for a reference electrode [38,46]. Because of these features, non-Faradaic EIS appears to be more amenable to miniaturization and point-of-care application. Typically, non-Faradaic EIS immunosensors involve the charging and discharging of the double-layer capacitance during the interaction between the solid sensing electrode and the analyte in solution. Henceforth, the double layer capacitance is the impedance parameter that is mostly monitored at the electrode-electrolyte interface [38,47]. Because of this, non-Faradaic immunosensors are mostly referred to as capacitive biosensors [48–50] due to the buildup of capacitance at electrode-electrolyte interface. The double-layer capacitance (C) is

therefore defined by the Helmholtz model as a function of the free space permittivity ($\varepsilon_0$), relative solution permittivity ($\varepsilon_r$), distance (d) of the Helmholtz layer, and surface area of the electrode (A) as shown in **Eq. (2.5)** [38,51]:

$$C = \frac{\varepsilon_0 \varepsilon_r A}{d} \qquad \textbf{(2.5)}$$

In other research groups [43,52], the double-layer capacitance has been expressed as the complex capacitance derived from the impedance data as shown in **Eq. (2.6):**

$$C = C' + jC'' \equiv \frac{1}{j\omega Z} = \frac{-Z''}{j\omega|Z|^2} + j\frac{-Z'}{j\omega|Z|^2} \qquad \textbf{(2.6)}$$

**Equ. (2.6)** is sometimes used to construct the Nyquist plot of complex capacitance which comprise of the imaginary (C″) plotted against the real (C′) capacitance.

Literature has shown that capacitive immunosensing is more desirable than Faradaic EIS [47,48,50,53–56]. However, it has also been noted that the capacitive changes that occur during the bio-affinity reaction of a surface bound bioreceptor binding the analyte in solution results in relatively small changes [41]. This challenge has been suggested to be caused by the defects in the insulation layer anchoring the receptor on the electrode surface. Moreover, the immobilization method of the bioreceptor has been shown to greatly affect the capacitive behavior of the immunosensor. The literature argues that to achieve high sensitivity, the immobilized bioreceptor layer should be as thin as possible, but insulating enough to prevent the Faradaic processes from occurring [47,48]. Another challenge observed with capacitive immunosensors is data analysis techniques. Since the capacitive perturbations are relatively small, it means that significant differences in capacitance between two different concentrations of the analytes are not easily observed. These small changes are not detected during well-known circuit fitting. For example, more recently Phal et. al found that the capacitive detection of methotrexate on the anti-methotrexate antibody modified electrode was impossible by using the circuit fitting because there were no significant changes in the capacitance between different analyte concentrations [57]. This was in agreement with Juan Liu's assertion, that, the capacitive signal changes at electrode surface before and after binding reactions are typically very small in capacitive immunosensors [58]. The suggested remedies to the above challenges being faced in the development of capacitance biosensors included the formation of more compact SAMs of longer carbon chain length [47] and the use of smaller molecules such as

mimotope [58]. These remedies have been shown to improve the capacitance signal. However, SAMs have been shown to cause defects on the insulation layer due to their instability, mobility on the electrode surface and are prone to oxidize leading to their desorption [47,59,60]. Henceforth, electrografting of diazonium salts onto electrode surfaces has attracted recent attention due to stable carbide (metal-carbon, M-C) bond that forms between the generated radical and the electrode surface. For example, more recently, Phal et. al used electrografting of diazonium salts for the development of a capacitive biosensor for the detection of methotrexate and they found that the method was highly reproducible, less time consuming, and stable [61].

### 2.3.2 Electrografting diazonium salts

Electrografting has been defined as the electrochemical process that allows for the attachment of organic molecules onto the conducting solid surfaces [62]. In principle, the electrografting of aryldiazonium salts onto the electrode surface involves a two-steps process: (i) one electron-reduction of the substituted aryldiazonium salt dissolved either in aqueous media or in acetonitrile containing an electrolyte, and (ii) followed by covalent attachment of the aryl radical group onto the surface as shown in **Scheme 2.2**. During the first step (electroreduction), the formation of aryl radical occrs after the diazonium salt loses the nitrogen ($N_2$) group. The aryl radical adsorbs spontaneously onto the electrode surface when the electrode is scanned onto high reduction potentials.

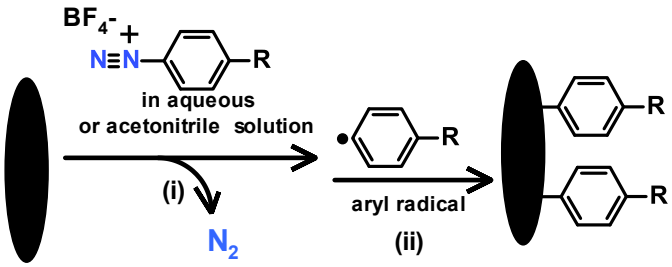


**Scheme 2.2:** Electrografting of para-substituted aryldiazonium salt by (i) electroreduction step leading the generation of the aryl radical, followed by (ii) spontaneous adsorption of the aryl radical onto the electrode surface.

The modification of surfaces with aryldiazonium salts can also be done by spontaneous reaction, reducing surfaces, reducing agents, and photochemistry other than electrochemistry [63]. Electrografting has presented researchers with numerous electrode modification advantages and these include: (i) high stability of the gold-carbon (Au-C) or carbon-carbon (C-C) bonds, (ii) high reproducibility, (iii) less time for electrode modification, and (iv) an ability to modify various other conducting surfaces apart from gold and/or carbon. However, it has found less applications for the development of capacitive biosensors and this is due to the formation of thick films. Thick films formation reduces the sensitivity of capacitive biosensors as changes during the capturing of the target analyte are very small. Garrote's group stressed that the capacitive sensors are more sensitive to interfacial changes at film thickness less than 10 nm [64]. Efforts have been made to develop well-ordered monolayers onto electrode surfaces by electrografting 3,5-*bis*-tertbutylbenzenediazonium salt [65]. The presence of tertbutyl groups on positions three and five of the benzene ring hindered the formation of the multilayers, and thus resulted in the formation of a thin monolayer film of 3,5-*bis*-tertbulyphenyl groups. However, the bulky (tertbutyl) functional groups used could not support post-functionalization of the modified surface for the development of an immunosensor. Building on this idea, in this thesis, the 5-diazonium isophthalic acid (5-DIPA) was synthesized from 5-amino isophtalic acid and used for the development of a controlled thin monolayer film of isophthalic acid. The electrografted monolayer contained carboxylic functional groups which were then used as an anchoring block for the immobilization of bioreceptors. This led to the subsequent development of capacitance biosensors for the detection of PSA on the gold electrode and MTX on glassy carbon and screen-printed carbon electrodes. For the detection of MTX, data analysis of EIS for capacitive monitoring was conducted using singular value decomposition (SVD) multivariate data analysis. To show the robustness of the capacitive immunosensor developed here, the detection of PSA was done using three different systems of EIS data analysis. These were circuit fitting of a resistor connected in series with the capacitor ($R_SC$); the conversion of the EIS data from the total impedance to total capacitance and the assumption of a supercapacitor, in that the capacitance changes are due to the imaginary impedance at a specific frequency. PSA was also detected using the colorimetric immunosensing method.

### 2.3.3 Colorimetric immunosensor

#### 2.3.3.1 Principle of colorimetric immunosensor

Colorimetric immunosensor research has attracted great research attention and this is due to the widely used and commercial available enzyme-linked immunosorbent assays, ELISA. Enzyme catalysis converts specific substrates into coloured products which can be spectroscopically measured and determined. In addition to these fascinating properties, enzyme immunoassays (EIA) are also simple and their mechanism which produces colored products can be observed with a naked eye, hence, their convenience for point-of-care applications. In addition to ELISA detection systems, the same principle was used for immunochromatographic lateral flow system using colour developing or colour producing enzyme-substrate reactions. However, ELISA systems are still laboratory based (or confined), require specialized skilled personnel for their operation and results interpretation, and require high sample and reagent volumes. These are the major limitations of ELISA. The most successful colorimetric immunosensors and attractive for POCT applications are the immunochromatographic lateral flow tests (LFTs) [66]. Traditionally, colorimetric immunosensors involve the monitoring of enzymatic reaction colour changes during the detection. For example, the natural enzymes widely used in colorimetric biosensors are horseradish peroxidase (HRP) and alkaline phosphatase (ALP) enzymes. HRP catalyzes the oxidation of 3,3',5,5'-tetramethylbenzidine (TMB) as a substrate to its blue coloured oxidation products in colorimetric immunosensor development [67–69]. ALP, on the other hand, catalyzes the hydrolysis of 4-nitrophenyl phosphate to p-nitrophenol which is yellow in colour and has high absorption extinction coefficient. However, natural enzymes are costly and denature easily in extreme pH and temperature conditions. These shortcomings for enzymes have severely restricted their analytical applications. Henceforth, there is a growing interest in research towards inorganic (nano) materials that exhibit similar enzyme-like catalysis and are more stable in environments known to be harsh for biological enzymes. These will be useful in the development of colorimetric immunosensors as characterized by high sensitivity, stability, affordability and huge potential for mass production.

#### 2.3.3.2 Nanomaterials in colorimetric biosensor development

The emergence of nanomaterial-based colorimetric immunosensors has enabled the development and use of nanomaterials as electroactive substance carriers and catalysts. As electroactive carriers, nanomaterials can encapsulate redox active substances and use these for the detection of analytes. As catalysts, their ability to transform substrates to coloured products is a subject of interest and their use as artificial enzymes. As catalysts, nanomaterials have been shown to possess enzyme-like catalysis properties. This is because nanomaterials are highly tuneable for efficient catalytic activity, are stable, affordable, and possess a large surface area for antibody loading and leaving enough surface for catalysis. Nanomaterials for the development of nanomaterial-based colorimetric immunosensors can be categorized into three main types (i) nanocarriers [70], (ii) colorimetric substrates with localized surface plasmon resonance absorption [71], and (iii) as artificial enzymes (nanozymes) [72]. This thesis focuses on the use of nanomaterials as carriers for electroactive species and also as artificial enzymes (nanozymes) for the development of a colorimetric immunosensor for PSA. For their applications as nanocarriers, nanoliposomes encapsulating glucose molecules were used for the repurposing of the personal glucose meters and their use in the detection of PSA.

Nanomaterials, especially nanoliposomes have been widely used as drug nanocarriers and for loading various signal-generating elements for the development of nanomaterial-based colorimetric immunosensors. As electroactive species nanocarriers, nanomaterials have been combined with already existing technologies like personal glucose meters (PGMs) for the detection of encapsulated glucose [73–75], lateral flow tests [66], and smart cellphones [76,77] for the development of point-of-care testing devices. Recently, liposomes have been used to encapsulate signal enhancing labels including glucose [73,78] for sensing applications due to their massive loading capacity and biocompatibility [70]. Liposomes have been widely used to carry drugs that are effective but fail clinical trials due to their properties for targeted drug delivery [79–82]. They have recently been combined with personal glucose meters and lateral flow testing kits for the detection of various bioanalytes. For example, Tang's group [78] used liposomes as glucose carriers for the colorimetric immunoassay of streptomycin. In another work, Juan's group [73] reported the glucose-loaded liposomes conjugated with antibodies to specifically bind to the antigen and form a sandwich immunoassay for the detection of aflatoxin using PGM. Luo's group [83] encapsulated HRP into liposomes and released it to catalyze the oxidation of TMB in the presence of hydrogen peroxide. Many challenges still exist despite

the successful use of liposomes as cargo carriers for the sensing indicators like glucose [73,78], nanoparticles [84], and enzymes [74]. Some of the challenges include: (i) low concentrations of the encapsulated electroactive material, which may affect the sensitivity and later the limit of detection; (ii) stability in physiological conditions which can also result in a false reading; and (iii) premature or uncontrolled release or leakage of the encapsulated electroactive material which can lead to a false reading. These challenges can directly affect the selectivity and much more the sensitivity of the sensing system. Hence, there is a growing need for the development of a more robust liposomal formulation that will be more stable with controlled release characteristics for the new sensing systems.

In this thesis, the preparation of glucose-encapsulating nanoliposomes (GENLs) for controlled release studies and sandwich immunoassay detection of PSA was investigated. The quantification of the encapsulated glucose within GENLs for the detection of PSA was investigated using three signal monitoring systems that is Pd|PdO nanoparticles, personal glucose meters (PGMs), and horseradish peroxidase (HRP).

Nanozymes are nanomaterials classified as artificial enzymes because of their intrinsic enzyme-like activity [85]. The applicability of nanomaterials was apparent in the work done by Gao et. al in 2007 which observed that $Fe_3O_4$ nanoparticles exhibited intrinsic peroxidase-like activity [86]. Since then, over 300 types of nanomaterials have been studied for their intrinsic enzyme-like activity, including peroxidase activity [85]. Other than $Fe_3O_4$ nanoparticles, nanozymes studied for peroxidase-like activity include $Co_3O_4$ [87], CuO [88], $MnFe_2O_4$ [89], $CoFe_2O_4$ [90], and palladium nanoparticles [91].

In this thesis, nanoliposomes were used as nanocarriers of glucose due to their massive loading capacity, and their surface was designed to provide functional groups for the immobilization of the detecting antibodies. Glucose was used for signal amplification for both colorimetric immunosensing and personal glucose meter for digital read-out of PSA concentration. Whilst, palladium nanoparticles (Pd|PdO) were used to compare their catalytic activity towards the colorimetric peroxidase detection of PSA. This part of the thesis was aimed at improving the sensitivity and reducing the cost of detection of PSA by combining the high-loading nanobioprobes (anti-PSA polyclonal antibodies bioconjugated onto glucose-encapsulating nanoliposomes) and high catalytic Pd|PdO nanoparticles for ultrasensitive colorimetric detection of PSA. It also aimed at developing a highly sensitive digital testing of PSA by combining the high-loading nanobioprobes and a personal glucose meter.

## 2.4 References


[1] Y.-E. Choi, J.-W. Kwak, J.W. Park, Nanotechnology for Early Cancer Detection, Sensors, 10 (2010) 428–455.

[2] I.E. Tothill, Biosensors for cancer markers diagnosis, Semin. Cell Dev. Biol. 20 (2009) 55–62.

[3] C. Babb, M. Urban, D. Kielkowski, P. Kellett, Prostate cancer in South Africa: pathology based national cancer registry data (1986-2006) and mortality rates (1997-2009), Prostate Cancer. 2014 (2014) 419801 (1-9).

[4] K. Ito, Y. Fujizuka, K. Ishikura, B. Cook, Next-generation prostate-specific antigen test: precursor form of prostate-specific antigen, Int. J. Clin. Oncol. 19 (2014) 782–792.

[5] C. Patrick, Signs of Prostate Cancer: Symptoms, PSA Test, Treatments, (2021) 1–31. https://www.onhealth.com/content/1/prostate_cancer (Date accessed: 20th December 2021)

[6] C. Huggins, The Physiology of the Prostate Gland, J. Physrev. 25 (1945) 281-295.

[7] National Cancer Institute, Prostate Cancer Prevention (PDQ(R)): Health Professional Version, Cancer.Gov. (2002) 1–24. https://www.cancer.gov/types/prostate/hp/prostate-prevention-pdq. (Date accessed: 24th December 2021).

[8] Sunshine Coast Urology, What is Prostate Cancer? (2016) 1-2. https://sunshinecoasturology.com.au/useful-info/urological-conditions/what-is-prostate-cancer. (Date accessed: 27th December 2021).

[9] N. Borley, M.R. Feneley, Prostate cancer: Diagnosis and staging, Asian J. Androl. 11 (2009) 74–80.

[10] C. Tonry, S. Finn, J. Armstrong, S.R. Pennington, Clinical proteomics for prostate cancer: understanding prostate cancer pathology and protein biomarkers for improved disease management, Clin. Proteomics. 17 (2020) 1–31.

[11] A. Hoogendam, F. Buntinx, H.C.W. De Vet, The diagnostic value of digital rectal examination in primary care screening for prostate cancer: A meta-analysis, Fam. Pract. 16 (1999) 621–626.

[12] B. Bohunicky, S.A. Mousa, Biosensors: The new wave in cancer diagnosis, Nanotechnol. Sci. Appl. 4 (2011) 1–10.

[13] U.-H. Stenman, J. Leinonen, W.-M. Zhang, P. Finne, Prostate-specific antigen, Semin. Cancer Biol. 9 (1999) 83–93.

[14] J. Meehan, M. Gray, C. Mart, C. Kay, D. Mclaren, A.K. Turnbull, Tissue- and Liquid-Based Biomarkers in Prostate Cancer Precision Medicine, J. Pers. Med. 11 (2021) 1–37.

[15] M. Adhyam, A.K. Gupta, A Review on the Clinical Utility of PSA in Cancer Prostate, Indian J. Surg. Oncol. 3 (2012) 120–129.

[16] S.K. Arya, S. Bhansali, Anti-Prostate Specific Antigen (Anti-PSA) Modified Interdigitated Microelectrode-Based Impedimetric Biosensor for PSA Detection, Biosens. J. 1 (2012) 1–7.

[17] E. Llop, M. Ferrer-Batallé, S. Barrabés, P.E. Guerrero, M. Ramírez, R. Saldova, P.M. Rudd, R.N. Aleixandre, J. Comet, R. de Llorens, R. Peracaula, Improvement of Prostate Cancer Diagnosis by Detecting PSA Glycosylation-Specific Changes, Theranostics. 6 (2016) 1190–1204.

[18] P. Sarkar, P.S. Pal, D. Ghosh, S.J. Setford, I.E. Tothill, Amperometric biosensors for detection of the prostate cancer marker (PSA), Int. J. Pharm. 238 (2002) 1–9.

[19] L. Zhu, J. Leinonen, W.M. Zhang, P. Finne, U.H. Stenman, Dual-label immunoassay for simultaneous measurement of prostate-specific antigen (PSA)-α1-antichymotrypsin complex together with free or total PSA, Clin. Chem. 49 (2003) 97–103.

[20] K. Chuah, L.M.H. Lai, I.Y. Goon, S.G. Parker, R. Amal, J. Justin Gooding, Ultrasensitive electrochemical detection of prostate-specific antigen (PSA) using gold-coated magnetic nanoparticles as “dispersible electrodes”, Chem. Commun. 48 (2012) 3503–3505.

[21] S.K. Arya, S. Bhansali, Anti-Prostate Specific Antigen (Anti-PSA) Modified Interdigitated Microelectrode-Based Impedimetric Biosensor for PSA Detection, Biosens. J. 1 (2012) 1–7.

[22] K.K. Kwok, E.C. Vincent, J.N. Gibson, Antineoplastic Drugs, Seventh Ed, Elsevier, 2017, 530-562.

[23] A. Gilman, Therapeutic applications of chemical warfare agents, Fed. Proc. 5 (1946) 285–292.

[24] F.M. Golomb, Agents Used in Cancer Chemotherapy, Am.J.Surg, 105 (1963) 579-590.

[25] W. Wang, H. Zhou, L. Liu, Side effects of methotrexate therapy for rheumatoid arthritis: A systematic review, Eur. J. Med. Chem. 158 (2018) 502–516.

[26] G.S. Alarcóan, I.C. Tracy, W.D. Blackburn, Methotrexate in rheumatoid arthritis. Toxic effects as the major factor in limiting long-term treatment, Arthritis Rheum. 32 (1989) 671–676.

[27] M.J.H. Wijnands, M.A. Van't Hof, M.A. Van Leeuwen, M.H. Van Rijswijk, L.B.A. Van De Putte, P.L.C.M. Van Riel, Long-term second-line treatment: A prospective drug survival study, Rheumatology. 31 (1992) 253–258.

[28] A.M. Boerbooms, P.J. Kerstens, J.W. van Loenhout, J. Mulder, L.B. van de Putte, Infections during low-dose methotrexate treatment in rheumatoid arthritis, Semin. Arthritis Rheum. 24 (1995) 411–421.

[29] H. Li, W. Luo, Q. Zeng, Z. Lin, H. Luo, Y. Zhang, Method for the determination of blood methotrexate by high performance liquid chromatography with online post-column electrochemical oxidation and fluorescence detection, J. Chromatogr. B Anal. Technol. Biomed. Life Sci. 845 (2007) 164–168.

[30] S. Chen, Z. Zhang, D. He, Y. Hu, H. Zheng, C. He, Flow-injection–electrochemical oxidation fluorimetry for determination of methotrexate, Luminescence. 22 (2007) 338–342.

[31] I. Rodin, A. Braun, A. Stavrianidi, O. Shpigun, A validated LC-MS/MS method for rapid determination of methotrexate in human saliva and its application to an excretion evaluation study, J. Chromatogr. B Anal. Technol. Biomed. Life Sci. 937 (2013) 1–6.

[32] C.M. Roach, P. Gozel, R.N. Zare, Determination of Methotrexate and its Major Metabolite, 7-hydroxymethotrexate, using Capillary Zone Electrophoresis and Laser-induced Fluorescence Detection, J. Chromatogr. 426 (1988) 129–140.

[33] N. Bhalla, P. Jolly, N. Formisano, P. Estrela, Introduction to biosensors, Essays Biochem. 60 (2016) 1–8.

[34] Singh, S., Kumar, V., Dhanjal, D.S., Datta, S., Prasad, R., Singh, J. Biological Biosensors for Monitoring and Diagnosis. In: Singh, J., Vyas, A., Wang, S., Prasad, R. (eds) Microbial Biotechnology: Basic Research and Applications. Environmental and Microbial Biotechnology. Springer, Singapore,2020: pp. 317–335.

[35] D.R. Thévenot, K. Toth, R.A. Durst, G.S. Wilson, Electrochemical biosensors: Recommended definitions and classification, Biosens. Bioelectron. 16 (2001) 121–131.

[36] G. Rocchitta, A. Spanu, S. Babudieri, G. Latte, G. Madeddu, G. Galleri, S. Nuvoli, P. Bagella, M.I. Demartis, V. Fiore, R. Manetti, P.A. Serra, Enzyme biosensors for biomedical applications: Strategies for safeguarding analytical performances in biological fluids, Sensors (Switzerland). 16 (2016) 780 (1-21).

[37] S.K. Arya, P. Zhurauski, P. Jolly, M.R. Batistuti, M. Mulato, P. Estrela, Capacitive aptasensor based on interdigitated electrode for breast cancer detection in undiluted human serum, Biosens. Bioelectron. 102 (2018) 106–112.

[38] R.A. Dorledo de Faria, L.G. Dias Heneine, T. Matencio, Y. Messaddeq, Faradaic and non-Faradaic electrochemical impedance spectroscopy as transduction techniques for sensing applications, Int. J. Biosens. Bioelectron. 5 (2019) 29–31.

[39] E.P. Randviir, C.E. Banks, Electrochemical impedance spectroscopy: An overview of bioanalytical applications, Anal. Methods. 5 (2013) 1098–1115.

[40] J.A. Dean, Basics of Electrochemical Impedance Spectroscopy Introduction, Princet. Apllied Res. (1995) 15.1-15.5.

[41] J.S. Daniels, N. Pourmand, Label-free impedance biosensors: Opportunities and challenges, Electroanalysis. 19 (2007) 1239–1257.

[42] J. Leva-Bueno, S.A. Peyman, P.A. Millner, A review on impedimetric immunosensors for pathogen and biomarker detection, Med. Microbiol. Immunol. 209 (2020) 343–362.

[43] T. Bertok, L. Lorencova, E. Chocholova, E. Jane, A. Vikartovska, P. Kasak, J. Tkac, Electrochemical Impedance Spectroscopy Based Biosensors: Mechanistic Principles, Analytical Examples and Challenges towards Commercialization for Assays of Protein Cancer Biomarkers, Chem.Electro.Chem. 6 (2019) 989–1003.

[44] O.K. Adeniyi, P.N. Mashazi, Stable thin films of human P53 antigen on gold surface for the detection of tumour associated anti-P53 autoantibodies, Electrochim. Acta. 331 (2020) 135272 (1-10).

[45] A.G. Mantzila, V. Maipa, M.I. Prodromidis, Development of a Faradaic impedimetric immunosensor for the detection of Salmonella typhimurium in milk, Anal. Chem. 80 (2008) 1169–1175.

[46] J.S. Park, H.J. Kim, J.H. Lee, J.H. Park, J. Kim, K.S. Hwang, B.C. Lee, Amyloid beta detection by Faradaic electrochemical impedance spectroscopy using interdigitated microelectrodes, Sensors (Switzerland). 18 (2018) 426-436.

[47] V.M. Mirsky, M. Riepl, O.S. Wolfbeis, Capacitive monitoring of protein immobilization and antigen-antibody reactions on monomolecular alkylthiol films on gold electrodes, Biosens. Bioelectron. 12 (1997) 977–989.

[48] C. Berggren, G. Johansson, Capacitance Measurements of Antibody-Antigen Interactions in a Flow System, Anal. Chem. 69 (1997) 3651–3657.

[49] M. Prodromidis, Impedimetric Biosensors and Immunosensors, Proc. 2nd Int. Semin. Anal. Sci. 8 (2007) 69–71.

[50] A. Qureshi, Y. Gurbuz, J.H. Niazi, Label-free capacitance based aptasensor platform for the detection of HER2/ErbB2 cancer biomarker in serum, Sensors Actuators, B Chem. 220 (2015) 1145–1151.

[51] J. Kang, J. Wen, S.H. Jayaram, A. Yu, X. Wang, Development of an equivalent circuit model for electrochemical double layer capacitors (EDLCs) with distinct electrolytes, Electrochim. Acta. 115 (2014) 587–598.

[52] P. Jolly, N. Formisano, J. Tkáč, P. Kasák, C.G. Frost, P. Estrela, Label-free impedimetric aptasensor with antifouling surface chemistry: A prostate specific antigen case study, Sensors Actuators, B Chem. 209 (2015) 306–312.

[53] J. Rickert, W. Göpel, W. Beck, G. Jung, P. Heiduschka, A "mixed" self-assembled monolayer for an impedimetric immunosensor, Biosens. Bioelectron. 11 (1996) 757–768.

[54] C. Gautier, C. Esnault, C. Cougnon, J.F. Pilard, N. Casse, B. Chénais, Hybridization-induced interfacial changes detected by non-Faradaic impedimetric measurements compared to Faradaic approach, J. Electroanal. Chem. 610 (2007) 227–233.

[55] S. Brosel-Oliu, N. Uria, N. Abramova, A. Bratov, Impedimetric Sensors for Bacteria Detection, in: Biosensors-Micro and Nanoscale Applications, IntechOpen, 2015:pp. 258-288

[56] J. Cecchetto, A. Santos, A. Mondini, E.M. Cilli, P.R. Bueno, Serological point-of-care and label-free capacitive diagnosis of dengue virus infection, Biosens. Bioelectron. 151 (2020) 111972 (1-7).

[57] S. Phal, B. Shatri, A. Berisha, P. Geladi, B. Lindholm-Sethson, S. Tesfalidet, Covalently electrografted carboxyphenyl layers onto gold surface serving as a platform for the construction of an immunosensor for detection of methotrexate, J. Electroanal. Chem. 812 (2018) 235–243.

[58] J. Liu, M.M. Chisti, X. Zeng, General Signal Amplification Strategy for Non-Faradaic Impedimetric Sensing: Trastuzumab Detection Employing a Peptide Immunosensor, Anal. Chem. 89 (2017) 4013–4020.

[59] M. Riepl, V.M. Mirsky, O.S. Wolfbeis, Electrical control of alkanethiols self-assembly on a gold surface as an approach for preparation of microelectrode arrays, Mikrochim. Acta. 131 (1999) 29–34.

[60] C. Berggren, B. Bjarnason, G. Johansson, Capacitive biosensors, Electroanalysis. 13 (2001) 173–180.

[61] S. Phal, K. Shimizu, D. Mwanza, P. Mashazi, A. Shchukarev, S. Tesfalidet, V. Van Tran, J.Y. Moon, Y.C. Lee, Electrografting of 4-carboxybenzenediazonium on glassy carbon electrode: The effect of concentration on the formation of mono and multilayers, J. Control. Release. 300 (2019) 4575 1–12.

[62] D. Bélanger, J. Pinson, Electrografting: A powerful method for surface modification, Chem. Soc. Rev. 40 (2011) 3995–4048.

[63] D. Hetemi, V. Noël, J. Pinson, Grafting of diazonium salts on surfaces: Application to biosensors, Biosensors. 10 (2020) 4-36.

[64] B.L. Garrote, A. Santos, P.R. Bueno, Label-free capacitive assaying of biomarkers for molecular diagnostics, Nat. Protoc. 15 (2020) 3879–3893.

[65] M. Ceccato, A. Bousquet, M. Hinge, S.U. Pedersen, K. Daasbjerg, Using a mediating effect in the electroreduction of aryldiazonium salts to prepare conducting organic films of high thickness, Chem. Mater. 23 (2011) 1551–1557.

[66] M. Pohanka, Point-of-Care Diagnoses and Assays Based on Lateral Flow Test, Int. J. Anal. Chem. 2021 (2021) 6685619 (1-9).

[67] R.W. Bally, T.C.J. Gribnau, Some Aspects of the Chromogen 3,3',5,5'-Tetramethylbenzidine as Hydrogen Donor in a Horseradish Peroxidase Assay, Clin. Chem. Lab. Med. 27 (1989) 791–796.

[68] L. Shayne, T.K. Omatsu, S.M. Ohammadi, M.M. Aeki, A.I. Shida, H.T. Ani, M.T. Okeshi, Peroxidase-based Assays, 32 (2016) 815–818.

[69] V.X.T. Zhao, T.I. Wong, X.T. Zheng, Y.N. Tan, X. Zhou, Colorimetric biosensors for point-of-care virus detections, Mater. Sci. Energy Technol. 3 (2020) 237–249.

[70] L. Liu, Y. Hao, D. Deng, N. Xia, Nanomaterials-based colorimetric immunoassays, Nanomaterials. 9 (2019) 316-348.

[71] H. Wang, T. Wu, M. Li, Y. Tao, Recent advances in nanomaterials for colorimetric cancer detection, J. Mater. Chem. B. 9 (2021) 921–938.

[72] Q. Liu, A. Zhang, R. Wang, Q. Zhang, D. Cui, A Review on Metal- and Metal Oxide-Based Nanozymes: Properties, Mechanisms, and Applications, Nano-Micro Lett., 13 (2021) 13-54.

[73] J. Tang, Y. Huang, H. Liu, C. Zhang, D. Tang, Novel glucometer-based immunosensing strategy suitable for complex systems with signal amplification using surfactant-responsive cargo release from glucose-encapsulated liposome nanocarriers, Biosens. Bioelectron. 79 (2016) 508–514.

[74] B. Lin, D. Liu, J. Yan, Z. Qiao, Y. Zhong, J. Yan, Z. Zhu, T. Ji, C.J. Yang, Enzyme-Encapsulated Liposome-Linked Immunosorbent Assay Enabling Sensitive Personal Glucose Meter Readout for Portable Detection of Disease Biomarkers, ACS Appl. Mater. Interfaces. 8 (2016) 6890–6897.

[75] J. Joo, D. Kwon, H.H. Shin, K.H. Park, H.J. Cha, S. Jeon, A facile and sensitive method for detecting pathogenic bacteria using personal glucose meters, Sensors Actuators, B Chem. 188 (2013) 1250–1254.

[76] W. Jung, J. Han, J.W. Choi, C.H. Ahn, Point-of-care testing (POCT) diagnostic systems using microfluidic lab-on-a-chip technologies, Microelectron. Eng. 132 (2014) 46–57.

[77] S. Wang, X. Zhao, I. Khimji, R. Akbas, W. Qiu, D. Edwards, D.W. Cramer, B. Ye, U. Demirci, Integration of cell phone imaging with microchip ELISA to detect ovarian cancer HE4 biomarker in urine at the point-of-care, Lab Chip. 11 (2011) 3411–3418.

[78] R. Ren, G. Cai, Z. Yu, D. Tang, Glucose-loaded liposomes for amplified colorimetric immunoassay of streptomycin based on enzyme-induced iron(II) chelation reaction with phenanthroline, Sensors Actuators, B Chem. 265 (2018) 174–181.

[79] W. Guo, T. Lee, J. Sudimack, R.J. Lee, Receptor-Specific Delivery of Liposomes Via Folate-Peg-Chol, J. Liposome Res. 10 (2000) 179–195.

[80] C.I. Nkanga, R.W. Krause, X.S. Noundou, R.B. Walker, Preparation and characterization of isoniazid-loaded crude soybean lecithin liposomes, Int. J. Pharm. 526 (2017) 466–473.

[81] V. Van Tran, J.Y. Moon, Y.C. Lee, Liposomes for delivery of antioxidants in cosmeceuticals: Challenges and development strategies, J. Control. Release. 300 (2019) 114–140.

[82] C.H.A. Boakye, K. Patel, R. Doddapaneni, A. Bagde, S. Marepally, M. Singh, Novel amphiphilic lipid augments the co-delivery of erlotinib and IL36 siRNA into the skin for psoriasis treatment, J. Control. Release. 246 (2017) 120–132.

[83] C. Lin, Y. Guo, M. Zhao, M. Sun, F. Luo, L. Guo, B. Qiu, Z. Lin, G. Chen, Highly sensitive colorimetric immunosensor for influenza virus H5N1 based on enzyme-encapsulated liposome, Anal. Chim. Acta. 963 (2017) 112–118.

[84] A.A. Yetisgin, S. Cetinel, M. Zuvin, A. Kosar, O. Kutlu, Therapeutic Nanoparticles and Their Targeted Delivery Applications, Mol. 25 (2020) 2193 (1-31).

[85] P. Wang, T. Wang, J. Hong, X. Yan, M. Liang, Nanozymes: A New Disease Imaging Strategy, Front. Bioeng. Biotechnol. 8 (2020) 1–10.

[86] L. Gao, X. Yan, Nanozymes: An emerging field bridging nanotechnology and biology, Sci. China Life Sci. 59 (2016) 400–402.

[87] J. Dong, L. Song, J.J. Yin, W. He, Y. Wu, N. Gu, Y. Zhang, $Co_3O_4$ nanoparticles with multi-enzyme activities and their application in immunohistochemical assay, ACS Appl. Mater. Interfaces. 6 (2014) 1959–1970.

[88] A.L. Hu, H.H. Deng, X.Q. Zheng, Y.Y. Wu, X.L. Lin, A.L. Liu, X.H. Xia, H.P. Peng, W. Chen, G.L. Hong, Self-cascade reaction catalyzed by CuO nanoparticle-based dual-functional enzyme mimics, Biosens. Bioelectron. 97 (2017) 21–25.

[89] A.A. Vernekar, T. Das, S. Ghosh, G. Mugesh, A Remarkably Efficient $MnFe_2O_4$-based Oxidase Nanozyme, Chem. - An Asian J. 11 (2016) 72–76.

[90] X. Zhang, S. He, Z. Chen, Y. Huang, $CoFe_2O_4$ nanoparticles as oxidase mimic-mediated chemiluminescence of aqueous luminol for sulfite in white wines, J. Agric. Food Chem. 61 (2013) 840–847.

[91] Z. Xi, X. Cheng, Z. Gao, M. Wang, T. Cai, M. Muzzio, E. Davidson, O. Chen, Y. Jung, S. Sun, Y. Xu, X. Xia, Strain Effect in Palladium Nanostructures as Nanozymes, Nano Lett. 20 (2020) 272–277.

## CHAPTER 3

## 3. Electrografting of isophthalic acid monolayer and covalent attachment of antibody onto carbon surfaces: construction of capacitive biosensor for methotrexate detection


### Abstract

In this study, a 5-diazonium isophthalic acid (5-DIPA) was synthesized and electrografted onto glassy carbon (GCE) and screen-printed carbon (SPCE) electrodes. SPCE was used to demonstrate fabrication of a miniature device and to compare with conventional glassy carbon electrodes. The isophthalic acid (IPA) electrografted thin film was used for the immobilization of polyclonal anti-methotrexate antibody (anti-MTX-pAb) using carbodiimide activation and coupling chemistry to form antibody modified surfaces, GCE-IPA-anti-MTX-pAb and SPCE-IPA-anti-MTX-pAb. A non-ionic polymer (*N*-[tris(hydroxymethyl)methyl]-acrylamide polymer, polyTHMMAA) was used as a blocking polymer (BP) to block the non-specific binding. After blocking the non-specific binding sites, the electrodes were represented as GCE-IPA-anti-MTX-pAb|BP and SPCE-IPA-anti-MTX-pAb|BP as capacitive biosensors for the detection of methotrexate (MTX) in phosphate buffer pH 7.4 using electrochemical impedance spectroscopy (EIS). The EIS data was analyzed using singular value decomposition (SVD). Principal component regression analysis gave $R^2$ values of 0.99 for both the GCE-IPA-anti-MTX-pAb|BP and SPCE-IPA-anti-MTX-pAb|BP surfaces. The detection limit from the calibration graph of the GCE-IPA-anti-MTX-pAb|BP and SPCE-IPA-anti-MTX-pAb|BP was calculated to be 7.0 pmol.$L^{-1}$ and 5.5 pmol.$L^{-1}$ respectively.


### 3.1 Introduction

Methotrexate (MTX) is an antifolate metabolite that inhibits DNA synthesis and cellular replication [1]. It has been successfully used for the treatment of rheumatoid arthritis (RA) but its most important use is as a chemotherapy agent [2–6]. However, MTX has been found to cause several side effects such as gastrointestinal disorders, hepatic dysregulations, dermatitis, hematologic disorders and nephrotoxicity pneumonitis [1, 7–9]. In chemotherapy, the effective

concentration range of MTX is limited to a relatively narrow therapeutic window, to avoid toxicity towards healthy cells at high concentrations whilst still effective as therapeutic drug at low concentration. The dosage of MTX and its level in the blood needs to be regularly controlled and individualized to establish the dose response and side effects [9]. This is a quest for many researchers pursuing studies towards precision medicine. There is therefore high demand for rapid and highly sensitive methods for monitoring MTX in real time and online. Today, the measurement of MTX in blood samples is often conducted using techniques such as high-performance liquid chromatography (HPLC) [10], oxidative fluorimetry [11], electrospray ionization tandem mass spectroscopy (ESI-MS) [12] and capillary electrophoresis (CE) [13]. These techniques offer high accuracy, sensitivity and selectivity, but they require highly trained personnel, large amount of chemicals, bulky instrumentation and tedious sample preparation. This makes these techniques not amenable for on-site or point-of-care (POC) applications.

Development of alternative methods, based on electrochemical detection, has recently received increased attention [14] and this is due to the low-cost, rapid analysis and the possibility of miniaturization for POC applications. Amongst the various electrochemical methods, electrochemical impedance spectroscopy (EIS) has emerged as a promising technique for biosensor development [15]. EIS offers the possibility for the development of relatively cheap capacitive biosensors that can be miniaturized and used for in-situ analysis. Impedimetric biosensors are either Faradaic or non-Faradaic [16]. The Faradaic impedimetric biosensor comprises a redox probe (label) while the non-Faradaic impedimetric biosensors are label-free and may not need a reference electrode. The biosensors that are based on non-Faradaic EIS are used to monitor the capacitive behaviour of the electrode in the presence of the biomolecule of interest without using a redox probe [17]. Capacitive EIS biosensors are mostly affinity-based sensors, hence attractive for their ability to detect analytes at lower detection limits with high selectivity and sensitivity without sample pre-treatment [17,18]. Their construction involves the immobilization of the recognition element on an electrode where dielectric changes are measured when an analyte binds. The major challenge faced in the design of capacitive biosensors is the immobilization of the bio-recognition layer onto the electrode surface.

Several methods of electrode modification have been exploited including the use of alkylthiols for production of self-assembled monolayers (SAMs) [19] and most recently electrografting with diazonium salts [20–23]. Thin layers are used for the immobilization of the bio-recognition element (the sensing element) that will interact with the target compound. The lack of stability, due to the defects in the formation of thin layers during immobilization of SAMs on the surface, has been challenging [17]. The electrografting of phenyl diazonium is known to form a more stable and reproducible films [22]. However, the formation of the multilayer films causes problems by increasing the initial capacitance of the immunosensor. Therefore, the formation of a more compact and high-quality insulating monolayer thin film with a lower initial capacitance which can attach the bio-recognition element is highly desired.

In this work, we demonstrate a new protocol of electrografting 5-diazonium isophthalic acid (5-DIPA), to promote the formation of a thin monolayer for the immobilization of biorecognition elements. The isophthalic acid (IPA) was electrografted onto glassy carbon (GCE), and screen-printed carbon (SPCE) electrodes for the immobilization of the anti-methotrexate polyclonal antibody (anti-MTX-pAb) and thereby construct a capacitive biosensor for the detection of MTX. Positions 1 and 3 of the benzene rings in the commonly used aryldiazonium salts are prone to the attack by radicals, facilitating the formation of multilayers [24]. In IPA, the carboxylic acid (-COOH) functional groups at positions 1 and 3 sterically hinder radical attachment to the phenyl ring, hence, favouring the formation of monolayers [24-27]. SPCEs were used to realize a low-cost, highly sensitive miniaturized point-of-care (POC) MTX monitoring system. The data analysis of EIS for capacitive monitoring was conducted using singular value decomposition (SVD) analysis as described elsewhere [28-30].

This chapter was set out to achieve the following aims of the thesis:

(a) To develop a label-free capacitive immunosensor by modifying carbon and screen-printed carbon electrode with a stable and electrografted thin film of isophthalic acid
(b) To immobilize anti-MTX-pAb as capture protein for non-Faradaic EIS detection of anti-cancer drug (MTX).

## 3.2 Experimental

### 3.2.1 Material and methods

Methotrexate hydrate (MTX ≥ 99.9%; HPLC grade; sodium hydrogen phosphate trihydrate ($NaH_2PO_4.3H_2O$), sodium hydroxide (NaOH) pellets, potassium chloride (KCl), tetrabutylammonium tetraflouroborate ($TBABF_4$), potassium ferricyanide ($K_3[Fe(CN)_6]$), potassium ferrocyanide ($K_4[Fe(CN)_6]$), N-hydroxysuccinimide (NHS), N-(3-dimethylamino-propyl)-N′-ethylcarbodiimide (EDC), absolute ethanol (EtOH), 5-Aminoisophthalic acid (5-AIPA), tetrafluoroboric acid ($HBF_4$), sodium nitrite ($NaNO_2$), and diethyl ether were purchased from Sigma-Aldrich. Potassium hydroxide pellets (KOH), absolute ethanol (EtOH), acetonitrile (ACN), potassium dihydrogen phosphate ($KH_2PO_4$), and disodium hydrogen phosphate ($Na_2HPO_4$) were purchased from SAARCHEM and used as received. Polyclonal sheep anti-methotrexate antibody (anti-MTX-pAb) of immunoglobulin G (IgG) isotype in a serum format with 0.09% sodium azide was purchased from AbD Serotec through Nordic Biosite (Taby, Sweden). HPLC grade acetonitrile (ACN) was purchased from Fischer Scientific (Bishop Meadow, UK). *N*-[tris(hydroxymethyl) methyl]-acrylamide polymer (polyTHMMAA) was obtained from Technical Research Center (VTT, Finland) and was used as a blocking polymer (BP) for non-specific binding sites on the immunosensing surfaces. All aqueous solutions were prepared using double distilled water or ultra-pure water with a resistivity of 18 MΩ.cm (at 25 °C) obtained from a Milli-Q Water Purification System purchased from Millipore Corporation. Phosphate buffer solution (PhB) pH 7.4 and stock solutions of MTX were prepared following the procedure reported earlier [30]. Briefly, the phosphate buffer (PhB) solution was prepared by dissolving $NaH_2PO_4$ (1.20g, 0.01 mmol) in 1 L of doubly distilled water. The pH was adjusted to the desired pH with NaOH (6.0 $mol.L^{-1}$), and the buffer was filtered before use. Diazonium isophthalic acid (5-DIPA) was synthesized and characterized using FT-IR and $^1H$ NMR as reported in *Sections 3.2.4* and *3.3.1.*

### 3.2.2 Apparatus

Infra-red (FT-IR) spectroscopy was carried out on the ALPHA-T, Bruker machine. $^1H$ NMR was recorded on a Bruker 400 MHz Advance III spectrometer at 298K, using a mixture of 9:1,

$d_6$-DMSO:$D_2O$ as a solvent. Modulab electrochemical system, ECS (Solartron Analytical, UK) was used for electrochemical measurements using a three-electrode setup which comprised glassy carbon electrode (GCE) as a working electrode (WE, diameter = 1.6 mm), silver|silver chloride (saturated KCl) (Ag|AgCl satd KCl) reference electrode (RE) and platinum wire (Pt) as a counter electrode (CE). The SPCE (C110, Dropsen, Metrohm) consisted of a carbon (4 mm diameter) working electrode, carbon counter electrode and silver reference electrode which were printed on ceramic substrate (33 x 10 x 0.50 mm). For the EIS measurements, an applied potential ($E_{app}$ = 0 V) was used in pH 7.4 and the capacitance signal sensitive to the changes in MTX concentrations was monitored. An alternating voltage amplitude of 10 mV, frequency range 65 kHz - 0.50 Hz, with 10 data points/decade was used.

### 3.2.3 Synthesis of 5-diazonium isophthalic acid (5-DIPA), Scheme 3.1

5-DIPA was synthesized using a generic method for the conversion of arylamine to a diazonium salt. Briefly, 5-aminoisophthalic acid (4.8 g, 26.5 mmol) was dissolved in a 20 ml mixture of 48% $HBF_4$ and water in the ratio of 1:1. The solution mixture was allowed to cool in an ice bath with continuous stirring. Water (10 mL) was added to solubilize the precipitate that formed during the cooling and stirring process. After 20 min of cooling and stirring, a concentrated solution of $NaNO_2$ (2.0 g, 28 mmol) dissolved in a minimum amount of water was added dropwise to a stirring solution. The white precipitate that formed was filtered and washed with diethyl ether and dried under vacuum. The product was stored at -20$^0$C in the dark. FT-IR (ν, $cm^{-1}$): 3064 (arC–H), 2270 (-$N^+$≡N), 1691 (C=O), 1570 (C-OH), 1385, 1247 (C-O), 1233, 1071, 1041, 902, 816, 760, 727, 677. $^1$H NMR (f = ppm) ($d_6$-DMSO: $D_2O$ 9:1): 7.93-7.94 (t, 1H, Ar-H); 7.25-7.53 (d, 2H, Ar-H).

### 3.2.4 Fabrication of MTX capacitive immunosensor

#### 3.2.4.1 Electrode pre-treatment

The glassy carbon electrode (GCE) was polished successively with 1.0 µm, 0.30 µm and lastly with 0.0025 µm alumina slurry on Buehler felt pads. After each polishing step, the glassy

carbon electrode was cleaned with a copious amount of ultrapure water. The cleaned GCE was then sonicated in ethanol and ultrapure water for 3 min to remove adsorbed alumina. Carbon electrodes (GCE and SPCE) were pre-treated by cycling in a solution containing 0.50 M $H_2SO_4$ until stable and reproducible scans were obtained. The carbon electrodes were then rinsed with water and dried with a stream of argon or nitrogen gas.

### 3.2.4.2 Electrochemical grafting of 5-DIPA

For electrografting of isophthalic acid (IPA) radical on GCE and SPCE, 2 CV scans were used. The electrografting solution contained 2.50 mmol.$L^{-1}$ 5-DIPA in 3% $H_2SO_4$ acetonitrile solution. Different potential windows were used for electrografting, for GCE (+0.80 *to* -0.50 V) and SPCE (0.00 *to* -1.50 V), scanned at 100 mV.$s^{-1}$ to form GCE-IPA and SPCE-IPA. Both electrografted electrodes were rinsed with ACN and dried with continuous flow of nitrogen gas before subsequent immobilization of the anti-methotrexate polyclonal antibody.

### 3.2.4.3 Immobilization of anti-MTX-pAb onto GCE-IPA

The carboxylic acid functional groups of the grafted isophthalic acid were activated by immersing the GCE-IPA into a 0.10 mmol.$L^{-1}$ PhB (pH 7.4) solution containing 100 mmol.$L^{-1}$ EDC and 20 mmol.$L^{-1}$ NHS for 4 hours at room temperature. The GCE-IPA surface activated with NHS/EDC was then rinsed with PhB and dried with $N_2$ gas. This was followed by incubating of anti-MTX-pAb (85 µL, 0.10 mg.$ml^{-1}$) in PhB at 4 $^0$C overnight. Thereafter, the electrode was washed with PhB to remove unreacted anti-MTX-pAb and dried with a stream of nitrogen or argon gas. The electrode treated with anti-MTX-pAb was represented as GCE-IPA-anti-MTX-pAb and was then exposed to 85 µL of 0.50 mg.$mL^{-1}$ of polyTHMMAA blocking polymer (BP) in PhB for 20 min to minimize non-specific binding yielding GCE-IPA-anti-MTX-pAb|BP. The electrode was finally rinsed with PhB before it was used for the detection of MTX. The SPCE-IPA surface was treated in a similar way and is represented as SPCE-IPA-anti-MTX-pAb|BP.

### 3.2.5 Electrochemical characterization of surface modification

The electrode modification steps were all characterized using CV and Faradaic EIS to assess the blocking effect of the immobilized thin layers. The CV scans were recorded between +0.60 to -0.3 V at 25 $mV.s^{-1}$ in a solution containing 2.5 $mmol.L^{-1}$ of $K_3/K_4[Fe(CN)_6]$ and 0.10 $mol.L^{-1}$ KCl which was used as redox probe solution. A final concentration of 5.0 $mmol.L^{-1}$ for a 1:1 ratio of $K_3[Fe(CN)_6]$ and $K_4[Fe(CN)_6]$ salts was prepared as an equimolar redox probe solution. The redox probe was represented as $[Fe(CN)_6]^{3-/4-}$. This allowed for the ratio of oxidation ($I_{pa}$) to reduction ($I_{pc}$) peak currents to be equal to a unity ($I_{pa}/I_{pc} = 1$) for a reversible redox probe. The CV and EIS experiments were run for the bare, electrografted (IPA) and IPA-anti-MTX-pAb|BP modified carbon surfaces (GCE and SPCE).

### 3.2.6 X-ray photoelectron spectroscopy (XPS) surface characterization

The XPS characterization of the bare and modified surfaces was studied using the flat glassy carbon plates, GC. A Kratos Axis Ultra DLD X-ray Photoelectron Spectrometer having a monochromatic $Al_\alpha$ X-ray source equipped with the charge neutralizer was used for bare and modified surface analysis. The operating pressure was kept below 5.0 x $10^{-9}$ Torr in argon environment. The survey spectra were collected using the following parameters: emission current was kept at 5 mA and the anode voltage at 15 kV; the pass energy was at 80 eV with the width 1200 eV, centre at 596.5 eV, and step size of 1 eV and dwell time of 100 ms. The quantitative analysis of the survey spectra was conducted by measuring the area of the peaks (C 1s, N 1s and O 1s). High resolution spectra were acquired using step size of 0.1 eV and a pass energy of 40 eV. All spectra were normalized using the C 1s as a reference point at 284.9 eV and the curve fitting was done using Vision processing software and Gaussian-Lorentzian peak shape after performing a linear background correction for each of the elements studied.

### 3.2.7 Detection of MTX using Electrochemical Impedance Spectroscopy (EIS)

Electrochemical impedance measurements were made on different concentrations of MTX (in PhB) ranging from 3.0 x $10^{-12}$ $mol.L^{-1}$ to 3.0 x $10^{-4}$ $mol.L^{-1}$. The data was converted to complex

capacitance and analysed using singular value decomposition (SVD) as described elsewhere [28-30]. In brief, EIS measurements were performed using the antibody modified electrodes having the blocking polymer, that is, GCE-IPA-anti-MTX-pAb|BP or SPCE-IPA-anti-MTX-pAb|BP in PhB (pH 7.4) solution containing increasing concentrations of MTX. The experimental run was followed as shown in **Table 3.1**.

**Table 3.1:** Detection of varying concentrations of MXT, experimental setup.

| **Run order** | **Sample** | **[MTX] (mol. $L^{-1}$)** | **(Results in triplicates)** |
|---|---|---|---|
| **1** | PhB | 0 | Establish baseline |
| **2** | MTX 1 | $3.0 \times 10^{-12}$ | Detection |
| **3** | PhB | 0 | Re-establish baseline |
| **4** | MTX 2 | $3.0 \times 10^{-10}$ | Detection |
| **5** | PhB | 0 | Re-establish baseline |
| **6** | MTX 3 | $3.0 \times 10^{-8}$ | Detection |
| **7** | PhB | 0 | Re-establish baseline |
| **8** | MTX 4 | $3.0 \times 10^{-6}$ | Detection |
| **9** | PhB | 0 | Re-establish baseline |
| **10** | MTX 5 | $3.0 \times 10^{-4}$ | Detection |

The EIS data, collected from the runs in **Table 3.1**, was evaluated with SVD for the detection and calibration of [MTX]. In brief, the total impedance (Z) from the EIS data generated was transformed to total capacitance as shown in **Eq.** (**3.1**) below:

$$C = \frac{1}{[j\omega Z]} = C' + jC'' \qquad (\mathbf{3.1})$$

where $j^2$ = -1, ω = 2π*f*; $Z = Z' + jZ''$; $C'$ is the real capacitance and $C''$ is the imaginary capacitance.

Using SVD, the matrix of *C* was decomposed to give **Eq.** (**3.2**) below:

$$C = U_m S_m V_m^* + E = T_m V_m^* + E \qquad (\mathbf{3.2})$$

where $U_m$ is a unitary matrix from the components, $V_m^*$ is the conjugate transpose of $U_m$; $S_m$ is the diagonal matrix of the rectangular values, $T_m$ is a product of $U_m$ and $S_m$ ($Um.Sm$) and E is the residual matrix of noise.

SVD is used to analyze the changes in capacitance, which otherwise is difficult to evaluate using EIS Nyquist plot and conventional circuit fitting. The calibration curve for evaluation of MTX was constructed using **Eq.** (**3.3**):

$$y = [1U_m S_m]b + f \qquad (\mathbf{3.3})$$

where 1 is the all-ones vectors and $U_m$ and $S_m$ is as described above, $b$ is the regression coefficient and $f$ is the vector of residual.

**Equation** (**3.3**) can be simply expressed as **Eq.** (**3.4**):

$$y = [1T]b + f \qquad (\mathbf{3.4})$$

where, $T = U_m.S_m$

In this work, calculations were performed using Matlab (Mathworks Inc., Natick MA).

## 3.3 Results and discussion

### 3.3.1 Synthesis of 5-diazonium isophthalic acid tetrafloroborate (2), Scheme 3.1

The synthesis of 5-DIPA was achieved following the diazotization method in **Scheme 3.1.** Diazotization method involves the reaction of the nitrous acid generated from the dissolved sodium nitrite and the acid present. This reaction produces the nitrosonium ion ($NO^+$). The $NO^+$ electrophile attacks the amine group to form the initial nitrogen-nitrogen bond in the presence of the acid meanwhile breaking the nitrogen-oxygen bond. This results in the expulsion of water and the formation of the nitrogen-nitrogen triple bond, hence forming the diazonium salt [31].

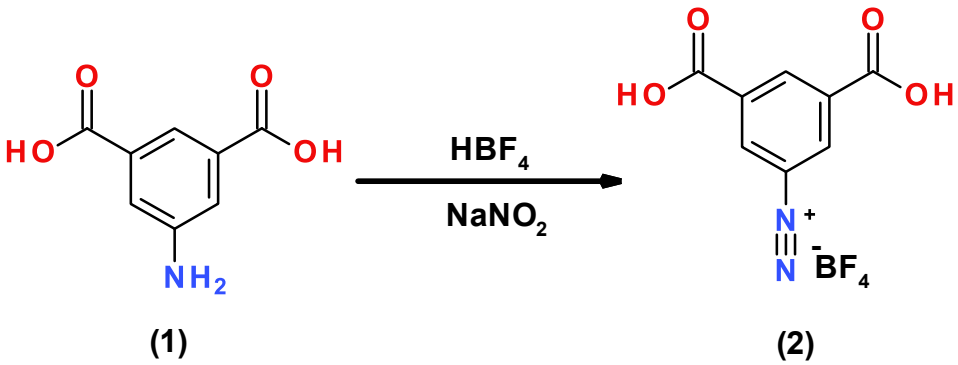


(1) (2)

**Scheme 3.1:** Synthesis of 5-diazoium tetrafluoroborate isophthalic acid salt (5-DIPA, 2) from 5-aminoisophthalic acid (5-AIPA).

**Figure 3.1** shows the FT-IR spectra of (i) 5-aminoisophthalic acid and (ii) 5-diazonium tetrafluoroborate isophthalic acid salt. Upon conversion of the amino functional group, the formation of the diazonium functional group (-N≡N$^{+}$) at 2270 cm$^{-1}$ was observed. The COOH functional groups were not affected by the diazotization reaction and the C=O vibrational bands are observed at 1700 cm$^{-1}$ for both compounds. The fingerprint bands were also observed to have not changed indicating that the parent phenyl ring was not disturbed by the diazotization process.

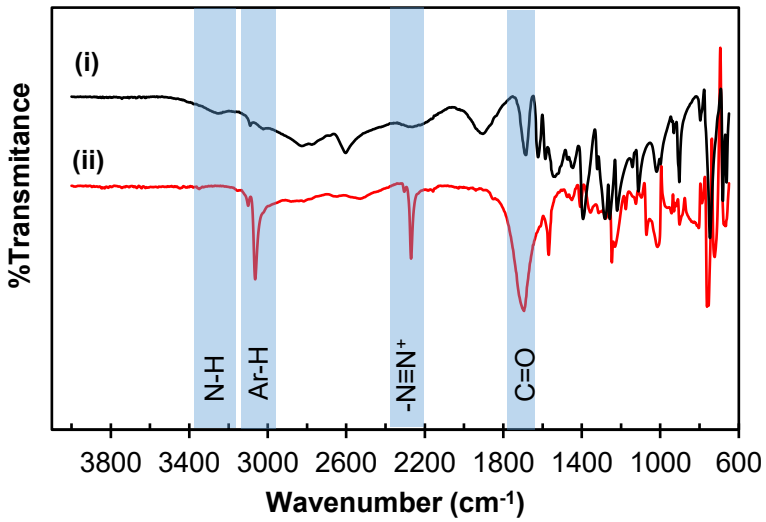


**Figure 3.1:** The FT-IR spectra of (i) 5-aminoisophthalic acid and (ii) 5-diazonium isophthalic acid (5-DIPA).

The FT-IR results above showed functional groups for the successful synthesis of the 5-DIPA, especially the disappearance of $NH_2$ and formation of diazonium salt ($-N^+\equiv N$). The purity of 5-DIPA was confirmed using $^1H$ NMR in **Fig. 3.2** measured in 9:1 $d_6$-DMSO:$D_2O$. The integrated spectrum showed 3 protons for the phenyl ring, with protons labeled **A** and **B** appearing at 7.93 and 7.73 ppm respectively. The spectrum also confirmed the high purity of the 5-DIPA. The proton due to the OH of the carboxylic groups did not show on the spectrum. This was because they were displaced by the sodium ion ($Na^+$) to form the oxygen-sodium ionic bond.

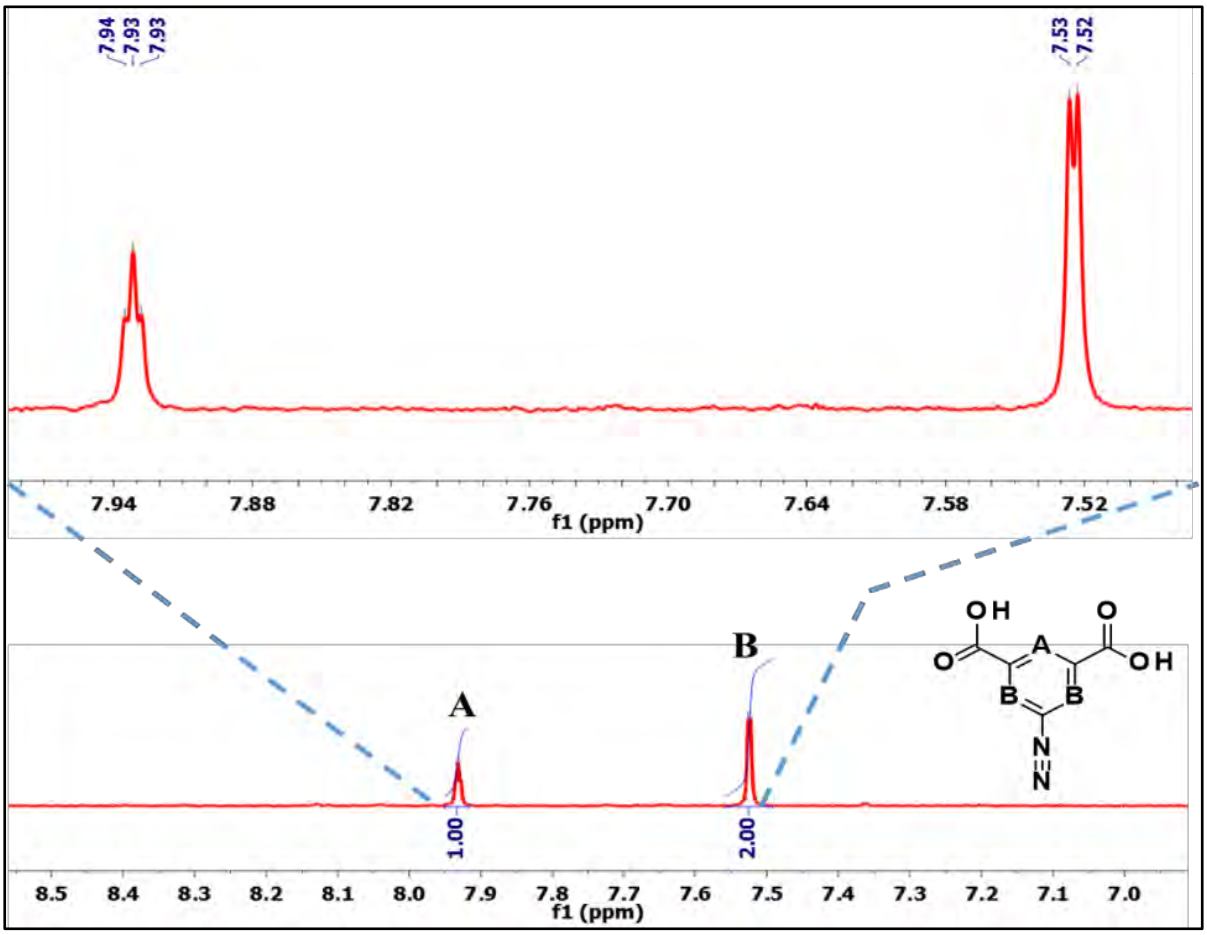


**Figure 3.2:** Proton NMR ($^1H$ NMR) of 5-DIPA measured in a solvent mixture of $d_6$-DMSO and $D_2O$ in the 9:1 volume ration.

### 3.3.2 Immunosensor fabrication

The step-by-step modification of carbon electrodes with 5-DIPA is shown in **Scheme 3.2.** The carboxylic acid modified surface was activated with EDC/NHS to yield an amine reactive ester and the anti-MTX-pAb was immobilized via the amino functional groups at the Fc-terminal. The reaction between the activated carboxylic acid of the IPA modified carbon surfaces and amine functional group on the Fc-region of antibodies was accomplished via carbodiimide chemistry. This yielded an amide bond and covalent immobilization of anti-MTX-pAb antibodies. The amide coupling reaction was performed in PhB at 4°C. The blocking of non-specific binding was achieved using polyTHMMAA (BP) and was used to avoid ionic interference with the anti-MTX-pAb and the MTX. Non-ionic polymers like polyTHMMAA have been used for blocking non-specific bonding sites [29] and allow the selective interaction of anti-MTX-pAb and MTX. The polyTHMMAA is also a hydrophilic polymer [32] and allows for wetting of the electrode surface.

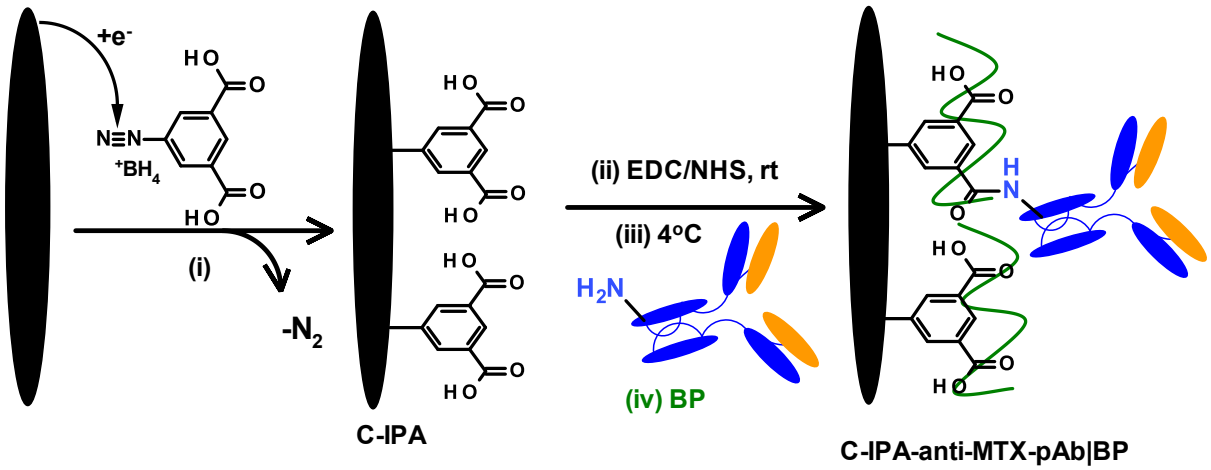


**Scheme 3.2:** Stepwise electrode surface modification, (i) electrografting of 2.5 mmol.L$^{-1}$ 5-DIPA in 3% $H_2SO_4$ in ACN; (ii) carbodiimide activation using EDC/NHS in PhB (pH 7.4) at room temperature; and (iii) covalent immobilization of antibody at 4°C overnight.

### 3.3.3 Electrografting of 5-DIPA onto GCE and SPCE

The first scan in **Fig. 3.3(a)** for GCE shows two reduction peaks at around +0.30 and -0.25 V for the isophthalic acid (IPA) radical generation and grafting onto the GCE surface. The second scan resulted in the reduction of the current density and the disappearance of the two peaks, confirming the electrode modification and passivation. This confirms the formation of the isophthalic acid layer on the glassy carbon electrode to yield a GCE-IPA surface. Similar CVs were observed at SPCE during electrografting but at different potential values, in **Fig. 3.3(b)**. The CV in **Fig. 3.3(b)** for SPCE showed a reduction peak at around -0.70 V for the formation of the aryl radical and the second scan shows a very small peak. This confirmed the electrografting of IPA onto the SPCE to yield SPCE-IPA. The reduction wave was not observed in a solution without 5-DIPA which confirms that the peak was due to the reduction of 5-DIPA to form IPA radicals as shown in **Fig. 3.3 (c)**.

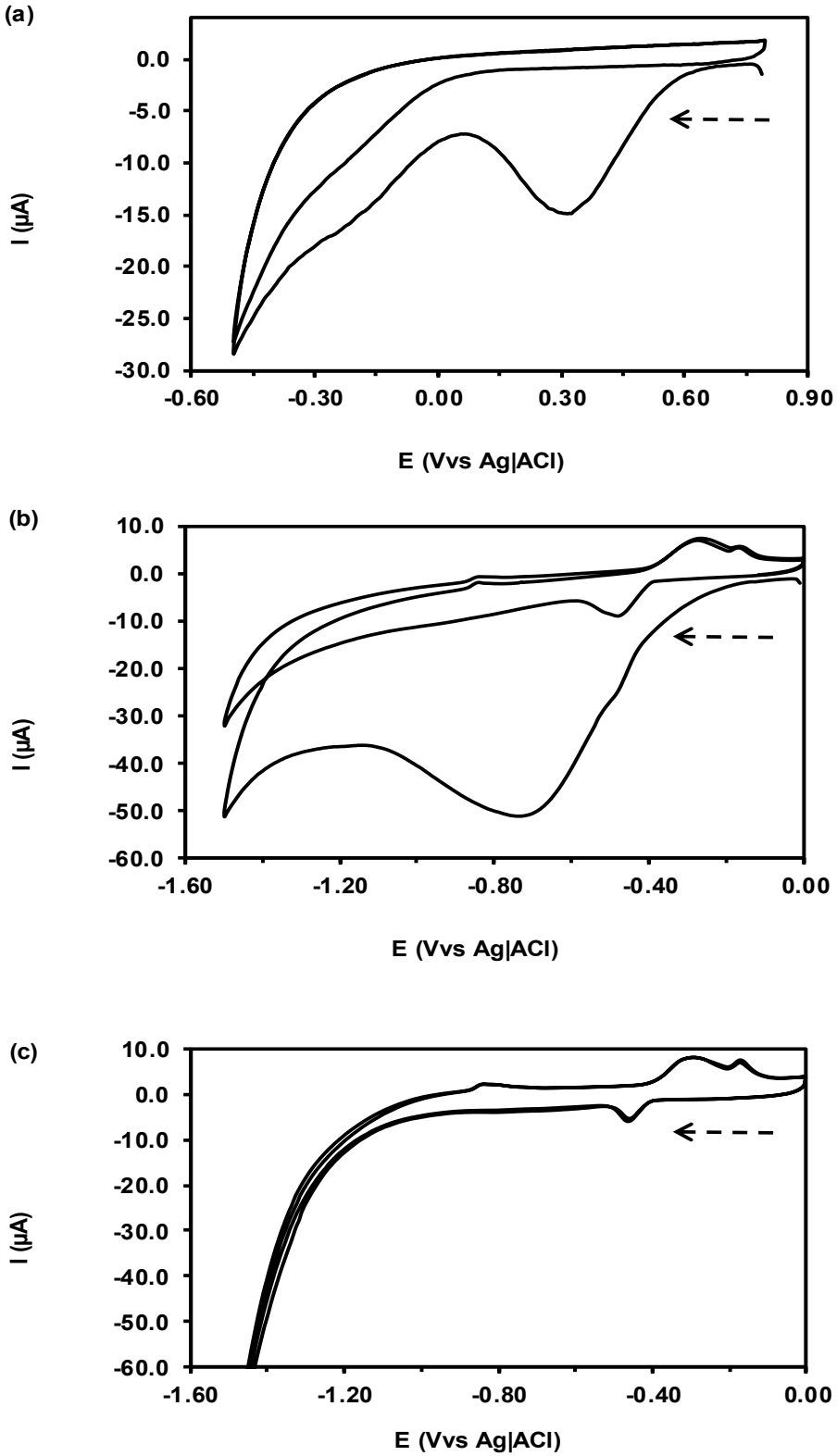


**Figure 3.3:** CVs for the electrografting of 2.50 mmol.$L^{-1}$ of 5-DIPA in 3% $H_2SO_4$ solution of acetonitrile for (a) GCE, (b) SPCE, and (c) SPCE in 3% $H_2SO_4$ in acetonitrile (without 5-DIPA).

The shift in potential from +0.30 V for GCE to -0.70 V for SPCE was attributed to many factors which included (i) different forms of carbon used in the GCE and SPCE, (ii) differences in diameters of GCE (1.6 mm) and SPCE (4.0 mm), (iii) the conductivity kinetics of the carbon surfaces, and (iv) electrolyte used (3% $H_2SO_4$ in acetonitrile). The shift in the reduction potentials on different forms of carbon has been reported before [26] even though not as big as 1 V as observed in this study. The electrodes were treated in the same manner by cycling in 0.50 M $H_2SO_4$ at potential window of −1.5 to +1.0 V at a scan rate of 100 mV.$s^{-1}$ until stable and reproducible scans were obtained. Several measurements were repeated and the differences in potential persisted. This confirmed the electrografting of IPA onto the SPCE to yield SPCE-IPA. The reduction wave was not observed in solution without 5-DIPA which confirmed that the peak was due to the reduction of 5-DIPA to form IPA radicals as shown in **Fig. 3.3(c)**. The surface coverage ($\Gamma_{IPA}$, mol.$cm^{-2}$) of IPA molecules electrografted was estimated to be 3.82 × $10^{-12}$ mol.$cm^{-2}$ for GCE-IPA and 1.17 × $10^{-11}$ mol.$cm^{-2}$ for SPCE-IPA from the area under the reduction peaks in **Fig. 3.3(a)** and **(b)**, respectively, using the following **Eq. (3.5):**

$$\Gamma_{IPA} = \frac{Q}{nFA} \qquad \textbf{(3.5)}$$

where Q (Coulombs, C) is the charge under the reduction peak ($Q_{GCE}$ = 2.61 × $10^{-8}$ C and $Q_{SPCE}$ = 1.14 × $10^{-7}$ C), n is the number of electrons transferred during the reduction of aryl diazonium salt (n = 1), F is the Faraday constant (96485 C.$mol^{-1}$) and A is the surface area of the electrodes for GCE (0.0707 $cm^2$) and SPCE (0.126 $cm^2$). The reduction peak of the aryl radical slightly overestimate the surface coverage as not all the reduced radicals are grafted onto the electrode surface. This still remains a good estimate of the surface coverage. The surface coverage values were much lower than reported for thin monolayer film formation [33] further confirming that the monolayer was obtained.

### 3.3.4 Electrochemical characterization of bare and modified electrodes

The bare and modified GCE surfaces were characterized using CVs in 2.5 mmol.$L^{-1}$ of $[Fe(CN)_6]^{3-/4-}$ solution containing 0.10 mol.$L^{-1}$ of KCl as electrolyte, **Fig. 3.4(a)**. The CV of the bare electrode in **Fig. 3.4(a)(i)**, showed a reversible redox couple with the peak-to-peak separation (ΔE) of 100 ± 10 mV. The current density of the redox couple collapsed after

electrografting, indicating a complete passivation of the electrode and the blocking of the electron transfer as shown in **Fig. 3.4(a)(ii)**. Finally, the immobilization of the anti-MTX-pAb onto the carboxyl-carbodiimide monolayer showed an increase in the blocking of the electron transfer as shown in **Fig. 3.4(a)(iii)**. The changes in CVs confirmed the electrografting of IPA and the subsequent immobilization of antibodies forming GCE-IPA-anti-MTX-pAb|BP. **Figure 3.4(b)** shows CVs obtained in 2.5 mmol.$L^{-1}$ $[Fe(CN_6)]^{3-/4-}$ containing 0.10 mol.$L^{-1}$ KCl for (i) bare SPCE , (ii) SPCE-IPA and (iii) SPCE-IPA-anti-MTX-pAb|BP. **Figure 3.4(b)(i)** shows a redox couple due to $[Fe(CN_6)]^{3-/4-}$ with peak-to-peak separation of 85 ± 3.5 mV. The redox couple disappeared at SPCE-IPA and SPCE-IPA-anti-MTX-pAb|BP surfaces in **Fig. 3.4(b)(ii)** and **(iii)**. The blocking and disappearance of $[Fe(CN_6)]^{3-/4-}$ redox couple confirmed the electrografting and formation of SPCE-IPA and the immobilization of antibodies to form SPCE-IPA-anti-MTX-pAb|BP. The IPA-anti-MTX-pAb|BP modified carbon electrodes have glycoprotein due to anti-MTX-pAb and this has insulating properties. The IPA modified carbon electrodes have COOH terminal functional groups which deprotonates ($-COO^-$) at pH 7.4 which is above the pKa (3.69) value of the carboxylic acid and repels the negatively charged $[Fe(CN_6)]^{3-/4-}$.

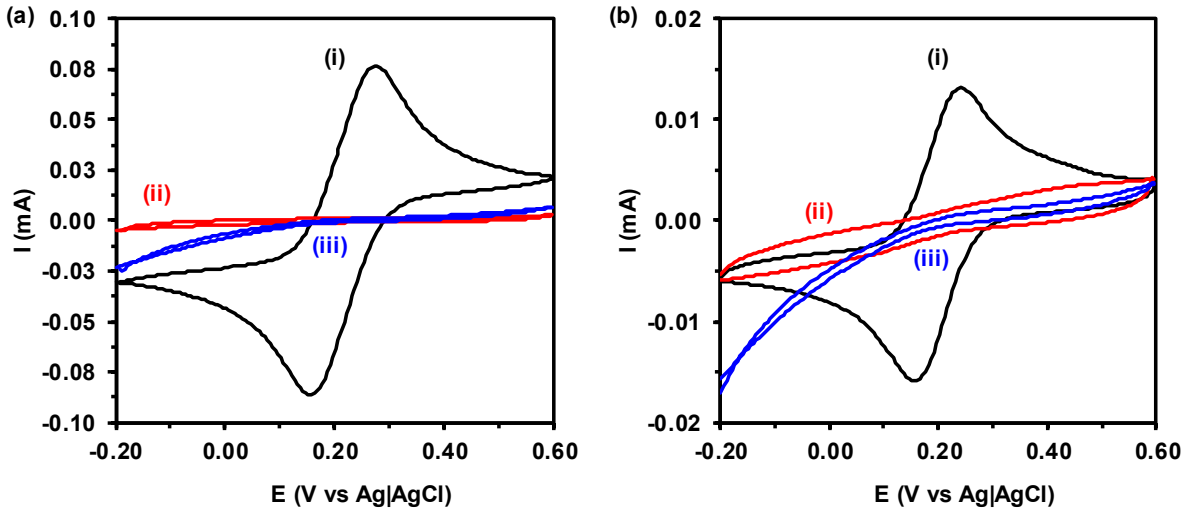


**Figure 3.4:** CVs measured in 2.5 mmol.$L^{-1}$ $[Fe(CN)_6]^{3-/4-}$ containing 0.10 mol.$L^{-1}$ KCl for (i) bare, (ii) C-IPA and (iii) C-IPA-anti-MTX-pAb|BP modified surfaces, where C represent (a) GCE and (b) SPCE.

### 3.3.5 XPS Characterization of Bare and Modified GC Plates

**Figure 3.5** shows the XPS survey spectra of the (i) bare glassy carbon plate (GC), (ii) GC-IPA and (iii) GC-IPA-anti-MTX-pAb|BP. The survey spectrum of bare glassy carbon plates in **Fig. 3.5(i)** contained carbon (C 1s) at 284 eV, nitrogen (N 1s) at 399 eV and oxygen (O 1s) at 529 eV. Due to the cleanliness of the carbon plates, the C 1s dominated the spectrum and had about 95.2% carbon with 3.9% for N 1s and 0.9% for O 1s. After electrografting with isophthalic acid, in **Fig. 3.5(ii)** to form GC-IPA, a 20.3% increase was observed for oxygen O 1s peak from 0.9% for bare GC. This increase in O 1s was accompanied by a decrease in C 1s from 95.2% for bare GC to 77.3% for GC-IPA and N 1s decreased from 3.9% for bare GC to 2.4% for GC-IPA. After the immobilization of antibodies to form GC-IPA-anti-MTX-pAb|BP in **Fig. 3.5(iii)**, an increase in the N 1s from 2.4% for GC-IPA to 10.6% for GC-IPA-anti-MTX-pAb|BP was observed. The increase in the N 1s was attributed to the amino acid, amide and peptide bond residues of the antibody (anti-MTX-pAb). A decrease in the C 1s and O 1s from 77.3% for GC-IPA to 75.5% for GC-IPA-anti-MTX-pAb and from 20.3% to 13.9% for GC-IPA-anti-MTX-pAb|BP was respectively observed. These changes confirmed the electrografting of isophthalic acid and the immobilization of anti-MTX-pAb. To further confirm the various functionalization of the GC, high resolution core-level spectra of C 1s, N 1s and O 1s were investigated.

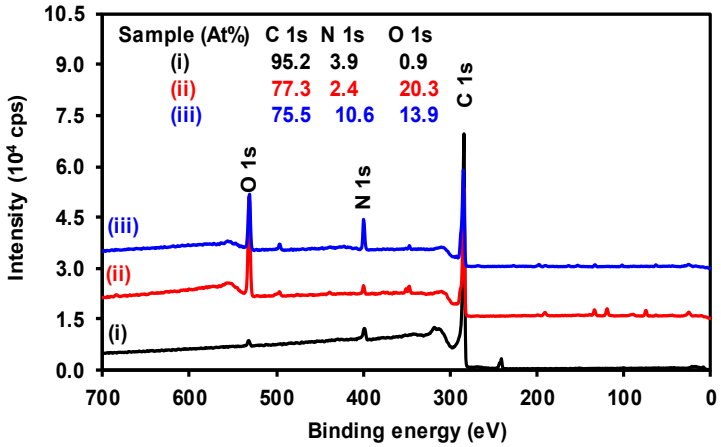


**Figure 3.5:** XPS survey spectra of the (i) bare glassy carbon plate (GC), (ii) GC-IPA and (iii) GC-IPA-anti-MTX-pAb|BP.

**Figure 3.6** shows high resolution core-level spectra of C 1s (left column), O 1s (middle column) and N 1s (right column) for (a) bare, GC, (b) GC-IPA and (c) GC-IPA-anti-MTX-pAb|BP. The high resolution spectra of C 1s in the left column was deconvoluted and four components were synthesized with different compositions and assignments. For the bare GC, the C 1s exhibited an intense component at 284.9 eV due to C-C, C=C and accounting for 59.3%. The same component at 284.9 eV was observed for GC-IPA and GC-IPA-anti-MTX-pAb accounting for 47.5% and 46.5% respectively. The bare GC had very small carboxylic acid component at 289.3 eV (5.6%) and this component increased after electrografting of IPA (GC-IPA) to 14.8% due to the carboxylic groups of isophthalic acid [34-36]. For the GC-IPA, a component at 287.9 eV due to carbonyl (C=O) was also observed to show an increase from 8.4% for bare GC to 12.6% for GC-IPA. The two components at 287.9 eV (C=O) and 289.3 eV (O-C=O) which are due to the carboxylic acid functional groups were scrutinized further. The % component differences for (C=O) increased by 4.2% and for O-C=O the increase was 9.2% from bare GC to GC-IPA. This was an indication of a thin monolayer film of IPA that formed and the ratio of C=O to O-C=O was 1:2.2 clearly confirming the presence of a thin IPA film. For the GC-IPA- anti-MTX-pAb, a further increase in the component at 288.5 eV was observed due to the presence of peptide and amide bonds of the antibody. The carbon components confirm the electrografting of IPA and the immobilization of anti-methotrexate polyclonal antibodies.

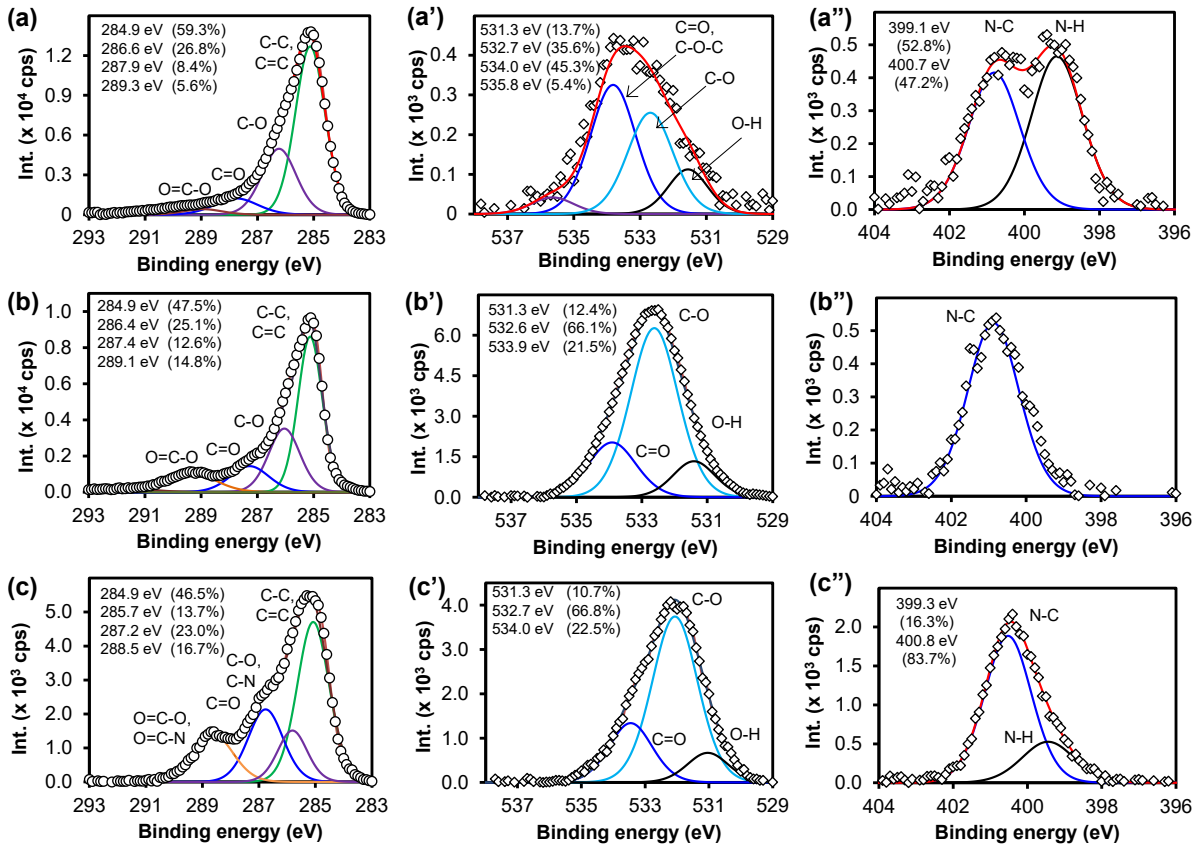


**Figure 3.6:** High resolution core-level spectra of C1s (left column), O1s (middle column) and N1s (right column) for (a) GC, (b) GC-IPA and (c) GC-IPA-anti-MTX-pAb.

The O 1s component, in **Fig. 3.6**, showed distinct changes from **(a')** bare GC to **(b')** GC-IPA and to **(c')** GC-IPA-anti-MTX-pAb. The carbonyl (C=O) component was predominant at 534.0 eV (45.3%) and it decreased sharply to 21.5% after electrografting (GC-IPA). Upon the immobilization of antibodies, the C=O, C-O-C percentage component remained almost the same at 22.5%. The other components at 531.3 eV assigned as O-H showed a very small decreasing effect from 13.7% for GC to 12.4% for GC-IPA and to 10.7% for GC-IPA-anti-MTX-pAb. The components at 532.7 eV increased from 35.6% for GC to 66.1% for GC-IPA and remained the same at 66.8% for GC-IPA-anti-MTX-pAb. The N 1s peak showed very interesting spectral changes. For the bare GC, there was equal number of components at 399.1 eV due to N-H was 52.8% and N-C at 400.7 eV (47.2%) in **Fig. 3.6(a")** for bare GC. After electrografting and formation of GC-IPA, in **Fig. 3.6(b")**, the component at 399.1 eV disappeared. It was interesting to note that the intensity of the component at 400.7 eV did not change and therefore was due to the surface adsorbed nitrogen. At GC-IPA-anti-MTX-pAb, the component at 399.3 eV reappeared with 16.3% in **Fig. 3.6(c")**. The increase in the intensity

of the N 1s components at GC-IPA-anti-MTX-pAb was attributed to the protein amino acids and peptide bonds [37, 38]. The general observed trend reveals that the intensity of the peaks after the immobilization of the anti-MTX polyclonal antibody increased, confirming its immobilization onto the electrode surface.

### 3.3.6 Molecular docking and molecular dynamics simulation conformational analysis

The molecular docking and molecular dynamic simulations were investigated to confirm the conformational analysis of the anti-methotrexate monoclonal antibody (apo protein) before and after binding to the methotrexate (ligand). In-silico docking was studied between the anti-MTX antibody (apo, PDB ID 4OCX) and MTX on the X-ray co-crystal structure. Maestro in the Schrodinger package was used for apo protein preparation as well as LigPrep, and to evaluate the glide ligand score. The crystal structure of the antibody-MTX had a good binding affinity between the anti-MTX monoclonal antibody and the MTX with a docking score of -8.207 kcal.mol$^{-1}$ was lowest docking score and was used to study the protein-ligand interaction.

**Figure 3.7(a)** shows that the MTX pteridine ring had strong hydrophobic and pi-pi interactions with the anti-MTX antibody heavy chain residues **TYR H:99** and **TYR H: 33**. **TYR H:33** also showed hydrophobic and pi-pi interactions with the p-aminobenzoate functional group. The glutamic acid moiety formed hydrogen bonds with antibody light chain residues **LYS L:55** and **TYR L:37**. The pteridine amine (-$NH_2$) functional groups further formed hydrogen bonds (H-bonds) with antibody light chain residue **GLU L:39** and heavy chain residue **ASN H:36**. The best antibody and MTX docking with the lowest docking score of -8.207 kcal.mol$^{-1}$ shown in **Fig. 3.7(b)** was selected for the molecular dynamics (MD) studies. Two different simulations were calculated, the antibody alone (anti-MTX-pAb) and the antibody (MTX), anti-MTX-pAb (MTX). The Radius of gyration (Rg) and Root Mean Square Deviation (RMSD) were evaluated over 100 ns. **Figure 3.7(c)** shows the radius of gyration as a measure of structural conformation. The antibody alone in **Fig. 3.7 (c)(i)** showed high Rg when compared to the antibody (MTX) Rg. The MTX, in the antibody (MTX) in **Fig. 3.7 (c)(ii)** stabilized the protein-ligand leading to low Rg. This confirms that when the antibody interacts with the MTX, the structural conformation of the antibody occurs. For the electrochemical measurements, the MTX binding site of the antibody is facing the solution away from the electrode surface for enhanced

interaction. The conformational changes of the antibody have significance in the detection of MTX as compact antibody-MTX forms. The RMSD in **Fig. 3.7(d**) for antibody and the antibody (MTX) complex reached convergence respectively within the 20 ns in **Fig. 3.7 (d)(i)** and 45 ns in **Fig. 3.7(d)(ii)**.

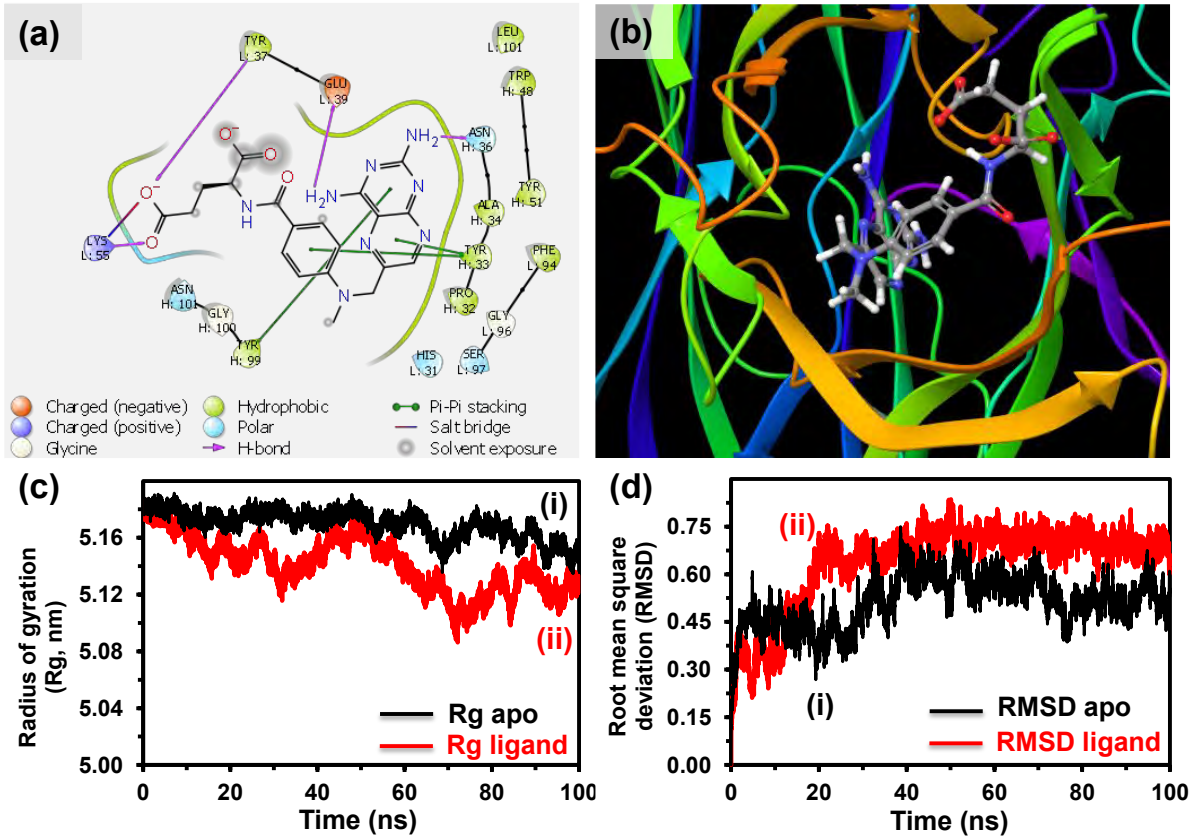


**Figure 3.7:** (a) Anti-methotrexate monoclonal antibody-MTX interactions, antibody [PDB ID: 4OCX]. (b) Docking pose of crystal antibody and MTX. Stability of (i) anti-methotrexate monoclonal antibody (Ab) and (ii) anti-MTX-pAb(MTX) interaction determined by (c) Rg and (d) RMSD.

### 3.3.7 Detection of MTX using modified GCE/SPCE-IPA-anti-MTX-pAb|BP

The detection of MTX is based on bio-affinity interaction of MTX with the anti-MTX-pAb on the GCE/SPCE-IPA-anti-MTX-pAb|BP in PhB pH 7.4. The presence of MTX in the sample brought about conformational changes of the immobilized antibody as shown in **Fig. 3.7**, which

upon binding results in capacitance changes. The capacitance of the electrochemical impedance data showed significant changes in the presence and absence of MTX when SDV was used for data evaluation. The changes in the absence and presence of MTX was monitored using EIS. The impedance changes are very small to be evaluated by Nyquist plot and circuit fitting. Therefore, SVD was used to analyse the data and elucidate the capacitive charges. The applied potential was 0.0 V allowing the monitoring of only the capacitance changes upon binding. The data analysis using SVD has been described and discussed earlier [28-30]. The previous work was based on grafting with salt of 4-diazonium benzoic acid (4-DBA) in which multilayers formed. In this work, the monolayer of IPA was formed with the blocking of the *meta*-(1,3)-positions with carboxylic acid functional groups.

#### 3.3.7.1 Detection of MTX on GCE-IPA-anti-MTX-pAb|BP

**Figure 3.8** shows the score plots obtained from the analysis of EIS data using SVD, for the detection of MTX using GCE-IPA-anti-MTX-pAb|BP. The score plots showed both diagonal and vertical separation in the absence and presence of MTX for the concentrations ranging from 3.0 x $10^{-12}$ mol.$L^{-1}$ to 3 x $10^{-4}$ mol.$L^{-1}$. This confirmed that the immunosensor can detect presence of MTX and the first component, u(1), accounted for 99.9% contribution and the second component, u(2), showed vertical separation and accounted for about 0.1% contribution. The separation on the GCE-IPA-anti-MTX-pAb|BP between the blank PhB and the MTX containing solutions were due to the binding between MTX and anti-MTX antibody (Ab) immobilized on the electrode surface. The observed changes in capacitance were due to the changes in the conformation of the anti-MTX antibody upon binding with MTX. An increase in the concentration of MTX resulted in an increase in changes of capacitance.

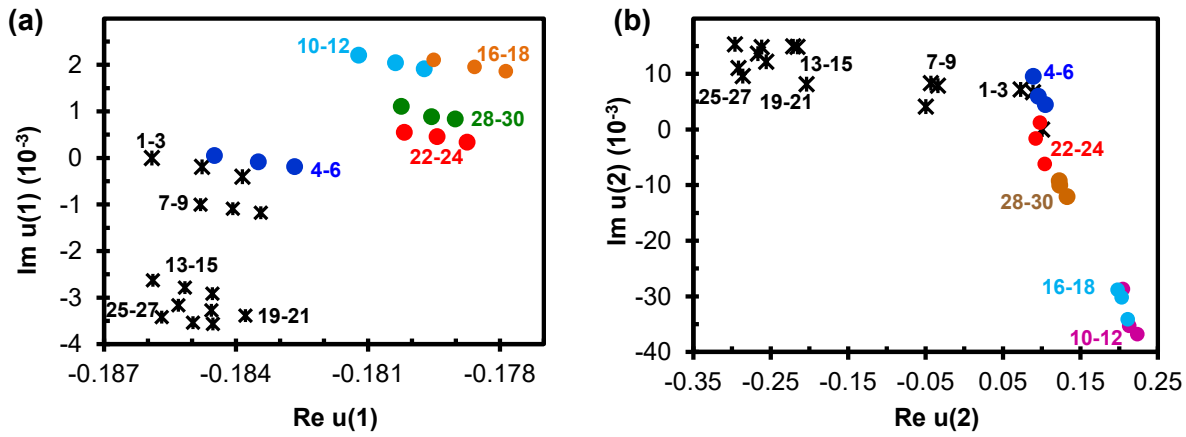


**Figure 3.8:** SVD score plots for the (a) first u(1 and (b) second u(2) components of the imaginary (Im) and real (Re) scores for GCE-IPA-anti-MTX-pAb|BP, PhB alone (black asterisk) and varying concentrations of MTX ranging from 3.0 x $10^{-12}$ mol.$L^{-1}$ to 3.0 x $10^{-4}$ mol.$L^{-1}$ (colour).

### 3.3.7.2 Detection of MTX on SPCE-IPA-anti-MTX-pAb|BP

**Figure 3.9** shows SVD score plots obtained for SPCE-IPA-anti-MTX-pAb|BP blocked with blocking polymer in PhB (black asterisks) and varying concentrations of MTX (3.0 x $10^{-12}$ mol.$L^{-1}$ to 3.0 x $10^{-4}$ mol. $L^{-1}$). The score plot of the first component, u(1) in **Fig. 3.9(a),** shows a very clear diagonal separation between the blank and the MTX confirming that the sensing surface responds to the presence of MTX. The first component accounted for 99.8% contribution. It is also worth noting that the separation was clearly visible on the SPE-IPA-anti-MTX-pAb|BP compared to the GCE-IPA-anti-MTX-pAb|BP. This might be attributed to the well-insulated layer formed on the SPCE which favoured the non-Faradaic process. The second component, u(2) in **Fig. 3.9(b)** showed clear separation between the blank and MTX solutions containing different concentrations and accounted for 0.2% contribution. This confirmed that MTX can be detected by the immobilized antibody and the surface can be regenerated for online continuous monitoring. Since the antibody was covalently attached, the sensor can be reused several times without loss of antibody binding strength.

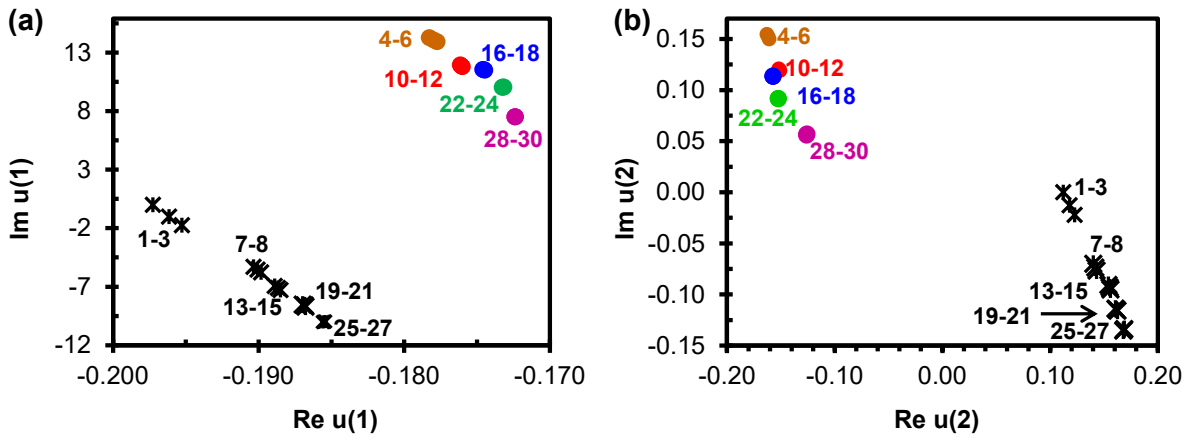


**Figure 3.9:** SVD score plots for the (a) first u(1) component and (b) second u(2) component of the imaginary (Im) and real (Re) scores of SPCE-IPA-anti-MTX-pAb|BP in PhB alone (black asterisks) and MTX concentrations ranging from 3.0 x $10^{-12}$ mol.$L^{-1}$ to 3 x $10^{-4}$ mol.$L^{-1}$ in colour.

The effect of non-specific binding on the SPCE-IPA-anti-MTX-pAb without the blocking polymer for the detection of MTX was studied. **Figure 3.10** shows the SVD score plots obtained for SPCE-IPA-anti-MTX-pAb sensing electrode without the blocking polymer at varying concentrations of MTX (3.0 x $10^{-12}$ mol.$L^{-1}$ to 3.0 x $10^{-4}$ mol.$L^{-1}$). The black asterisk (*) were the data points for PhB alone and the coloured dots were data points of PhB containing varying concentrations of MTX. The score plots were observed to be random, and no trend could be observed, and this was due to the MTX interacting with the electrode surface as a result of non-specific interaction. Unlike when the blocking polymer was used, the score plot of the first component, u(1) in **Fig. 3.9**, shows that there was a clear difference and separation between PhB containing MTX and when PhB was used alone. The SPCE-IPA-anti-MTX-pAb|BP in **Fig. 3.9** showed a drifting of plots in the diagonal direction in both the blank PhB and MTX, indicating that no non-specific binding occurred for MTX at the SPCE-IPA-anti-MTX-pAb|BP. The second component, u(2) in **Fig. 3.9(b)** showed the same trend, although the drifting was observed to be at an angle of rotation 90 degrees clockwise. In **Fig. 10**, the non-separation of the plots in the blank (PhB) and in the presence of MTX could be explained by the non-specific binding of the MTX to both the anti-MTX-pAb antibody and to the unblocked reactive sites on the immunosensor.

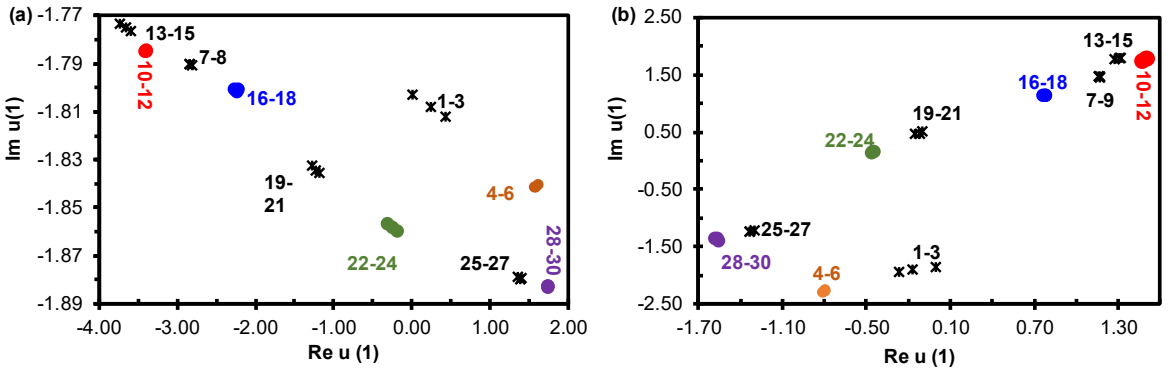


**Figure 3.10:** SVD score plots for the (a) first u(1) component and (b) second u(2) component of the imaginary (Im) and real (Re) scores of SPCE-IPA-anti-MTX-pAb|BP without the blocking polymer in PhB alone (black asterisks) and MTX concentrations ranging from 3.0 x $10^{-12}$ mol.L$^{-1}$ to 3 x $10^{-4}$ mol.L$^{-1}$ in colour.

The calibration graphs shown in **Fig. 3.11(a,b)** were constructed using the principal component regression (PCR) as described previously [25]. PCR calibration analysis gave $R^2$ values of 0.99 for both GCE-IPA-anti-MTX-pAb|BP and SPCE-IPA-anti-MTX-pAb|BP confirming excellent correlation between theoretical and measured concentration of MTX. The detection limit from the calibration curves of the GCE-IPA-anti-MTX-pAb|BP and SPCE-IPA-anti-MTX-pAb|BP was calculated to be 7.0 pmol.L$^{-1}$ and 5.5 pmol.L$^{-1}$ respectively. The limits of detection were both comparable with reported studies [25–27] while the $R^2$ showed a decrease in the relative error, hence, making this protocol developed in here more desirable. The reproducibility in terms of percentage relative standard deviation (%RSD) obtained for the lowest concentration using the SPCE-IPA-anti-MTX-pAb|BP was 1.14% and much better than for the GCE-IPA-anti-MTX-pAb|BP which was 4.23%.

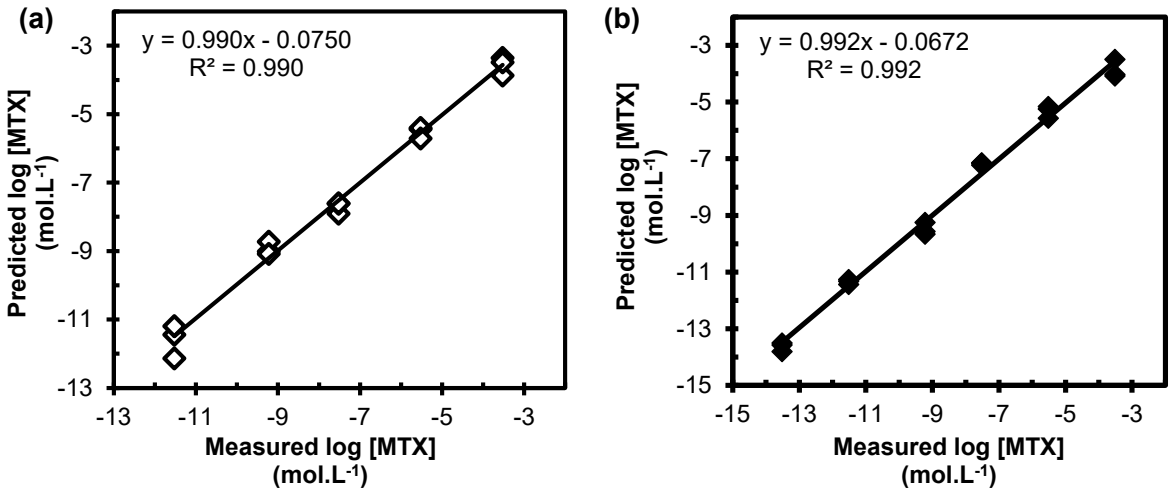


**Figure 3.11:** The calibration graphs (a) GCE-IPA-anti-MTX-pAb|BP and (b) SPCE-IPA-anti-MTX-pAb|BP response towards the changes in concentrations of MTX ranging from 3 x $10^{-12}$ to 3 x $10^{-4}$ mol.$L^{-1}$.

### 3.4 Conclusions

In this work, we presented a new protocol of surface modification for electrografting a thin monolayer film of isophthalic acid (IPA) on carbon surfaces: glassy carbon electrode (GCE) and screen-printed carbon electrode (SPCE). The GCE/SPCE-IPA modified surfaces were activated with carbodiimide to immobilize anti-methotrexate (MTX) antibody to form GCE/SPCE-IPA-anti-MTX-pAb. The stepwise modification and immobilization of antibodies on the electrode surfaces was confirmed by CV and XPS. The sensor surfaces containing anti-MTX antibodies were used for capacitive detection of methotrexate (MTX) and this was accomplished using SVD for data analysis. The MTX interacted with the immobilized anti-MTX antibody leading to antibody conformation changes and changes in capacitance. Molecular dynamics (MD) confirmed the conformational changes of the anti-methotrexate antibody alone and after binding to the MTX (anti-MTX-pAb/MTX). These conformational changes were observed electrochemically using sensitive impedance measurements for the detection of MTX. The changes in capacitance increased with increasing concentration of MTX for both GCE-IPA-anti-MTX-pAb|BP and SPCE-IPA-anti-MTX-pAb|BP. The detection limits for GCE and SPCE were found to be 7.0 pmol.$L^{-1}$ and 5.5 pmol.$L^{-1}$ respectively. The $R^2$ values were much close to a unity (0.99), confirming that the developed method was more reliable.

The possibility of miniaturization, ease of use, and the reproducibility of obtained results makes the screen-printed carbon electrodes more attractive for extending their application for determination of MTX online and in clinical samples.

### 3.5 References


[1] W. Wang, H. Zhou, L. Liu, Side effects of methotrexate therapy for rheumatoid arthritis: A systematic review, Eur. J. Med. Chem. 158 (2018) 502–516.

[2] H. Tian, B.N. Cronstein, Understanding the mechanisms of action of methotrexate: Implications for the treatment of rheumatoid arthritis, Bull. NYU Hosp. Jt. Dis. 65 (2007) 168–173.

[3] E.S.L. Chan, B.N. Cronstein, Methotrexate how does it really work?, Nat. Rev. Rheumatol. 6 (2010) 175–178.

[4] E.S.L. Chan, B.N. Cronstein, Mechanisms of action of methotrexate, Bull. Hosp. Joint Dis. 71 (2013) S5–S8.

[5] J.J. Wang, L.F. Sinks, Treatment of Acute Lymphocytic Leukemia by High-Dose Intravenous Methotrexate, Cancer Res. 36 (1976) 1441–1444.

[6] A.D.R. Pontinha, S.M.A. Jorge, V.C. Diculescu, M. Vivan, A.M. Oliveira-Brett, Antineoplasic Drug Methotrexate Redox Mechanism Using a Glassy Carbon Electrode, Electroanalysis. 24 (2012) 917–923.

[7] G.S. Alarcóan, I.C. Tracy, W.D. Blackburn, Methotrexate in rheumatoid arthritis. Toxic effects as the major factor in limiting long-term treatment, Arthritis Rheum. 32 (1989) 671–676.

[8] M.J.H. Wijnands, M.A. Van't Hof, M.A. Van Leeuwen, M.H. Van Rijswijk, L.B.A. Van De Putte, P.L.C.M. Van Riel, Long-term second-line treatment: A prospective drug survival study, Rheumatology. 31 (1992) 253–258.

[9] A.M. Boerbooms, P.J. Kerstens, J.W. van Loenhout, J. Mulder, L.B. van de Putte, Infections during low-dose methotrexate treatment in rheumatoid arthritis, Semin. Arthritis Rheum. 24 (1995) 411–421.

[10] H. Li, W. Luo, Q. Zeng, Z. Lin, H. Luo, Y. Zhang, Method for the determination of blood methotrexate by high performance liquid chromatography with online post-

column electrochemical oxidation and fluorescence detection, J. Chromatogr. B Anal. Technol. Biomed. Life Sci. 845 (2007) 164–168.

[11] H.C. Chen Suming, Zhang Zhujun, He Deyong, Hu Yufei, Zheng Huzhi, Abstracts of the XIIth International Symposium on Luminescence Spectrometry Detection Techniques in Biomedical , Environmental and Food Analysis (ISLS 2006) Determination of benzimidazole fungicides by coupling solid-phase microextraction and, Luminescence. (2007) 320–386.

[12] I. Rodin, A. Braun, A. Stavrianidi, O. Shpigun, A validated LC-MS/MS method for rapid determination of methotrexate in human saliva and its application to an excretion evaluation study, J. Chromatogr. B Anal. Technol. Biomed. Life Sci. 937 (2013) 1–6.

[13] N.R. Roach, c mark; Gozel, Philippe;Zare, Determination of methotrexate and its major metabolite, 7-hydroxymethotrexate, using capillary zone electrophoresis and laser-induced fluorescence J. Chromatogr. 426 (1988) 129–140.

[14] S. Kummari, V.S. Kumar, M. Satyanarayana, K.V. Gobi, Direct electrochemical determination of methotrexate using functionalized carbon nanotube paste electrode as biosensor for in-vitro analysis of urine and dilute serum samples, Microchem. J. 148 (2019) 626–633.

[15] T. Bertok, L. Lorencova, E. Chocholova, E. Jane, A. Vikartovska, P. Kasak, J. Tkac, Electrochemical Impedance Spectroscopy Based Biosensors: Mechanistic Principles, Analytical Examples and Challenges towards Commercialization for Assays of Protein Cancer Biomarkers, ChemElectroChem. 6 (2019) 989–1003.

[16] R.A. Dorledo de Faria, L.G. Dias Heneine, T. Matencio, Y. Messaddeq, Faradaic and non-Faradaic electrochemical impedance spectroscopy as transduction techniques for sensing applications, Int. J. Biosens. Bioelectron. 5 (2019) 29–31.

[17] C. Berggren, B. Bjarnason, G. Johansson, Capacitive biosensors, Electroanalysis. 13 (2001) 173–180.

[18] C. Berggren, B. Bjarnason, G. Johansson, Instrumentation for direct capacitive biosensors, Instrum. Sci. Technol. 27 (1999) 131–140.

[19] V.M. Mirsky, M. Riepl, O.S. Wolfbeis, Capacitive monitoring of protein immobilization and antigen-antibody reactions on monomolecular alkylthiol films on gold electrodes, Biosens. Bioelectron. 12 (1997) 977–989.

[20] D. Bélanger, J. Pinson, Electrografting: A powerful method for surface modification, Chem. Soc. Rev. 40 (2011) 3995–4048.

[21] A. Adenier, M.-C. Bernard, M.M. Chehimi, E. Cabet-Deliry, B. Desbat, O. Fagebaume, J. Pinson, F. Podvorica, Covalent Modification of Iron Surfaces by Electrochemical Reduction of Aryldiazonium Salts, J. Am. Chem. Soc. 123 (2001) 4541–4549.

[22] D. Hetemi, V. Noël, J. Pinson, Grafting of diazonium salts on surfaces: Application to biosensors, Biosensors. 10 (2020) 4-36.

[23] D. Mwanza, S. Mvango, S. Khene, T. Nyokong, P. Mashazi, Exploiting Click Chemistry for the Covalent Immobilization of Tetra (4-Propargyloxyphenoxy) Metallophthalocyanines onto Phenylazide-Grafted Gold Surfaces, Electrochim. Acta. 254 (2017) 89-100.

[24] C. Combellas, F. Kanoufi, J. Pinson, F.I. Podvorica, Sterically hindered diazonium salts for the grafting of a monolayer on metals, J. Am. Chem. Soc. 130 (2008) 8576–8577.

[25] K. Tahara , Y. Kubo , B. Lindner , S. Hashimoto , S. Hirose , A. Brown , B. Hirsch , L. Daukiya , S. De Feyter , Y. Tobe , Steric and electronic effect of electrochemi- cally generated aryl radicals on grafting of the graphite surface, Langmuir 35 (2019) 2089–2098 .

[26] J. Greenwood , T.H. Phan , Y. Fujita , Z. Li , O. Ivasenko , W. Vanderlinden , H. Van Gorp , W. Frederickx , G. Lu , K. Tahara , Y. Tobe , H. Uji-I , S.F.L. Mertens , S. De Feyter , Covalent Modification of Graphene and Graphite Using Diazo- nium Chemistry: Tunable Grafting and Nanomanipulation, ACS Nano 9 (2015) 5520–5535

[27] L. Gillan, T. Teerinen, L.S. Johansoon , M. Smolander , Controlled diazonium electrodeposited towards biosensor for C-reactive protein, Sens. Int. 2 (2021) 10060 .

[28] S. Tesfalidet, P. Geladi, K. Shimizu, B. Lindholm-Sethson, Detection of methotrexate in a flow system using electrochemical impedance spectroscopy and multivariate data analysis, Anal. Chim. Acta. 914 (2016) 1–6.

[29] S. Phal, B. Lindholm-Sethson, P. Geladi, A. Shchukarev, S. Tesfalidet, Determination of methotrexate in spiked human blood serum using multi-frequency electrochemical immittance spectroscopy and multivariate data analysis, Anal. Chim. Acta. 987 (2017) 15–24.

[30] S. Phal, B. Shatri, A. Berisha, P. Geladi, B. Lindholm-Sethson, S. Tesfalidet, Covalently electrografted carboxyphenyl layers onto gold surface serving as a platform for the construction of an immunosensor for detection of methotrexate, J. Electroanal. Chem. 812 (2018) 235–243.

[31] V. Roman, Diazotization (Diazonium salt), in: V. Roman, Organic Chemistry:100 Must-Know Mechansms, De Gruyter, 2020:pp. 82-83

[32] N. T. H. Bui, W. Jiang, T. Smarman, K. Irgun, Synthesis of poly(N-[tris(hydroxymethyl)methyl]acrylamide) functionalized porous silica fr application in hydrohylic interaction chromatography, J. Sep. Sci. 35 (2012) 3257 – 3269.

[33] T. Menanteau , E. Levillain , A.J. Downard , T. Breton , Evidence of monolayer formation via diazonium grafting with a radical scavenger: electrochemical, AFM and XPS monitoring, Phys. Chem. Chem. Phys. 17 (2015) 13137--13142 .

[34] S. Phal, K. Shimizu, D. Mwanza, P. Mashazi, A. Shchukarev, S. Tesfalidet, Electrografting of 4-carboxybenzenediazonium on glassy carbon electrode: The effect of concentration on the formation of mono and multilayers, Molecules. 25 (2020) 4575-4586.

[35] C.S. Kam, T.L. Leung, F. Liu, A.B. Djurišić, M.H. Xie, W.K. Chan, Y. Zhou, K. Shih, Lead removal from water-dependence on the form of carbon and surface functionalization, RSC Adv. 8 (2018) 18355–18362.

[36] L.Z. Fan, S. Qiao, W. Song, M. Wu, X. He, X. Qu, Effects of the functional groups on the electrochemical properties of ordered porous carbon for supercapacitors, Electrochim. Acta. 105 (2013) 299–304.

[37] E. Desimoni, B. Brunetti, X-ray Photoelectron Spectroscopic characterization of chemically modified electrodes used as chemical sensors and biosensors: A review, Chemosensors. 3 (2015) 70–117.

[38] X. Zong, N. Kong, J. Liu, W. Yang, M. Cao, J.J. Gooding, The influence of graphene on the electrical communication through organic layers on graphite and gold electrodes, Electroanalysis. 26 (2014) 84–92.

# CHAPTER 4

## 4. Label-free Capacitive Immunosensor Based on a Stable Thin-film Monolayer of Isophthalic Acid for Detection of Prostate-Specific Antigen


### Abstract

A rapid, low-cost, and accurate point-of-care analytical device for the determination of prostate-specific antigen (PSA) is highly required for the early diagnosis and prognosis of prostate cancer. In this chapter, an ultrasensitive electrochemical capacitive immunosensor was developed for the label-free detection of prostate-specific antigen. The immunosensor was based on the covalent immobilization of monoclonal anti-PSA antibody onto gold electrode pre-modified with a thin monolayer of isophthalic acid (IPA). A methodology based on the steric hindrance of 1,3-substituted aryldiazonium salt was adopted to control the growth of the IPA monolayer on the gold electrode. The monoclonal anti-PSA antibodies were immobilized onto the IPA monolayer via carbodiimide chemistry. The non-specific binding sites were blocked with bovine serum albumin (BSA) to afford an AuE-IPA-anti-PSA-mAb|BSA immunosensor. The immunosensor was characterized by, X-ray photoelectron spectroscopy (XPS), cyclic voltammetry (CV), and electrochemical impedance spectroscopy (EIS). The analytical performance of the developed sensor was validated using Nyquist plots and the capacitance was generated from the complex impedance data. In addition, complex capacitance was also calculated from the imaginary part of the impedance and plotted against the log of frequency. The double layer capacitance from the circuit fitting ($R_SC$) was also used to compare the detection signal sensitive to the changes in PSA concentrations. All the three data analysis techniques used showed an excellent linear range between 10.0 $fg.mL^{-1}$ to 0.10 $mg.mL^{-1}$. The LOD was found to be 2.30 $fg.mL^{-1}$, 76.0 $pg.mL^{-1}$, and 33.0 $pg.mL^{-1}$ for the Nyquist plots of capacitance, complex capacitance, and double layer capacitance from the circuit fitting ($R_SC$); respectively. The developed immunosensor exhibited good stability, selectivity, low detection limits, and a wide linear range which was suitable for screening of prostate cancer.

## 4.1 Introduction

Prostate cancer (PCa) is the most frequently diagnosed cancer in men, accounting for about 1.4 million cases and 375,000 death worldwide in 2020 [1]. The detection of PCa at an early stage is vital for effective curative surgery and an improved survival rate. The five-year survival rate of metastatic PCa is less than 30 %, while the survival rate is about 98 % if detected early [2]. Digital rectum examination (DRE) and quantification of prostate-specific antigen (PSA) levels are the clinically approved methods for screening and diagnosis of prostate cancer. However, the accuracy of DRE depends on the doctor's skill, and its invasive procedure makes it unsuitable for mass screening of incipient cancer [3]. The quantification of serum PSA concentration is the most preferred method for early-stage detection and monitoring of relapse after treatment due to the non-invasive nature of the analysis.

PSA is a 34-kDa serine protease produced by prostatic epithelium and secreted into the seminal fluid to break grown semenogelins I and II proteins. A total PSA (t-PSA) level of less than 4.0 $ng.mL^{-1}$ is present in the blood of a healthy man [4]. Elevated serological levels of PSA have been correlated with the development of PCa. PSA levels in the diagnostic grey zone range from 4.0 to 10 $ng.mL^{-1}$ and indicate a 25 to 40% probability of developing PCa. PSA levels greater than 10 $ng.mL^{-1}$ is a conclusive indication of PCa in about 67% of men [5]. Therefore, monitoring the rate of increase in PSA levels is vital in the clinical diagnosis of PCa. On such a basis, various PSA immunoassays, including enzyme-linked immunosorbent assay (ELISA) [6], radioimmunoassay [7], mass spectroscopy [8], fluorescence immunoassay [9], chemiluminescence [10,11], and photoelectrochemical immunoassay [12,13] have been developed for the quantification of serological PSA levels. These methods are quite complicated due to expensive equipment, laborious procedures, long turn-around time, and the requirement of a specialized analyst, which limits their applicability at point-of-care [14]. Therefore, developing a portable point-of-care testing (POCT) device to streamline the diagnostic process and ensure real-time, effective, and efficient patient care is an unmet need in the clinical management of PCa.

A suitable approach to overcome the challenges of conventional PSA immunosensors is desirable. Electrochemical impedance spectroscopy (EIS) based-immunosensor was investigated due to its operational simplicity, miniaturizability, label-free and rapid response. EIS could either be in a Faradaic or non-Faradaic mode. Faradaic EIS relies on a redox probe

(such as ferricyanide/ferrocyanide) and the application of a DC voltage to initiate the redox reaction at the immunoelectrode/electrolyte interface. In immunosensors that use Faradaic impedance, resistance to charge transfer ohmic current indicates the immunocomplex formation at the immunoelectrode surface. Faradaic impedance thus requires an additional design strategy to incorporate the redox probe, making it unsuitable for POCT applications. However, non-Faradaic impedance measures the dielectric changes, local conductance, and charge distribution due to the immunocomplex formation at the electrode surface [15,16], which results in changes in the electrochemical capacitance. The non-Faradaic impedance (capacitive) immunosensor does not require a redox probe and application of DC, making it more suitable for POCT.

The chemical modification of the working electrode for covalent immobilization of the biorecognition element is an essential factor in developing a stable, sensitive, and accurate capacitive immunosensor [17–19]. Self-assembled monolayer (SAMs) [20], electropolymerization of a conductive polymer [21], and electrochemical grafting of phenyl diazonium derivatives are commonly used methods for the fabrication of chemically modified electrodes [22]. Among these methods, electrografting has gained more research attention because it forms more stable and reproducible films [23]. However, the electrografting of phenyl diazonium often results in the formation of multilayer thick films of up to 100 nm [24, 25]. The formation of the thick films has presented a challenge in developing ultrasensitive capacitive sensors [26]. Literature reports that capacitive sensors are more sensitive to interfacial changes within 10 nm [27] of the film thickness. Therefore, controlling the formation of thin film via electrografting of the substituted phenyl group is required to achieve a highly sensitive and stable capacitive POCT immunosensor for PSA detection.

Herein, we present a novel label-free capacitive non-Faradaic immunosensor for PSA based on a thin monolayer film of isophthalic acid (IPA) electrografted onto a gold (AuE) electrode forming AuE-IPA. Electrografting of AuE with 1,3-isophthalic acid groups would prevent multilayer formation due to carboxylic acid (-COOH) substituents at positions 1 and 3 of the diazonium benzene ring as discussed in chapter three. An important phenomenon that was not explored and discussed in earlier literature [28]. The capacitive PSA biosensor was fabricated by covalent attachment of the anti-PSA monoclonal antibody via the terminal amino groups to the monolayer carboxylic acid groups to form AuE-IPA-anti-PSA-mAb immunoelectrode. The fabricated immunoelectrode was characterized using electrochemical methods, and X-ray photoelectron spectroscopy (XPS). The non-Faradaic electrochemical impedance

spectroscopic (EIS) data was converted to electrochemical capacitance Nyquist plots using our accustomed written MATLAB program. The Nyquist plots were then used to assess the analytical performance of the fabricated sensor towards serological PSA. The assessment of the analytical performance of the sensor developed was also conducted using the complex capacitance and the double layer capacitance obtained from the imaginary impedance and the circuit fitting ($R_S$ C), respectively.

This chapter was set out to achieve the following aims of the thesis:

(c) To fabricate a label-free capacitive immunosensor based on a stable thin-film monolayer of isophthalic acid onto gold electrode
(d) To immobilize anti-PSA monoclonal antibody for non-Faradaic EIS detection of PSA.

## 4.2. Experimental

### 4.2.1. Chemicals and reagents

Potassium ferricyanide $K_3[Fe(CN)_6]$, potassium ferrocyanide $K_4[Fe(CN)_6]$, hexaammine ruthenium(II) chloride $[Ru(NH_3)_6]Cl_2$, hexaammine ruthenium(III) chloride $[Ru(NH_3)_6]Cl_3$, 98% sulfuric acid ($H_2SO_4$), sodium chloride (NaCl), N-hydroxysuccinimide (NHS), N-(3-dimethylaminopropyl)-N'-ethyl carbodiimide (EDC), tetrabutylammonium tetrafluoroborate ($TBABF_4$), and potassium chloride (KCl) were obtained from Sigma-Aldrich (South Africa). Potassium hydroxide pellets (KOH), absolute ethanol (EtOH), acetonitrile (ACN), potassium dihydrogen phosphate ($KH_2PO_4$), and disodium hydrogen phosphate ($Na_2HPO_4$) were purchased from SAARCHEM and used as received. The monoclonal anti-prostate specific antibodies (anti-PSA-mAb), and prostate-specific antigens (PSA) were purchased from Bio-Rad Laboratory Ltd. All aqueous solutions were prepared using double distilled water or ultra-pure water with a resistivity of 18 MΩ.cm (at 25 °C) obtained from a Milli-Q Water Purification System purchased from Millipore Corporation. Detection of PSA was performed in freshly prepared phosphate buffer saline solution (PBS) pH 7.4. The 5-diazonium isophthalic acid (5-DIPA) was prepared as reported in chapter 3 and stored at -20 $^0$C.

### 4.2.2. Apparatus

Cyclic voltammetry (CV) and electrochemical impedance spectroscopy (EIS) measurements were performed using AUTOLAB PGSTAT302N Potentiostat/Galvanostat electrochemical workstation equipped with a NOVA 1.10 software. A conventional three-electrode system, consisting of a bare or modified gold electrode (AuE, r = 0.8 mm, A = 0.0201 $cm^2$) as the working electrode (WE), a platinum wire as a counter electrode (CE), and a silver-silver chloride (Ag|AgCl) pseudo-reference electrode.

### 4.2.3. Fabrication of AuE-IPA-anti-PSA-mAb|BSA immunosensor

**Scheme 4.1** shows the fabrication process of the AuE-IPA-anti-PSA-mAb|BSA immunosensor. Before the modification, the bare gold electrode was cleaned and polished to a mirror finish using 1.0 µm, 0.30 µm, and 0.050 µm alumina slurry on a polishing pad. The polished electrode was ultrasonicated with ethanol and ultra-pure water to remove residual alumina. The gold surface was then cleaned in a "piranha" solution comprising 1:3 (v/v) 30% $H_2O_2$ and concentrated 98% $H_2SO_4$ for 2 min to remove organic contaminants and then rinsed with a copious amount of water and absolute ethanol. The gold electrode was electrochemically cleaned by continuous scanning in 0.50 M $H_2SO_4$ between -0.50 to +1.0 V (versus Ag|AgCl pseudo-reference or Ag|AgCl in 3.0 M KCl) until reproducible scans were obtained. Then, the clean gold surface was rinsed with ultra-pure water and dried with a stream of nitrogen gas.

The cleaned AuE was immersed in an acetonitrile solution containing 5-DIPA (0.15 mg, 2.5 mmol) and $TBABF_4$ (0.16 mg, 0.10 mol) as supporting electrolyte. The electrografting was done by cyclic voltammetry within a potential window between +0.60 to -0.25 V at a scan rate of 100 $mV.s^{-1}$. The isophthalic acid grafted gold electrode (AuE-IPA) was then cleaned with acetone and ultra-pure water to remove physically adsorbed 5-DIPA. The AuE-IPA electrode was dried and immersed into a mixed solution of EDC (0.10 mol. $L^{-1}$) and NHS (20 $mmol.L^{-1}$) in PBS (pH 7.4) for 1 h at room temperature to activate the carboxylic acid groups to a reactive NHS ester to form Au-IPA-NHS modified electrode. Then, the AuE-IPA-NHS was rinsed with PBS and dried with $N_2$. The AuE-IPA-NHS was incubated with 100 µL of monoclonal anti-

PSA-mAb (20 µg.mL$^{-1}$) at 4°C overnight to yield AuE-IPA-anti-PSA-mAb. Afterward, the AuE-IPA-anti-PSA-mAb was incubated in 100 µL of PBS (pH 7.4) containing BSA (10 mg.mL$^{-1}$) for 30 mins to block residual unreactive NHS groups and non-specific adsorption on the AuE surface to form AuE-IPA-anti-PSA-mAb|BSA immunosensor. The electrode was rinsed with PBS (pH 7.4) to remove unreacted BSA. The electrode was stored at 4°C. It was then allowed to thaw at room temperature and subsequently in pH 7.4 PBS before use.

### 4.2.4 Electrochemical characterization

The electrode modification steps were all characterized using CV and EIS to assess the blocking effect of the immobilized layer using potassium ferricyanide and ruthenium hexamine buffered with phosphate buffer at pH 7.0 as redox probes. The formation of an isophthalic acid thin monolayer film was also confirmed with CV and EIS using potassium ferri/ferrocyanide at pH 4.0, pH 7.0, and pH 8 in phosphate buffer. The typical setup involved immersing electrodes in 2.5 mmol L$^{-1}$ of $[Fe(CN)_6]^{3-/4-}$ or $[Ru(NH_3)_6]^{2+/3+}$, the solution containing 0.10 mol L$^{-1}$ of KCl as an electrolyte. CV was performed using a potential window of +0.60 to -0.30 V for potassium ferricyanide and +0.10 to -0.40 for ruthenium hexamine at a scan rate of 100 mV.s$^{-1}$ for all the electrode surfaces studied.

### 4.2.5 Non-Faradaic capacitive detection of PSA

The non-Faradaic capacitive detection of PSA was done by carrying out EIS measurement with the modified gold electrode in standard PSA solutions of increasing concentrations at a DC potential of 0.0 V vs Ag|AgCl. The measurements were done with the blank solution of 1.0 mM PBS before incubation of the electrode in PBS containing a known concentration of PSA. After the EIS measurement in a known PSA solution, the electrode was immersed in 2.0 M glycine hydrochloric acid for 2 min to regenerate the sensing platform. The electrode was washed thoroughly with ultra-pure water before immersing in PBS for 60 min and before a subsequent measurement.

## 4.3. Results and discussion

### 4.3.1 Fabrication and characterization of AuE-IPA-anti-PSA-mAb|BSA, Scheme 4.1

The schematic representation of the fabrication of the AuE-IPA-anti-PSA-mAb|BSA immunosensor is shown in **Scheme 4.1**. In the first step, a thin monolayer film of isophthalic acid was formed on the AuE via electrochemical grafting of a 5-diazoniumisophthalic acid (5-DIPA). Uncontrolled electrochemical grafting of aryldiazonium salts often results in an insulating thick multilayer film [29] that is undesirable for immunosensing applications. The multilayer formation is usually due to the grafting of aryl radicals substituted at *para* or 4th position on the benzene ring [25,30,31]. In this work, we showed the formation of an electrografted thin monolayer film of IPA on the gold electrode and its use for the fabrication of label-free capacitive immunosensor for the detection of PSA.

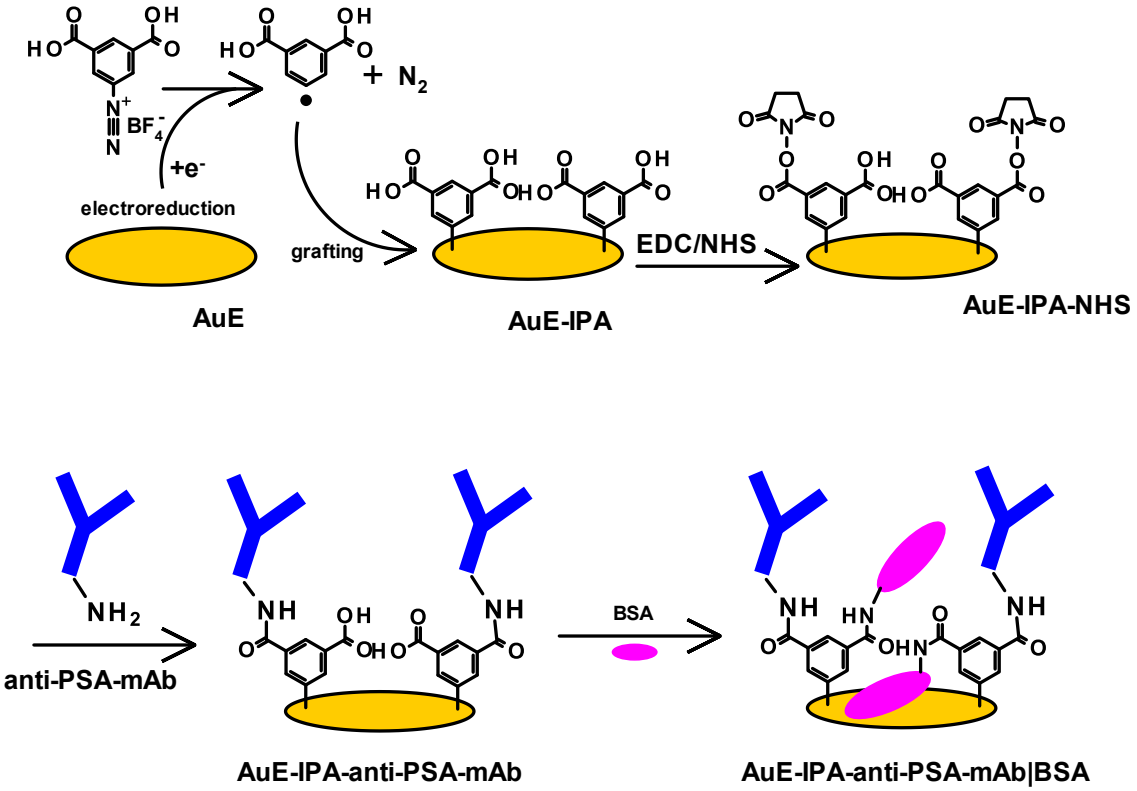


**Scheme 4.1:** Step-by-step fabrication of AuE-IPA-anti-PSA-mAb|BSA immunosensor.

#### 4.3.1.1 Characterization of AuE-IPA monolayer

**Figure 4.1** (a) shows the CVs of AuE in acidified ACN solution containing 2.5 mmol. $L^{-1}$ of 5-DIPA and 50 mmol.$L^{-1}$ of $TBABF_4$. The CVs in **Fig. 4.1** (a) show a broad irreversible peak at 0.35 V vs Ag|AgCl. The cathodic peak was due to one-electron transfer electroreduction of 1,3-isophthalic acid diazonium salt leading to the subsequent formation of an isophthalic acid radical and loss of nitrogen molecule. The isophthalic acid radical was covalently grafted to AuE, forming the AuE-IPA monolayer. The cathodic current densities decreased gradually during the second and subsequent scans. This indicated that the AuE-IPA surface was not completely passivated on the first scan and grafting of IPA radical continued to take place on the unmodified areas of the electrode surface during the subsequent scans. The carboxylic acid groups at positions 1 and 3 of the benzene ring prevented further grafting of the IPA radical onto the already grafted IPA layer on the AuE, leading to the formation of an IPA thin monolayer film grafted onto gold electrode (AuE-IPA). The observation was similar to previously reported electrografting of diazonium salt-containing bulky tertbutyl groups at positions 1 and 3 [31]. The electroreduction response (ERR%) calculated as the percentage of the charge ratio between the first and subsequent scans. **Equation (4.1)**, was used to observe the progress of electrografting of IPA on the gold electrode.

$$ERR\% = \frac{Q_{1^{st}}}{Q_{n^{th}}}\ x\ 100 \qquad \textbf{(4.1)}$$

where $Q_{1^{st}}$ is the charge under the area of the reduction wave of the first scan and $Q_{n^{th}}$ is the charge under the area of the reduction wave of the 2$^{nd}$ and nth scans.

**Figure 4.1** (b) highlights the elelctroreduction response as a percentage (ERR%) of the charge calculated after integrating the area under the reduction wave of the active AuE with the first scan taken as 100% response. It was observed that the ERR% decreased with the increasing number of scans. This suggested the slowing of the electron transfer rate during the subsequent grafting of IPA onto the AuE. The curve was further observed to flatten from 20 scans and above. The flattening of the ERR% indicated the formation of the IPA thin monolayer film which was thin enough to reduce the diazonium salt in solution. The thin monolayer film prevented further grafting of the IPA radicals onto the formed IPA monolayer as discussed above. The surface concentration of the IPA molecules grafted onto the gold electrode was

calculated from a modified equation shown in **Eq. (4.2)** and was found to be 1.78 x $10^{-10}$ mol.cm$^{-2}$.

$$\Gamma_{modified} = \frac{\frac{Q_{1}st}{Q_{20}th} x\, A_{AuE}\ (cm^2)}{A_{IPA}(cm^2.(molecule)^{-1})\ x\ N_A(molecule.mol^{-1})\ x\ A_{AuE}\ (cm^2)} \qquad \textbf{(4.2)}$$

where, $Q_{1}st$ and $Q_{20}th$ are the average (n = 5) charge of the reduction wave, of the 1$^{st}$ and 20$^{th}$ scan respectively, $A_{AuE}$ is the geometric surface area of the unmodified gold electrode (0.0201 cm$^2$), $A_{IPA}$ is the estimated surface area of the IPA (74.6 Å) optimized using Agadros software, $N_A$ is the Avogadro's constant.

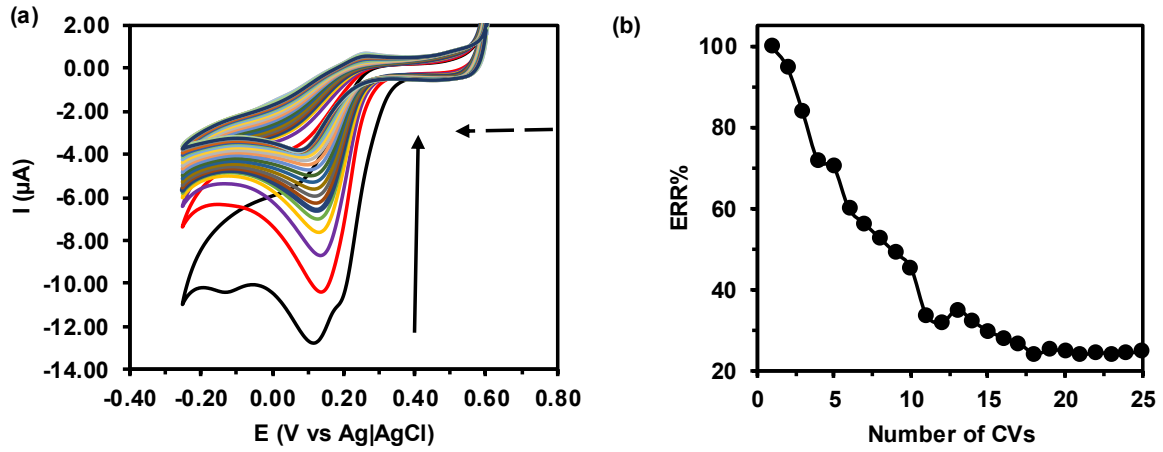


**Figure 4.1:** (a) Electrografting of AuE in acidified ACN solution containing 2.5 mmol.L$^{-1}$ 5-DIPA and 50 mmol.L$^{-1}$ $TBABF_4$ at 100 mV.s$^{-1}$, and (b) percentage electroreduction response (ERR%) with respect to the number of scans.

Dimensional analysis of **Eq. (4.2)** gives the resultant unit of mol.cm$^{-2}$ which corresponds with the units when the conventional surface concentration was calculated using **Eq. (4.3)** as shown in the literature [32].

$$\Gamma = \frac{Q}{nFA} \qquad \textbf{(4.3)}$$

where Q (C) is the charge under the reduction wave, (n = 1) is the number of electrons transferred, F is the Faraday constant (C.mol$^{-1}$) and A is the area of the bare gold electrode

(0.0201 $cm^{-1}$). **Equation (4.2)** offers a facile method of determining the surface concentration of the electrografted compound without the need for post functionalization of the monolayer as observed when **Eq. (4.3)** is used. The surface concentration was observed to be lower than the ones calculated when the same concentration of the unsubstituted aryldiazonium salts were electrografted [32]. This was attributed to the formation of a thin monolayer film which also spaces apart due to the presence of the polar headgroups of carboxylic acid on positions 1 and 3 of the IPA moiety formed on the gold electrode.

#### 4.3.1.2 Electrochemical characterization of the AuE, AuE-IPA and AuE-IPA-anti-PSA-mAb|BSA

The electrochemical blocking behavior of the bare Au, AuE-IPA and AuE-IPA-anti-PSA-mAb|BSA surfaces was studied using $[Fe(CN)_6]^{3-/4-}$ and $[Ru(NH_3)_6]^{2+/3+}$ which are negatively and positively charged redox probes respectively, in PBS (0.10 M, pH 7.0) at a scan rate of 100 $mV.s^{-1}$. **Figure 4.2** shows the CVs and EIS Nyquist plots of (a) $[Fe(CN)_6]^{3-/4-}$ and (b) $[Ru(NH_3)_6]^{2+/3+}$ in 0.10 M PBS at pH 7.0 for (i) bare AuE, (ii) IPA electrografted electrode (AuE-IPA), and (iii) immunosensor (AuE-IPA-anti-PSA-mAb|BSA). The CVs in **Fig. 4.2(a)** indicated that there was a decrease in the peak currents ($I_p$) for the redox probe $[Fe(CN)_6]^{3-/4-}$ from (i) AuE to (ii) AuE-IPA surface. The decrease in the peak curerents was accompanied by the increase in the peak-to-peak separation (ΔE) from 83 ± 5 mV for AuE to 103 ± 5 mV for AuE-IPA. The decrease in peak currents was higher when the AuE-IPA was modified with the anti-PSA-mAb and BSA to yield AuE-IPA-anti-PSA-mAb|BSA. The ΔE increased further from 103 ± 5 mV for AuE-IPA to 136 ± 4 mV for AuE-IPA-anti-PSA-mAb|BSA. Both the increase in ΔE and the decrease in the peak currents from the bare gold electrode to the immunosensor were attributed to the successful electrografting of IPA and the subsequent immobilization of the anti-PSA-mAb. The changes in both the ΔE and $I_p$ were small from surface to surface indicating that the immobilized layer was ultrathin. The corresponding EIS Nyquist plots in **Fig. 4.2** (a') shows that the charge transfer resistance ($R_{CT}$) characterized as the diameter of the semi-circle increased from that of the AuE (0.21 $k\Omega.cm^{-2}$), to 0.51 $k\Omega.cm^{-2}$ for AuE-IPA and further to 0.65 $k\Omega.cm^{-2}$ for AuE-IPA-anti-PSA-mAb. This observation confirmed the successful immobilization of the anti-PSA-mAb onto the AuE-IPA. The $R_{CT}$

increased further with the immobilization of BSA to yield AuE-IPA-anti-PSA-mAb|BSA (0.70 kΩ $cm^{-2}$) confirming the blocking of the unreacted AuE-IPA-NHS.

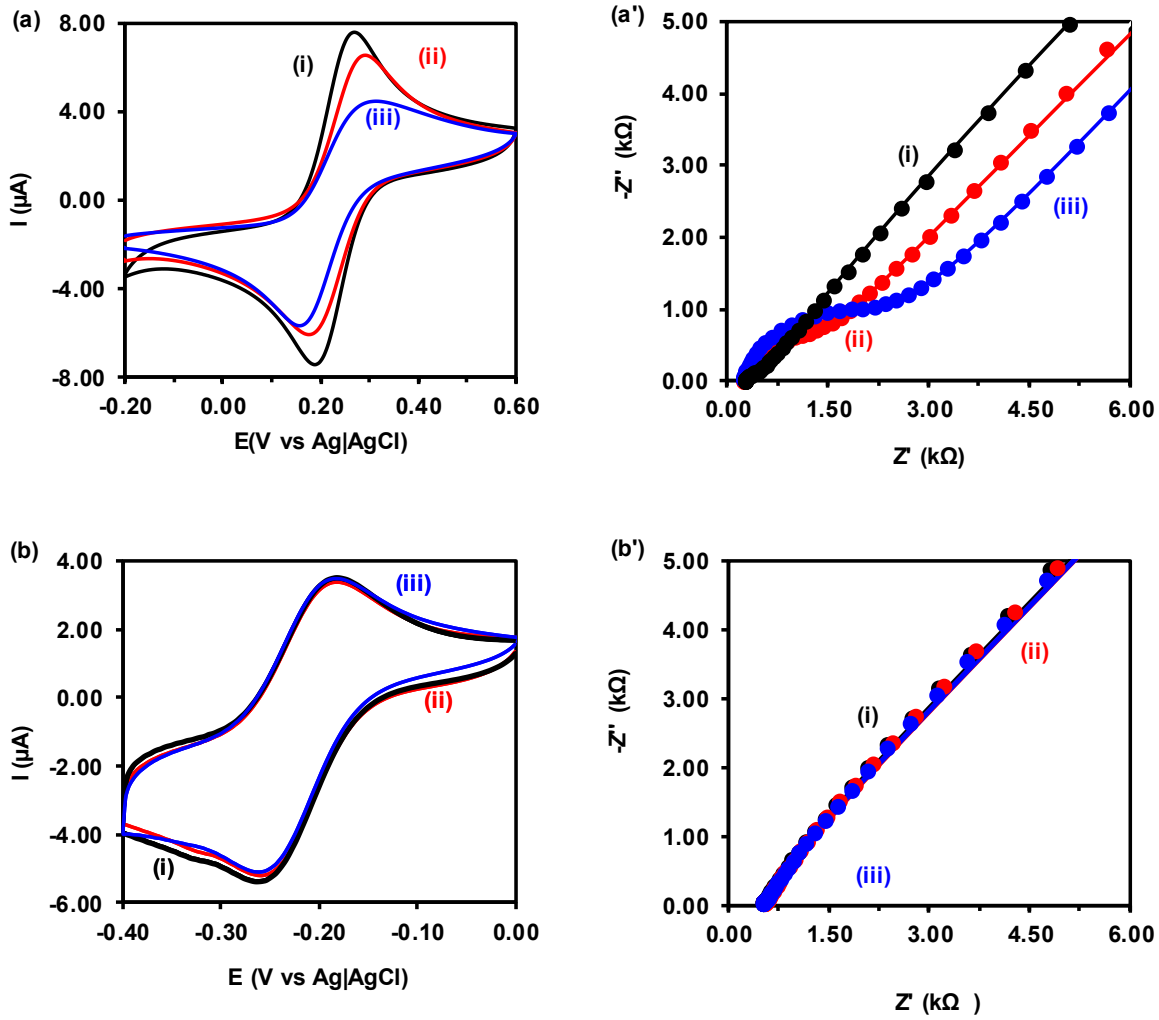


**Figure 4.2:** CVs and their corresponding Nyquist plots of (i) AuE, (ii) AuE-IPA and AuE-IPA-anti-PSA-mAb|BSA in 2.5 mmol $L^{-1}$ of (a) $[Fe(CN)_6]^{3-/4-}$ , (b) $[Ru(NH)_6]^{2+/3+}$ in 0.10 M PBS (pH 7.0). Scan rate: 100 $mVs^{-1}$.

Meanwhile, the CVs and their corresponding EIS Nyquist plots in **Fig. 4.2**(**b**) and (**b'**) for the $[Ru(NH_3)_6]^{2+/3+}$ as a positive probe showed no significant change in both the ΔE, $I_p$, and $R_{CT}$ for AuE, AuE-IPA, and AuE-IPA-anti-PSA-mAb|BSA surfaces. This confirmed that both the AuE-IPA and AuE-IPA-anti-PSA-mAb|BSA surfaces had the same electrochemical effect as the AuE towards $[Ru(NH_3)_6]^{2+/3+}$ probe at pH 7.0. The observed difference in electrochemical blocking behavior of both AuE-IPA and AuE-IPA-anti-PSA-mAb|BSA surface towards

positively ($[Ru(NH_3)_6]^{2+/3+}$) and negatively ($[Fe(CN)_6]^{3-/4-}$) charged probes can be attributed to the repulsive and attractive effect between the electrode surface and the redox probes as previously observed in the literature [33]. The pKa value of the AuE-IPA monolayer is closer to that of its parent compound, 5-aminoisophthalic acid (pKa = 3.69) [34]. At pH 7.0 which is above pH 3.6, the carboxylic acid groups on the AuE-IPA thin monolayer film is expected to deprotonate to form $COO^-$, thereby, causing the repulsion against $[Fe(CN)_6]^{3-/4-}$. The repulsion causes the slowing down of the electron transfer as compared to the AuE. On the other hand, the negatively charged AuE-IPA surface causes the attractive forces towards $[Ru(NH_3)_6]^{2+/3+}$ positively charged probe and due to the migration and diffusion mass transport. It was not strange that the AuE-IPA-anti-PSA-mAb|BSA surface behaved similarly as the AuE-IPA surface towards the $[Fe(CN)_6]^{3-/4-}$ and $[Ru(NH_3)_6]^{2+/3+}$. This is because the BSA on the surface attains the negative charge at pH 7.0, therefore, repelling the negatively charged $[Fe(CN)_6]^{3-/4-}$ whilst attracting the positively $[Ru(NH_3)_6]^{2+/3+}$ redox probe.

The thickness of the monolayer was assessed by the ion barrier factor ($\Gamma_{ibf}$) value. The $\Gamma_{ibf}$ was studied in 0.010 M KOH solution. **Figure 4.3** (i) shows the gold oxidation (0.66 V) and the reduction (-0.08 V) peaks were observed at the bare AuE. After electrografting the gold to form AuE-IPA, the oxidation and reduction peak currents decreased as shown in **Fig. 4.3** (ii)**.** A further decrease in the redox peaks was observed in the CV for the AuE-IPA-anti-PSA-mAb|BSA shown in **Fig. 4.3** (iii). However, the decrease was much smaller compared to when the unsubstituted diazonium salts are used [32]. This suggested the formation of an ultrathin monolayer film due to IPA. The ion barrier factor was calculated using **Fig. 4.3** and **Eq. (4)** and was found to be 0.40. The $\Gamma_{ibf}$ increased from 0.40 on AuE-IPA to 0.60 on AuE-IPA-anti-PSA-mAb|BSA indicating the successful immobilization of the anti-PSA-mAb and the subsequent blocking with BSA of the AuE-IPA surface. The ion barrier factor in this study is far much less than a unit, suggesting the successful formation of an ultrathin monolayer film of IPA on the AuE surface.

$$\Gamma_{ibf} = 1 - \frac{Q_{monolayer}}{Q_{bare}} \qquad \textbf{(4.4)}$$

where $Q_{monolayer}$ and $Q_{bare}$ are the charges under the reduction peak of the AuE-IPA and AuE respectively.

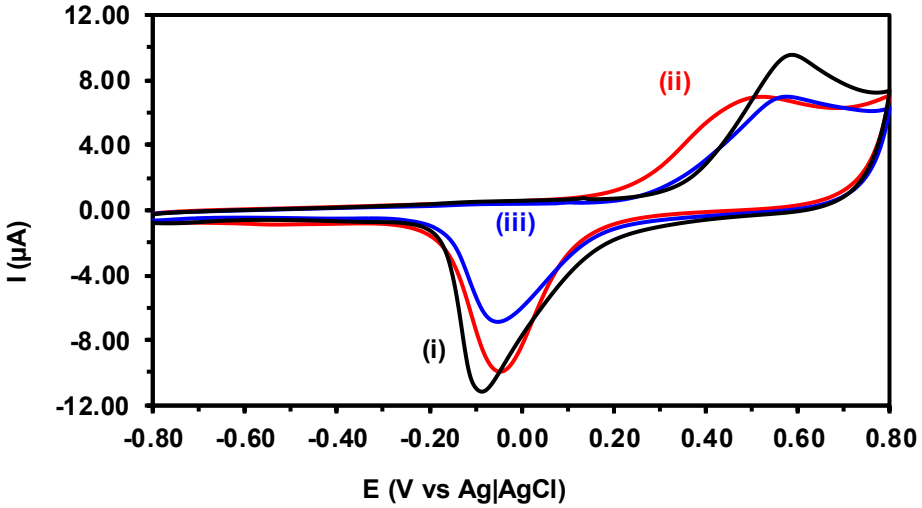


**Figure 4.3:** CVs of (i) AuE, (ii) AuE-IPA, and (iii) AuE-IPA-anti-PSA-mAb|BSA in 0.010 M KOH solution. Scan rate: 100 $mVs^{-1}$.

### 4.3.1.2 The effect of pH on the AuE-IPA and AuE-IPA-anti-PSA-mAb|BSA

The effect of pH on the AuE-IPA and AuE-IPA-anti-PSA-mAb|BSA was studied using the CV and EIS data obtained in 2.5 $mmol.L^{-1}$ of $[Fe(CN)_6]^{3-/4-}$ solution containing 0.10 mol $L^{-1}$ of KCl in PBS pH 4.0, 7.0 and 8.0. The EIS circuit model used in this study was a Randles circuit: $R_S(Q[R_{CT}Zw])$ where R is the resistance of the solution or electrolyte, $R_{CT}$ is the resistance of the charge-transfer of redox species moving through the film, Zw is the Warburg impedance, and Q is the capacitance, either double layer capacitance (Cdl) or the constant phase element (CPE) as reported in the literature [36]. The $R_S$ is connected in series to the parallel combination of CPE and $R_{ct,}$ which is in series to Zw.

**Figure 4.4** shows the CVs and their corresponding EIS Nyquist plots at pH 4.0, pH 7.0, and pH 8.0 of the (a) AuE, (b) AuE-IPA and (c) AuE-IPA-anti-PSA-mAb|BSA. **Figure 4.4(a)** shows that the AuE did not show any significant difference in both the CVs and the EIS at pH 4.0, pH 7.0, and pH 8.0. The gold electrode surface is inert and was not affected by the change of pH. However, at AuE-IPA, the CVs and Nyquist plots in **Fig. 4.4(b)** showed that the peak current and the electron transfer were higher at pH (pH 4.0) and this was due to the neutral (or protonated) carboxylic acid groups. At this pH, full protonation of the carboxylic acid groups on the AuE-IPA electrode took place as stated above. At pH 4.0, the ΔE for AuE was 75 mV

and the $R_{CT}$ was 0.16 kΩ. For AuE-IPA electrode at pH 4.0, the increase in ΔE to 90 mV and the $R_{CT}$ to 0.32 kΩ was observed. The small increase in both the ΔE and the $R_{CT}$ from the bare to that of the IPA modified signified the formation of an ultrathin monolayer film of IPA on the AuE electrode. The formed ultrathin monolayer film of IPA on gold electrode could not completely block the redox processes hence, the electrografted layer (AuE-IPA) retained the AuE electron transfer characteristics.

At pH 7.0 (ΔE = 103 mV, $R_{CT}$ = 0.51 kΩ) and pH 8.0 (ΔE = 176 mV, $R_{CT}$ = 1.08 kΩ), a significant increase in both the ΔE and $R_{CT}$ on the AuE-IPA surface was observed. This was so, because, the terminal carboxylic groups on the AuE-IPA electrode surface were deprotonated and became negatively charged ($-COO^-$). Therefore, causing the repulsive force between the isophthalic thin monolayer film and the negatively charged $[Fe(CN)_6]^{3-/4-}$ in solution. Thus, causing the increase in the blocking effect of the electron transfer as observed by the increase in the ΔE and $R_{CT}$. Since the pKa value of the grafted IPA monolayer is estimated at pKa = 3.69, the increase in pH to 8.0 increased the formation or deprotonation of the $-COO^-$ on the grafted electrode surface. It was interesting to note that the AuE-IPA-anti-PSA-mAb|BSA surface was also affected by changes in the pH. **Figure 4.4(c)**, shows that the immunosensor exhibited high electron transfer at pH 4.0 (ΔE = 80 mV, $R_{CT}$ = 0.30 kΩ). The AuE-anti-PSA-mAb|BSA surface at pH 4.0 resulted in the retention of the ΔE for AuE-IPA of 80 mV and $R_{CT}$ of 0.30 kΩ. The similar values were attributed to the pH being lower than the isoelectric point of both anti-PSA-mAb and BSA. Thus allowing electron transfer to occur and permeation of the redox probe ions. The electron transfer rate decreased further at pH 7.0 (ΔE = 136 mV, $R_{CT}$ = 0.70 kΩ) and pH 8.0 (ΔE = 180 mV, $R_{CT}$ = 0.80 kΩ). The decrease in the electron transfer was also noticed by the decrease of the peak current from pH 4.0 to pH 7.0 and pH 8.0. The pH responsiveness of the immunosensor was attributed to the presence of anti-PSA-mAb and BSA on an ultrathin IPA monolayer. It has been shown in the literature that proteins such as BSA and anti-PSA-mAb have a positive net charge in acidic pH and a negative charge at neutral and basic pH [35]. The positive charge of BSA at acidic pH enabled the attraction of the ferri/ferrocyanide negative charges, hence increasing the electron transfer. Whilst, the negative charge of BSA and anti-PSA-mAb at higher pH (pH 7.0 and pH 8.0) enabled the repulsion effect with the negatively charged ferricyanide redox probe, hence decreasing the electron elctron transfer.

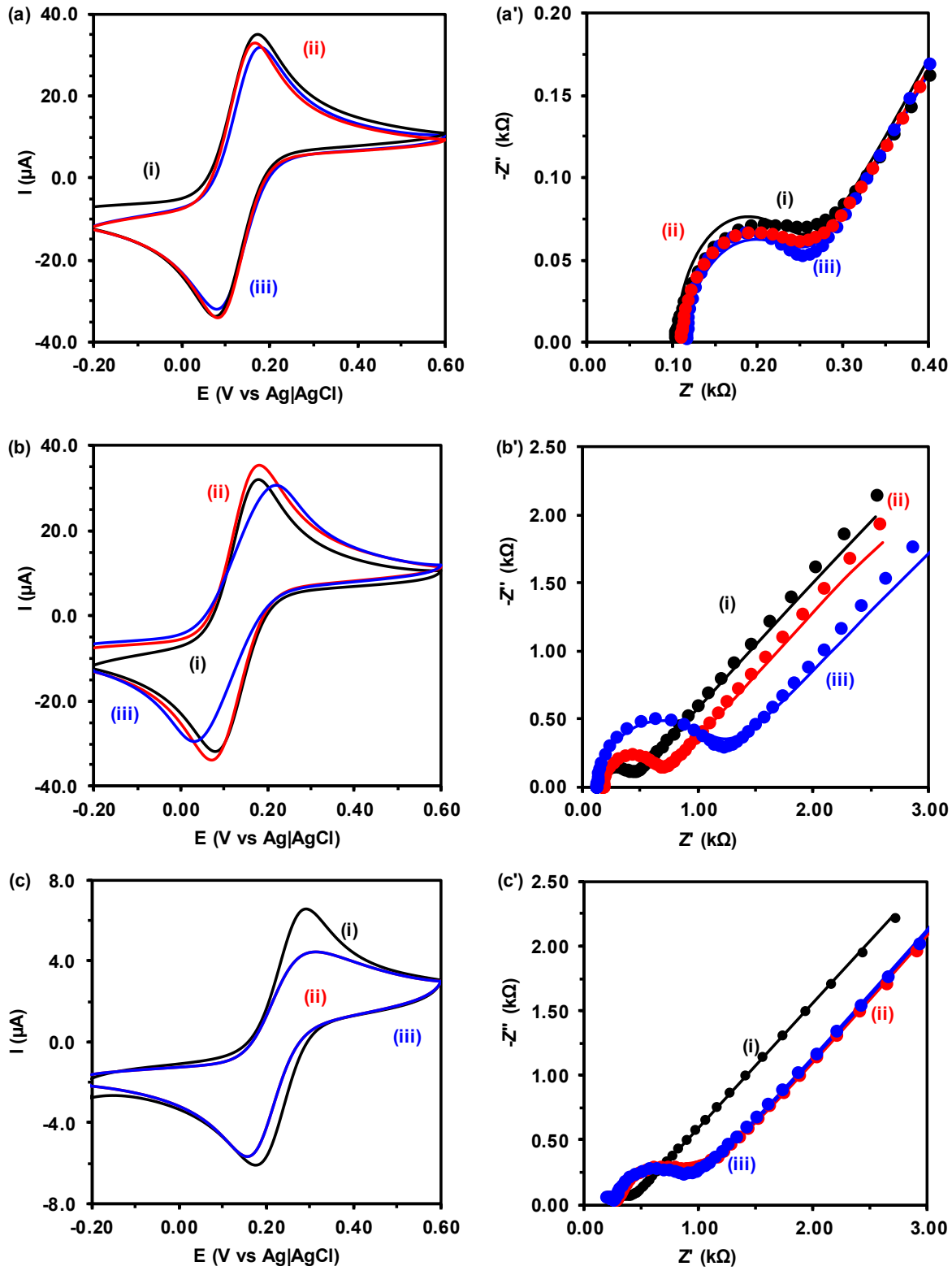


**Figure 4.4:** CVs and corresponding EIS of 2.5 mmol.L$^{-1}$ $[Fe(CN)_6]^{3-/4-}$ in 0.10 mol.L$^{-1}$ of KCl solution in (i) pH 4.0 (ii) pH 7.0 and (iii) pH 8.0 for (a) AuE and (b) AuE-IPA and (c) AuE-IPA-anti-PSA-mAb|BSA.

**Table 4.1** shows the summary of the effect of pH on the AuE, AuE-IPA and AuE-IPA-anti-PSA-mAb|BSA on the peak-to-peak separation (ΔE) and the charge-transfer resistance ($R_{CT}$) in 2.5 mmol.mL$^{-1}$ $[Fe(CN)_6]^{3-/4}$. The increase in both the ΔE and $R_{CT}$ due to the increase in pH was attributed to the increase in the repulsive forces between the negatively charged IPA thin monolayer film at higher pH and the negative redox probe $[Fe(CN)_6]^{3-/4}$ in solution. This phenomenon has also been observed elsewhere [37]. Furthermore, the capacitance decreased with an increase in pH due to the increasing repulsive forces and the distance in the double layer [33, 37].

The observed sharp responses of both the AuE-IPA and AuE-IPA-anti-PSA-mAb|BSA surfaces towards the changes in the pH of the electroactive probe indicated the successful electrografting of IPA and subsequent immobilization of anti-PSA-mAb and blocking of non-specific binding with BSA. The ultrathin monolayer film of IPA on gold electrode has been fully established by the persistent redox peaks of the gold electrode in both ferri/ferrocyanide, ruthenium hexamine redox reaction and gold oxidation in KOH solution. The formation of an ultrathin monolayer film of IPA on the gold electrode was important to facilitate the fabrication of an ultrasensitive label-free capacitive immunosensor for the detection of PSA.

**Table 4.1:** Parameters acquired from the CVs and EIS in 2.5 mmol.L$^{-1}$ $[Fe(CN)_6]^{3-/4-}$ containing 0.10 mol.L$^{-1}$ KCl at pH 4.0, pH 7.0, and pH 8.0.

| Electrode | ΔE (mV.cm$^{-2}$) | | | $R_{ct}$ (kΩ.cm$^{-2}$) | | | C (μF.cm$^{-2}$) | | |
|---|---|---|---|---|---|---|---|---|---|
| | pH 4.0 | pH 7.0 | pH 8.0 | pH 4.0 | pH 7.0 | pH 8.0 | pH 4.0 | pH 7.0 | pH 8.0 |
| AuE | 75 | 83 | 91 | 0.16 | 0.21 | 0.32 | 3.14 | 2.76 | 2.13 |
| AuE-IPA | 90 | 103 | 176 | 0.32 | 0.51 | 1.08 | 2.97 | 2.26 | 1.49 |
| AuE-IPA-anti-PSA-mApBSA | 80 | 136 | 180 | 0.30 | 0.70 | 0.80 | 4.50 | 2.89 | 2.78 |

### 4.3.1.3 XPS analysis of the AuE-IPA and AuE-IPA-anti-PSA-mAb surfaces

The XPS analysis was used to investigate the presence of the elements due to the electrografting of IPA on the bare gold electrode form AuE-IPA and the subsequent immobilization of the anti-PSA monoclonal antibody to yield AuE-IPA-anti-PSA-mAb. The characterization of the bare (AuE) gold electrode was done as reported previously [32]. **Figure 4.5** shows the survey spectra of (i) AuE-IPA and (ii) AuE-IPA-anti-PSA-mAb which indicated the presence of the peaks due to gold (Au 4f, Au 4p, and Au 4d), carbon (C 1s), nitrogen (N 1s), and Oxygen (O 1s). The presence of the C 1s (284.9 eV, 77.7%) and O 1s (531.9 eV, 16.7%) on the Au-IPA surface confirmed the successful electrografting of the IPA thin monolayer film on the gold surface. The unexpected N 1s (399.9 eV, 5.6%) peak on the AuE-IPA surface might be due to the presence of the adsorbed nitrogen used to dry the AuE-IPA after the electrografting process. The persistence presence of the Au 4f, Au 4p and Au 4d peaks on the AuE-IPA shown in **Fig. 4.5(i)** indicated that the ultrathin IPA monolayer film formed. The XPS survey analysis of AuE-IPA-anti-PSA-mAb in **Fig. 4.5(ii)** showed that the peaks due to the underlying gold surface disappeared. This was attributed to the anti-PSA-mAb layer immobilized onto the thin monolayer film of IPA. Furthermore, the percentage atomic composition (at%) of the peak due to O 1s was observed to increase from the AuE-IPA (16.7%) to that of AuE-IPA-anti-PSA-mAb (44.3%). The increase in O 1s intensity at Au-IPA-anti-PSA-mAb was attributed to the immobilization of the antibody containing numerous amide and carbonyl groups. Henceforth, confirming the successful formation of the immunosensing surface, AuE-IPA-anti-PSA-mAb.

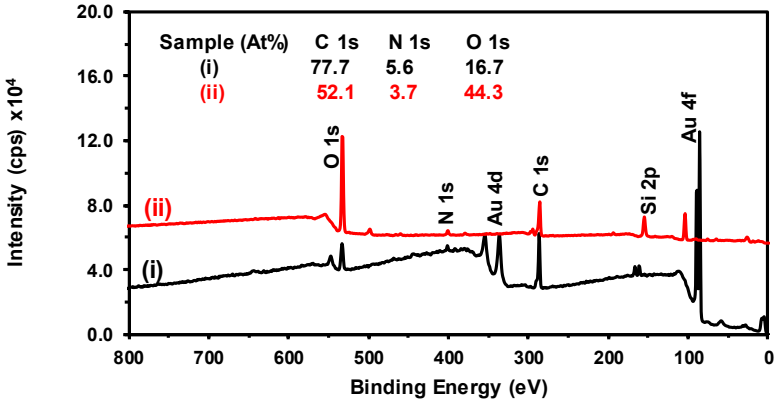


**Figure 4.5:** XPS survey spectra of (i) AuE-IPA and (ii) AuE-IPA-anti-PSA-mAb.

**Figure 4.6** shows the high resolution core-level spectra for (a) AuE-IPA and (b) AuE-IPA-anti-PSA-mAb surface analysis of C 1s (left column), O 1s (middle column), and N 1s (right column). The deconvoluted spectra of C 1s in **Fig. 4.6**(a) showed five components with an intense peak at 284.9 eV due to C=C and C-H (64.8%). The other three components were observed at 287.0 eV (C-OH, 18.7%), 289.7 eV (O-C-O, 10.1%), and 288.8 eV (O=C-OH, 4.7%) all due to the carboxylic acid of the IPA moiety electrografted [28] on the gold surface. The electrografting of IPA on the gold surface was further confirmed by the appearance of the fifth component at 284.4 eV (C-Au) which was due to the carbide bond [32]. The Au-C was observed due to the thin monolayer film of IPA. Deconvolution of the C 1s for the AuE-IPA-anti-PSA-mAb in **Fig. 4.6**(**b**) showed four components. The component due to C-Au (284.4 eV) disappeared as a result of covalent immobilized anti-PSA-mAb masking the AuE-IPA surface. The components due to C=C and C-C were observed at 284.9 eV. There was an increase in the atomic percentage observed on the component at 286.3 eV (C-O and C-N) from 18.7% to 23.3%, and the component at 288.9 eV (C=O, 6.4%) which could be attributed to the amino acid groups on the immobilized anti-PSA monoclonal antibody. The decrease in atomic percentage for the component at 288.0 eV (O=C-O, 4.6%) could be attributed to the formation of the amide bond that introduces the C-N bond substituting the C-O on the IPA monolayer.

The O 1s high resolution core-level analysis of the AuE-IPA thin monolayer film was deconvoluted and three components at 531.5 eV (O-H, 15.4%), 532.9 eV (C=O, 65.7%), and 534.3 eV (C-O, 19.0%) were shown in **Fig. 4.5(a')**. The components accounting for the presence of O-H, and C-O binding energies were expected due to the electrografting of the IPA monolayer. After immobilization of the anti-PSA monoclonal antibody on the AuE-IPA surface, the O 1s high resolution spectra in **Fig. 4.5(b')** showed some distinct changes but deconvoluted to the same number of components. The component due to O-H and C=O (72.4%), C-O (19.2%), and O=C (8.5%) were observed to increase in intensity by 10 folds indicating an increased amount of carbonyl (C=O) groups due to the peptide bonds on the anti-PSA monoclonal antibodies.

The N 1s of the AuE-IPA in **Fig. 4.5(a")** deconvoluted to one component at 401.0 eV due to the presence of the $N_2$ as a result of the adsorbed nitrogen gas on the surface. Whilst, on the AuE-IPA-anti-PSA-mAb surface, three components of the N 1s were observed as shown in **Fig. 4.5(b").** The component due to N-H (398.1 eV) and $N^+$ (402.6 eV) accounted for the presence of the peptide bonds from the anti-PSA antibodies present on the AuE-IPA-anti-PSA-mAb surface. The changes in the N 1s chemical environment from that of the AuE-IPA (N-C)

to the AuE-IPA-anti-PSA-mAb (N-H, N-C, and $N^+$) further confirmed the successful immobilization of the anti-PSA antibody on the AuE-IPA via the EDC/NHS chemistry.

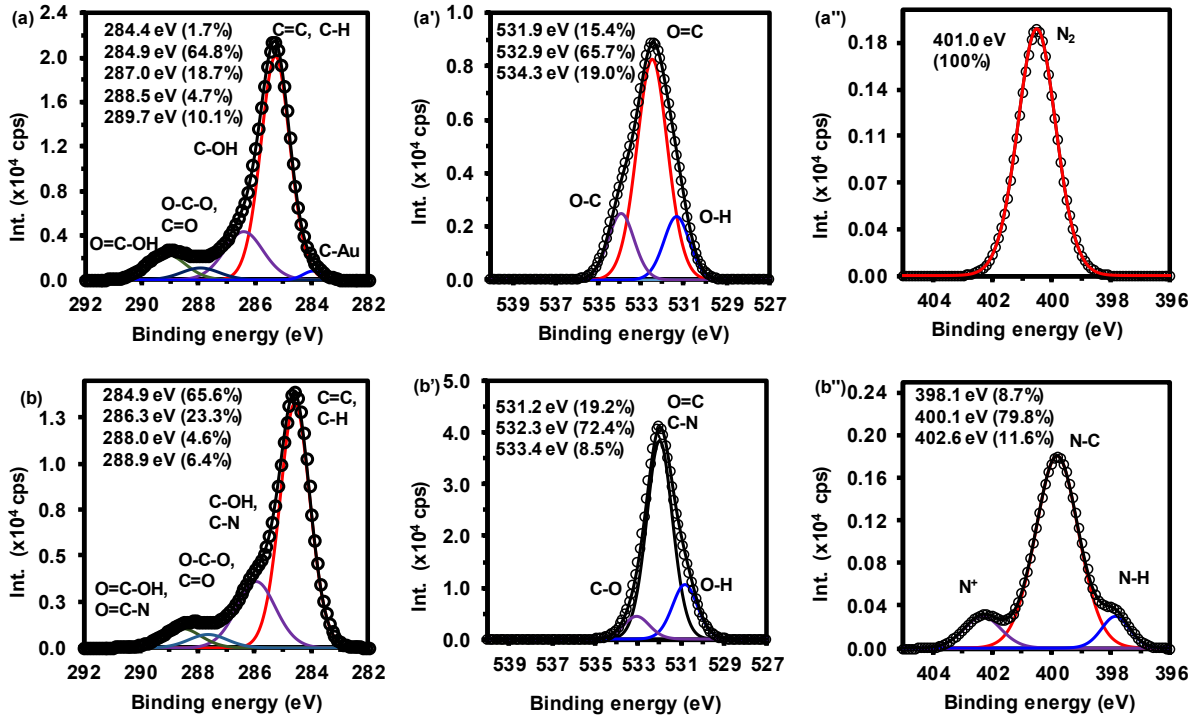


**Figure 4.6:** High resolution core-level spectra of C 1s (left column), O 1s (middle column and N 1s (right column) for (a) AuE-IPA and (b) AuE-IPA-anti-PSA-mAb

### 4.3.2 Principle of capacitive detection of PSA and optimization of immunoassay fabrication

The AuE-IPA-anti-PSA-mAb|BSA immunosensor was used for the capacitive detection of PSA in PBS (pH 7.4) via non-Faradaic EIS. The detection mechanism was based on the capture of PSA by the immobilized anti-PSA-mAb on the electrode surface. The changes in capacitance of the sensing surface after exposure to PSA spiked PBS were measured. The EIS data acquired during the non-Faradaic impedimetric sensing of PSA was processed in three different analysis techniques. This was done to assess the robustness of the immunosensor for the label-free impedimetric detection of PSA.

The following variables were optimized for the fabrication of the AuE-IPA-anti-PSA-mAb|BSA sensing platform towards impedimetric detection of PSA: (i) the number of cyclic voltammograms (CVs) for electrografting of IPA onto the Au electrode, (ii) amount of anti-

PSA-mAb immobilized, and (iii) incubation time of the AuE-IPA-anti-PSA-mAb|BSA sensing platform in PBS (pH 7.4) containing PSA. These variables were assessed using the non-Faradaic electrochemical capacitance depicted as the diameter of the capacitance Nyquist plot changes by incubating in PBS ($C_{PBS}$) and after incubating in PBS containing 0.10 ng.mL$^{-1}$ of PSA ($C_{PSA}$). **Figure 4.7** shows the optimization of AuE-IPA-anti-PSA-mAb|BSA sensing platform at different variables, (a) shows the effect of the number of scans for electrografting of IPA, (b) the amount of anti-PSA-mAb immobilized, and (c) incubation time. In **Fig. 4.7(a)**, the number of CVs for electrografting of IPA onto the AuE electrode was varied between 4 to 24 scans. The recorded scans were at every fourth interval. It was observed that the $Q_{PSA}$ decreased with an increase in the scan number until the 20$^{th}$ and 24$^{th}$ scans which showed the same semicircle. The decrease in capacitance semicircle between the 4$^{th}$ and 20$^{th}$ scans was attributed to the increase of the immobilized anti-PSA-mAb due to the increase of the amount of IPA molecules grafted on the pinholes at the AuE surface. The 20$^{th}$ scan was chosen as an optimum as no further changes in capacitance signal was observed.

The percentage relative response (RR%) was calculated as shown in **Eq. (4.7)** used to monitor the effect of the amount of anti-PSA-mAb immobilized. In **Fig. 4.7(b),** it was observed that the change in RR% value increased with an increasing concentration of the immobilized anti-PSA-mAb up to 20.0 μg.mL$^{-1}$ and reached a plateau afterwards. The plateau of the RR% observed at 20.0 μg.mL$^{-1}$ could be attributed to the saturation of anti-PSA-mAb and steric hindrance preventing the further capturing of the PSA. Therefore, 20.0 μg.mL$^{-1}$ of anti-PSA antibody was the optimal for the fabrication of the AuE-IPA-anti-PSA-mAb|BSA sensing for the impedimetric detection of PSA.

The effect of the incubation time in PBS containing 0.10 ng.mL$^{-1}$ of PSA on the AuE-IPA-anti-PSA-mAb|BSA sensing platform towards the impedimetric detection of PSA was also investigated. The measure of RR% was plotted against the incubation time between 0 to 25 min. The relative response signal increased with the longer incubation time and reached its maximum value at 15 minutes. No further increase in the signal was observed after 15 min of incubation time. Therefore, 15 minutes was used as the optimum incubation time for the AuE-IPA-anti-PSA-mAb|BSA sensing platform towards impedimetric detection of PSA.

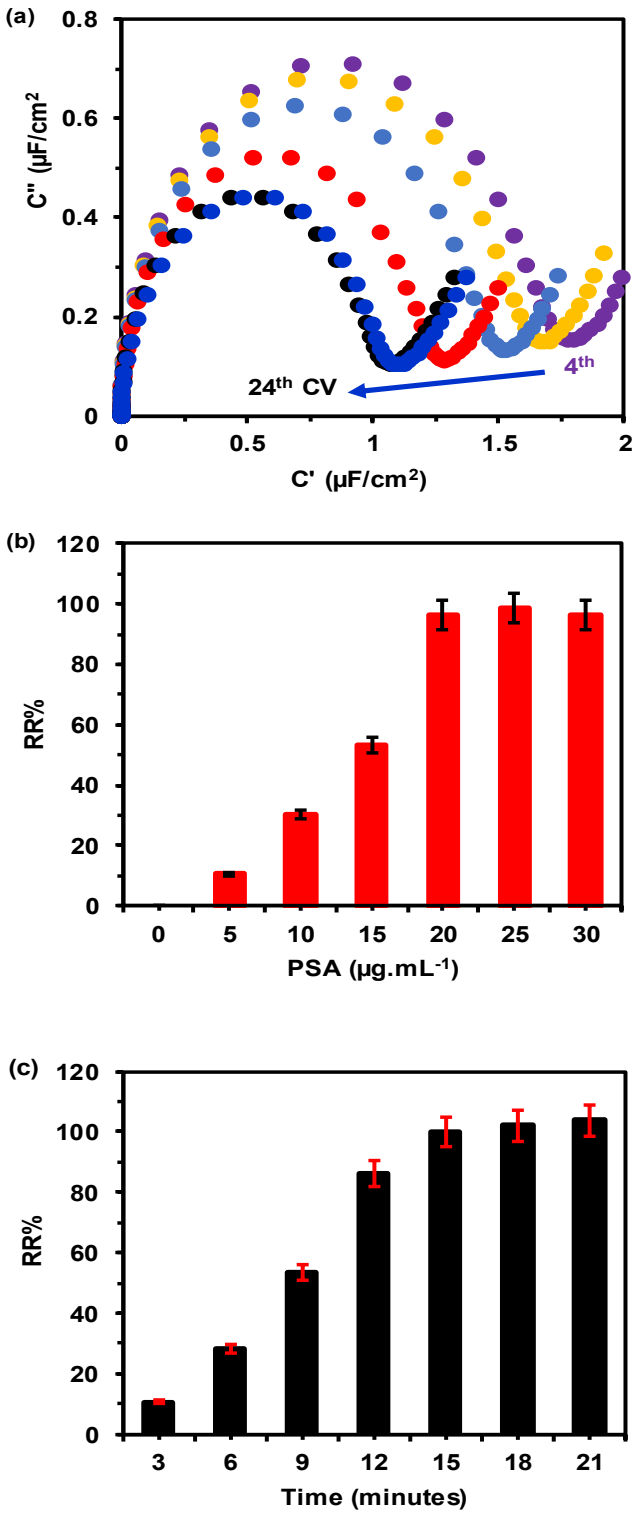


**Figure 4.7:** Optimisation for the fabrication of the AuE-IPA-anti-PSA-mAb|BSA sensing platform towards capacitive detection of PSA: (a) effect of the number of scans for electrografting of IPA, (b) amount of anti-PSA-mAb immobilized, and (c) the incubation time PBS containing 0.10 ng.mL$^{-1}$ of PSA.

### 4.3.3 Non-Faradaic impedimetric detection of PSA

The non-Faradaic impedimetric detection of PSA was done using three data analysis methods. The first method comprised of conversion of the non-Faradaic impedimetric detection data into the capacitive Nyquist plots (-C" Vs C') to obtain the non-Faradaic capacitance as the diameter of the semicircle. The second method involved the conversion of the non-Faradaic impedimetric detection data into the complex capacitance (C*). The third method involved the use of Randles circuit ($R_SC$) fitting for the non-Faradaic impedimetric detection of PSA.

#### 4.3.3.1 Capacitance Nyquist plots for detection of PSA

The non-Faradaic EIS data from the measurement shown in **Fig. 4.8** was converted to the total capacitance plane using Matlab and **Eq. (4.5):**

$$C = \frac{1}{j\omega Z} \qquad \textbf{(4.5)}$$

where C is the total capacitance, Z is the total impedance, $j^2 = -1$ with $\omega = 2\,\pi\,f$ in which *f is* the frequency in Hz. Total complex capacitance can be expressed in terms of the real (C') and the imaginary (C") capacitance as shown in **Eq. (4.6).** The capacitance Nyquist plot of C' versus C" was obtained.

$$C = C' + jC'' \qquad \textbf{(4.6)}$$

**Fig. 4.8(a)** shows the EIS Nyquist plot of the imaginary (-Z") part versus the real (Z') part impedance. The plot shows that the impedance data from the blank to the data with varying concentrations of PSA overlaps. The EIS data was transformed to the total capacitance and the plot of imaginary (C") versus real (C') capacitance is shown in **Fig. 4.8(b)**. The drifting of the semicircle was observed from the blank (without PSA) to the data acquired after exposing the immunosensor to varying concentrations of PSA. The diameter of the semicircle of the blank was wider than that of PBS containing PSA. The semicircle diameter decreased showing the decrease in the total capacitance in the presence of PSA. The decrease was attributed to the binding of PSA to the anti-PSA-mAb on the electrode forming a compact antibody film after binding the antigen. From the Nyquist plots of capacitance in **Fig. 4.8 (b)**, the non-Faradaic

capacitance ($C_{nFC}$) was determined according to the literature [27, 38] and was then used to obtain the relative response percentage (RR%) following **Eq. (4.7):**

$$\boldsymbol{RR\%} = \left[\frac{\left(\frac{1}{C_{PSA}} - \frac{1}{C_{PBS}}\right)}{\frac{1}{C_{PBS}}}\right] \boldsymbol{x\ 100} \qquad \textbf{(4.7)}$$

where, $C_{PSA}$ is the non-Faradaic capacitance after electrode incubation in PBS containing PSA and $C_{PBS}$ is the capacitance measured in the blank PBS**.** The RR% values were poted versus the logarithmic concentration of PSA to generate the analytical curve for the label-free capacitive detection of PSA, as shown in **Fig. 4.8 (c)**. The RR% in **Fig. 4.8 (c)** shows a linear curve against PSA concentration ranging from 10 fg.mL$^{-1}$ and 0.10 mg.mL$^{-1}$ and the limit of detection (LOD) was calculated to be 2.3 fg.mL$^{-1}$ and LOQ was calculated to be 7.6 fg.mL$^{-1}$ based on literature reported method of calculating the LOD and LOQ [32,41].

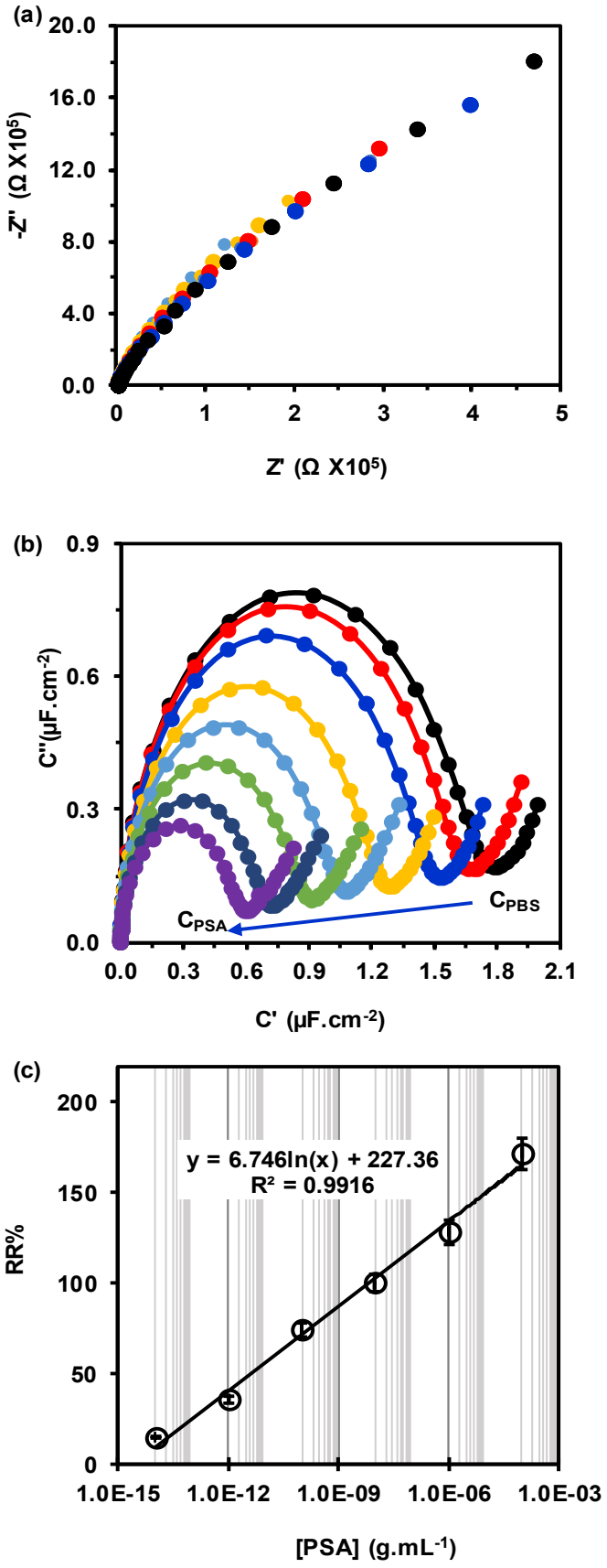


**Figure 4.8:** (a) EIS Nyquist plots (-Z" vs Z'), (b) complex capacitance Nyquist plots (C" vs C'), and (c) calibration curve for [PSA] from 0.10 fg.mL$^{-1}$ to 0.10 mg.mL$^{-1}$.

#### 4.3.3.2 Complex capacitance for detection of PSA

The complex capacitance (C*) was used to monitor the analytical performance of the developed sensor and was computed by converting the imaginary impedance data (-Z″) to the C* by using **Eq. (4.8).** as reported in the literature [39,40]:

$$C^* = \frac{-1}{\omega Z''} \qquad \textbf{(4.8)}$$

where C* is the capacitance calculated from the imaginary impedance, -Z", $\omega$ is the radian frequency which is expressed as $2\pi f$ in which $f$ is the frequency in Hz. Hence **Eq. 4.8**, is rewritten as **Eq. (4.9):**

$$C^* = \frac{-1}{2\pi f Z''} \qquad \textbf{(4.9)}$$

**Figure 4.9(a)** shows the plot of capacitance (C*) versus log frequency (log $f$) and the maximum corresponding capacitance effect was at 100 Hz. The C* values at the frequency of 100 Hz were used to generate the calibration curve shown in **Fig. 4.9(b)**. **Figure 4.8(b)** shows that the capacitance decreases linearly with an increase in the PSA concentration. This trend in capacitance can be attributed to the binding of the PSA antigen to the immobilized anti-PSA-mAb on the electrode surface.

The phenomenon observed above agrees with the theory in literature [18, 22] that capacitance changes with the changes in the dielectric properties of the electrode surface shown in **Eq. (4.10).**

$$C = \varepsilon_r \varepsilon_0 \frac{A}{d} \qquad \textbf{(4.10)}$$

Where $\varepsilon_r$ is the relative dielectric constant, $\varepsilon_0$ is the relative solution permittitivity, $A$ is the area of an electrode surface and $d$ is the thickness of an insulator. Therefore, the binding of the PSA antigen to the immobilized anti-PSA antibody resulted in changes in the dielectric effect, which later caused a decrease in capacitance. At high concentrations of PSA, the higher the increase in binding and thickness resulted in the decrease in capacitance, as observed in both **Fig. 4.9(a)**.

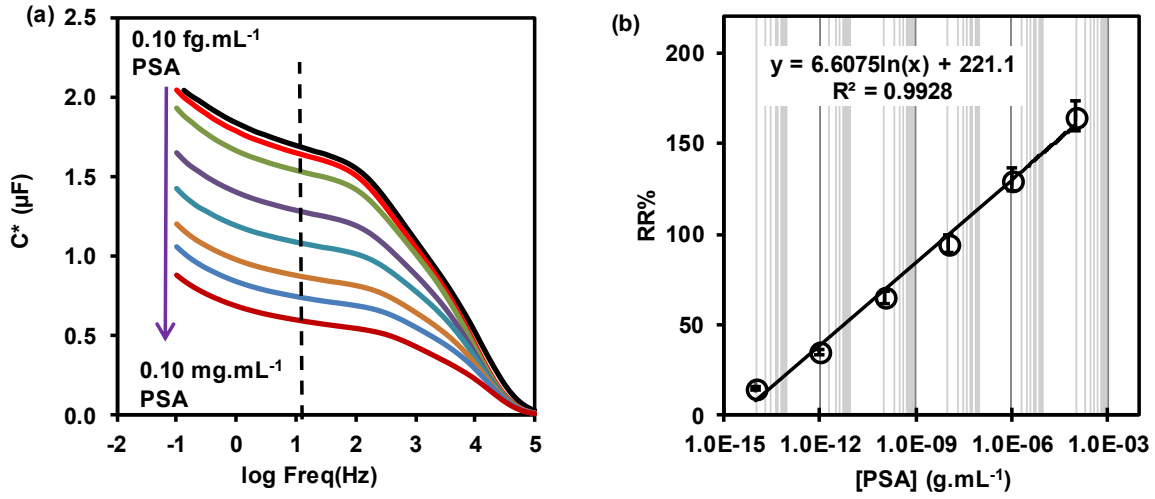


**Figure 4.9:** (a) Plot of complex capacitance versus log frequency and (b) calibration curve at varying [PSA] ranging from 0.10 fg.mL$^{-1}$ to 0.10 mg.mL$^{-1}$

The plot of RR% against the [PSA] generated the calibration curve for the label-free capacitive detection of PSA as described in **Eq. (4.7)**. The RR% in **Fig. 4.9(b)** shows a linear curve against [PSA] concentration ranging from 10.0 fg.mL$^{-1}$ to 0.10 mg.mL$^{-1}$. The LOD was calculated to be 7.6 fg.mL$^{-1}$ and the LOQ was 25.1 fg.mL$^{-1}$.

### 4.3.3.3 Impedimetric detection of PSA using the Randles circuit ($R_SC$) fitting

Randles circuit with solution resistance ($R_S$) and capacitance (C) in series ($R_SC$) was used in this study to analyze the application of impedimetric detection of PSA by monitoring the changes in capacitance as reported [18]. Using this approach, it was observed that the capacitance in the modeled Randles circuit decreased with an increase in the PSA concentrations, as shown in **Fig. 4.10(a)**. The decrease in the capacitance using this approach was observed to be similar with the methods used above. This suggests the success of the applicability of the fabricated immunosensor and also the achievement of the aims of this work. The changes in capacitance were linearly related when the plot of RR% vs [PSA] (g.mL$^{-1}$) was used as shown in **Fig. 4.10 (b)**. LOD was calculated to be 3.3 fg.mL$^{-1}$ and the LOQ was calculated to be 11.0 fg.mL$^{-1}$ based on literature [32,41].

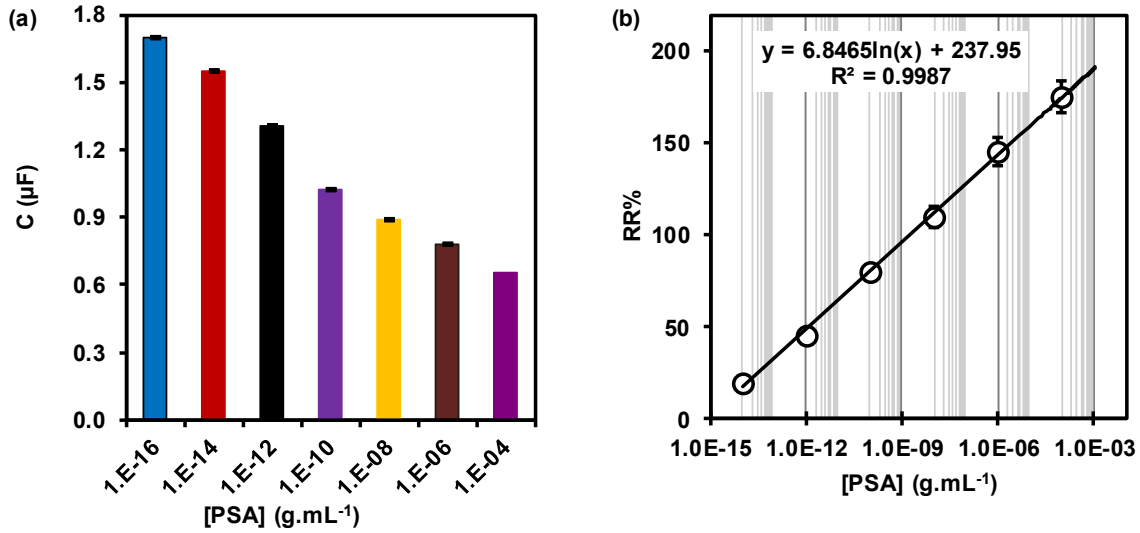


**Figure 4.10:** (a) Bar graph of C (µF) vs [PSA] and the corresponding calibration curve of RR% vs [PSA] for [PSA] ranging from 10.0 fg.mL$^{-1}$ to 0.10 mg.mL$^{-1}$.

The analytical behavior of this study was compared with the other electrochemical biosensors for the detection of PSA as shown in **Table 4.2.** The Table **4.2** shows that the immunosensor developed here has achieved both the low LOD in femtograms per milliliter of PSA and a very wide concentration range. In addition, the use of electrografting of IPA as a thin monolayer template for the immobilization of anti-PSA-mAb proved to be more simple, reproducible, and stable with a high binding affinity for the detection of PSA. The fabricated electrochemical immunosensor for the detection of PSA was compared with immunosensor fabricated with molecular imprinting [16], polymer imprinting [42], and mixed self-assembly monolayers [43]. These methods present a wide range of advantages, however, they suffer from slow mass transfer kinetic [44], low-affinity binding sites [45], and instability [22] in the case of the SAMs. Henceforth, making the immunosensor developed in this work much more desirable.

**Table 4.2:** A comparison of different electrochemical biosensors for the detection of PSA

| Method of modification | Method of PSA analysis | Range of detection | LOD | Refs |
|---|---|---|---|---|
| Molecular imprinting | Imprinted capacitive sensing | 10 $fg.mL^{-1}$ to 100 $ng.mL^{-1}$ | 80.0 $fg.mL^{-1}$ 600.0 $fg.mL^{-1}$ | [16] |
| Polymer imprinting | Double layer capacitance | 1 $ng.mL^{-1}$ to 100 $ng.mL^{-1}$ | 3 $ng.mL^{-1}$ | [42] |
| Self-assembly monolayer | Surface plasmon response | 70 $pg.mL^{-1}$ to 100 $ng.mL^{-1}$ | 1 $ng.mL^{-1}$ | [43] |
| Diazonium salt Electrografting | Total capacitance from total impedance | 10.0 $fg.mL^{-1}$ to 0.10 $mg.mL^{-1}$ | 2.30 $fg.mL^{-1}$. | TW |
| Diazonium salt Electrografting | Capacitance from imaginary impedance | 10.0 $fg.mL^{-1}$ to 0.10 $mg.mL^{-1}$ | 7.6 $fg.mL^{-1}$ | TW |
| Diazonium salt Electrografting | Randles circuit fitting ($R_SC$) | 10.0 $fg.mL^{-1}$ to 0.10 $mg.mL^{-1}$ | 3.3 $fg.mL^{-1}$ | TW |

TW = This work

## 4.4 Conclusions

In this chapter, a thin monolayer film of IPA was achieved via electrografting of 5-DIPA on the gold electrode surface. The thin monolayer film was thoroughly studied using CV and EIS and these techniques confirmed that the gold electrode contained an immobilized isophthalic acid monolayer. The AuE-IPA could respond to pH changes of the solution due to the presence of pH-sensitive COOH functional groups. The AuE-IPA thin monolayer film was later used for the covalent attachment of anti-PSA-mAb for a capacitive label-free detection of PSA. Capacitive PSA detection was performed with standard PSA solutions in the concentration range of 10.0 $fg.mL^{-1}$ and 0.10 mg. $mL^{-1}$ using EIS for data acquisition. The analytical performance of the developed sensor was validated using Nyquist plots of capacitance generated from the complex impedance data, complex capacitance calculated from the imaginary part of the impedance, and capacitance as the double layer capacitance from the circuit fitting ($R_SC$) all versus [PSA]. All the three data analysis techniques used showed excellent LODs which were found to be 2.3 $fg.mL^{-1}$, 7.6 $fg.mL^{-1}$, and 3.3 $fg.mL^{-1}$ for the Nyquist plots of capacitance, complex capacitance and capacitance from the circuit fitting ($R_SC$) respectively.

## 4.5 References


[1] H. Sung, J. Ferlay, R.L. Siegel, M. Laversanne, I. Soerjomataram, A. Jemal, F. Bray, Global Cancer Statistics 2020: GLOBOCAN Estimates of Incidence and Mortality Worldwide for 36 Cancers in 185 Countries, CA. Cancer J. Clin. 71 (2021) 209–249.

[2] J.M. Mattsson, S. Ravela, C. Hekim, M. Jonsson, J. Malm, A. Närvänen, U.H. Stenman, H. Koistinen, Proteolytic activity of prostate-specific antigen (PSA) towards protein substrates and effect of peptides stimulating PSA activity, PLoS One. 9 (2014) 1–12.

[3] I.E. Tothill, Biosensors for cancer markers diagnosis, Semin. Cell Dev. Biol. 20 (2009) 55–62.

[4] H. Qi, M. Li, M. Dong, S. Ruan, Q. Gao, C. Zhang, Electrogenerated chemiluminescence peptide-based biosensor for the determination of prostate-specific antigen-based on target-induced cleavage of peptide, Anal. Chem. 86 (2014) 1372–1379.

[5] J. Meehan, M. Gray, C. Mart, C. Kay, D. Mclaren, A.K. Turnbull, Tissue- and Liquid-Based Biomarkers in Prostate Cancer Precision Medicine, J. Pers. Med. 11 (2021) 1–37.

[6] B. Acevedo, Y. Perera, M. Ruiz, G. Rojas, J. Benítez, M. Ayala, J. Gavilondo, Development and validation of a quantitative ELISA for the measurement of PSA concentration, Clin. Chim. Acta. 317 (2002) 55–63.

[7] A.S. Abu-Bakr El-Bayoumy, A.T. Hessien Keshta, K.M. Sallam, N.H. Ebeid, H.M. Elsheikh, B.E.S. Bayoumy, Extraction, purification of prostate-specific antigen (PSA), and establishment of radioimmunoassay system as a diagnostic tool for prostate disorders, J. Immunoass. Immunochem. 39 (2018) 12–29.

[8] E.W. Klee, O.P. Bondar, M.K. Goodmanson, S.A. Trushin, E.J. Bergstralh, R.J. Singh, N.L. Anderson, G.G. Klee, Serum concentrations of prostate-specific antigen measured using immune extraction, trypsin digestion, and tandem mass spectrometry quantification of LSEPAELTDAVK peptide, Arch. Pathol. Lab. Med. 138 (2014) 1381–1386

[9] M. Kawatani, K. Yamamoto, D. Yamada, M. Kamiya, J. Miyakawa, Y. Miyama, R. Kojima, T. Morikawa, H. Kume, Y. Urano, Fluorescence Detection of Prostate Cancer

by an Activatable Fluorescence Probe for PSMA Carboxypeptidase Activity, J. Am. Chem. Soc. 141 (2019) 10409–10416.

[10] S. Gutkin, O. Green, G. Raviv, D. Shabat, O. Portnoy, Powerful Chemiluminescence Probe for Rapid Detection of Prostate-Specific Antigen Proteolytic Activity: Forensic Identification of Human Semen, Bioconjug. Chem. 31 (2020) 2488–2493.

[11] M. Kim, K. Kim, J.H. Lee, A cost-effective and rapid aptasensor with chemiluminescence detection for the early diagnosis of prostate cancer, Microchem. J. 155 (2020) 104763 (1-8).

[12] X.P. Liu, N. Chang, J.S. Chen, C.J. Mao, B.K. Jin, Ultrasensitive photoelectrochemical immunosensor based on a g-$C_3N_4$/$SnS_2$ nanocomposite for prostate-specific antigen detection, Microchem. J. 168 (2021) 106337 (1-10).

[13] Y. Zhang, Y. Liu, R. Li, M. Saddam Khan, P. Gao, Y. Zhang, Q. Wei, Visible-light driven Photoelectrochemical Immunosensor Based on $SnS_2$@mpg-$C_3N_4$ for Detection of Prostate Specific Antigen, Sci. Rep. 7 (2017) 1–8.

[14] W. Jung, J. Han, J.W. Choi, C.H. Ahn, Point-of-care testing (POCT) diagnostic systems using microfluidic lab-on-a-chip technologies, Microelectron. Eng. 132 (2014) 46–57.

[15] G. Ertürk, B. Mattiasson, Capacitive biosensors, and molecularly imprinted electrodes, Sensors (Switzerland). 17 (2017) 1–21.

[16] G. Ertürk, M. Hedström, M.A. Tümer, A. Denizli, B. Mattiasson, Real-time prostate-specific antigen detection with prostate-specific antigen imprinted capacitive biosensors, Anal. Chim. Acta. 891 (2015) 120–129.

[17] M. Prodromidis, Impedimetric Biosensors and Immunosensors, Proc. 2nd Int. Semin. Anal. Sci. 8 (2007) 69–71.

[18] C. Berggren, G. Johansson, Capacitance Measurements of Antibody-Antigen Interactions in a Flow System, Anal. Chem. 69 (1997) 3651–3657.

[19] A. Qureshi, Y. Gurbuz, J.H. Niazi, Label-free capacitance-based aptasensor platform for the detection of HER2/ErbB2 cancer biomarker in serum, Sensors Actuators, B Chem. 220 (2015) 1145–1151.

[20] V.M. Mirsky, M. Riepl, O.S. Wolfbeis, Capacitive monitoring of protein immobilization and antigen-antibody reactions on monomolecular alkylthiol films on gold electrodes, Biosens. Bioelectron. 12 (1997) 977–989.

[21] Y. Wei, L. Luo, Y. Ding, X. Si, Y. Ning, Highly sensitive determination of methotrexate at poly (l-lysine) modified electrode in the presence of sodium dodecylbenzene sulfonate, Bioelectrochemistry. 98 (2014) 70–75.

[22] C. Berggren, B. Bjarnason, G. Johansson, Capacitive biosensors, Electroanal. 13 (2001) 173–180.

[23] D. Bélanger, J. Pinson, Electrografting: A powerful method for surface modification, Chem. Soc. Rev. 40 (2011) 3995–4048.

[24] M. Ceccato, A. Bousquet, M. Hinge, S.U. Pedersen, K. Daasbjerg, Using a mediating effect in the electroreduction of aryldiazonium salts to prepare conducting organic films of high thickness, Chem. Mater. 23 (2011) 1551–1557.

[25] D. Hetemi, V. Noël, J. Pinson, Grafting of diazonium salts on surfaces: Application to biosensors, Biosensors. 10 (2020) 4-35.

[26] Q.-Z. Xie, M.-W. Lin, W.-E. Hsu, C.-T. Lin, Review—Advancements of Nanoscale Structures and Materials in Impedimetric Biosensing Technologies, ECS J. Solid State Sci. Technol. 9 (2020) 115027 (1-13).

[27] B.L. Garrote, A. Santos, P.R. Bueno, Label-free capacitive assaying of biomarkers for molecular diagnostics, Nat. Protoc. 15 (2020) 3879–3893.

[28] Z. Üstündağ, M.O. Çağlayan, R. Güzel, E. Pişkin, A.O. Solak, A novel surface plasmon resonance enhanced total internal reflection ellipsometric application: electrochemically grafted isophthalic acid nanofilm on gold surface, Analyst, 136 (2011) 1464-1471.

[29] I. López, S. Dabos-Seignon, T. Breton, Use of Selective Redox Cross-Inhibitors for the Control of Organic Layer Formation Obtained via Diazonium Salt Reduction, Langmuir 35 (2019) 11048–11055.

[30] C. Combellas, F. Kanoufi, J. Pinson, F.I. Podvorica, Sterically hindered diazonium salts for the grafting of a monolayer on metals, J. Am. Chem. Soc. 130 (2008) 8576–8577.

[31] J. Greenwood, T.H. Phan, Y. Fujita, Z. Li, O. Ivasenko, W. Vanderlinden, H. Van Gorp, W. Frederickx, G. Lu, K. Tahara, Y. Tobe, H. Uji-I, S.F.L. Mertens, S. De Feyter, Covalent modification of graphene and graphite using diazonium chemistry: Tunable grafting and nanomanipulation, ACS Nano. 9 (2015) 5520–5535.

[32] D. Mwanza, S. Mvango, S. Khene, T. Nyokong, P. Mashazi, Exploiting Click Chemistry for the Covalent Immobilization of Tetra (4-Propargyloxyphenoxy) Metallophthalocyanines onto Phenylazide-Grafted Gold Surfaces, Electrochim. Acta. 254 (2017) 89-100.

[33] J. Liu, L. Cheng, B. Liu, S. Dong, Covalent modification of a glassy carbon surface by 4-aminobenzoic acid and its application in fabrication of a polyoxometalates-consisting monolayer and multilayer films, Langmuir. 16 (2000) 7471–7476.

[34] X.F. Huang, Z.H. Zhang, Q.Q. Zhang, L.Z. Wang, M.Y. He, Q. Chen, G.Q. Song, L. Wei, F. Wang, M. Du, Norfloxacin salts with benzenedicarboxylic acids: Charge-assisted hydrogen-bonding recognition and solubility regulation, CrystEngComm. 15 (2013) 6090–6100.

[35] B. Beykal, M. Herzberg, Y. Oren, M.S. Mauter, Influence of surface charge on the rate, extent, and structure of adsorbed Bovine Serum Albumin to gold electrodes, J. Colloid Interface Sci. 460 (2015) 321–328.

[36] P. Mashazi, T. Nyokong, Electrocatalytic studies of covalently immobilized metal tetra-amino phthalocyanines onto derivatized screen-printed gold electrodes, Microchim. Acta. 171 (2010) 321–332.

[37] R.K. Mendes, R.S. Freire, C.P. Fonseca, S. Neves, L.T. Kubota, Characterization of Self-Assembled Thiols Monolayers on Gold Surface by Electrochemical Impedance Spectroscopy, J. Braz. Chem. Soc., 15 (2004) 849–855.

[38] J. Cecchetto, A. Santos, A. Mondini, E.M. Cilli, P.R. Bueno, Serological point-of-care and label-free capacitive diagnosis of dengue virus infection, Biosens. Bioelectron. 151 (2020) 111972 (1-7).

[39] P. Zhurauski, S.K. Arya, P. Jolly, C. Tiede, D.C. Tomlinson, P. Ko Ferrigno, P. Estrela, Sensitive and selective Affimer-functionalised interdigitated electrode-based capacitive biosensor for Her4 protein tumour biomarker detection, Biosens. Bioelectron. 108 (2018) 1–8.

[40] S.K. Arya, P. Zhurauski, P. Jolly, M.R. Batistuti, M. Mulato, P. Estrela, Capacitive aptasensor based on interdigitated electrode for breast cancer detection in undiluted human serum, Biosens. Bioelectron. 102 (2018) 106–112.

[41] A. Shrivastava, V.R. Gupta, Methods for the determination of limit of detection and limit of quantitation of the analytical methods, Chronicles Young Sci. 2 (2011) 21–25.

[42] C. Fernández-Sánchez, C.J. McNeil, K. Rawson, O. Nilsson, Disposable noncompetitive immunosensor for free and total prostate-specific antigen based on capacitance measurement, Anal. Chem. 76 (2004) 5649–5656.

[43] L. Huang, G. Reekmans, D. Saerens, J.M. Friedt, F. Frederix, L. Francis, S. Muyldermans, A. Campitelli, C. Van Hoof, Prostate-specific antigen immunosensing based on mixed self-assembled monolayers, camel antibodies and colloidal gold enhanced sandwich assays, Biosens. Bioelectron. 21 (2005) 483–490.

[44] N.F. Che Lah, A.L. Ahmad, S.C. Low, Molecular imprinted membrane biosensor for pesticide detection: Perspectives and challenges, Polym. Adv. Technol. 32 (2021) 17–30.

[45] G. Vasapollo, R. Del Sole, L. Mergola, M.R. Lazzoi, A. Scardino, S. Scorrano, G. Mele, Molecularly imprinted polymers: Present and future prospective, Int. J. Mol. Sci. 12 (2011) 5908–5945.

## CHAPTER 5

## 5. Ultrasensitive detection of prostate-specific antigen using glucose-encapsulated nanoliposomes anti-PSA polyclonal antibody as detection nanobioprobes


### Abstract

In this chapter, the preparation of glucose encapsulating nanoliposomes was achieved using two different lipid formulations**,** labelled as **F1** and **F2**. Both formulations contained phosphatidylcholine (PC), oleylamido-4-butanoic acid (OABA) and in addition **F1** contained cholesterol (CHO) while **F2** contained cholesteryl hemisussinate (CHEMS). These formulations were studied for their pH sensitivity and controlled release of encapsulated glucose for indirect detection of prostate-specific antigen (PSA) using sandwich immunoassay. As a signal generator, encapsulated glucose in nanoliposomes was quantified directly using the personal glucose meter (PGM) and colorimetrically using horseradish peroxidase (HRP) enzyme and Pd|PdO as nanoparticles. Controlled release of the encapsulated glucose was achieved using the pH effect or Triton-X 100 as a surfactant to destabilize the liposomal structure. The **F2** formulation showed maximum controlled release at acidic phosphate buffer saline (PBS, pH 5.0). The concentration of encapsulated glucose was found to be high in **F2** formulation and these were applied for the indirect detection of PSA. The limit of detection (LOD) values for PSA were found to be 0.050 $fg.mL^{-1}$, 0.160 $fg.mL^{-1}$ and 0.250 $fg.mL^{-1}$ when HRP, Pd|PdO and PGM were respectively used. The detection signal was linear over a wide concentration range for PSA including the clinical range of 4 – 10 $ng.mL^{-1}$. The HRP system showed low LOD value when compared with Pd|PdO nanoparticles and PGMs. Pd|PdO nanoparticles system showed good stability over a wide temperature up to 80°C. PGM system required less reaction time (2 min), low reagents and results were readily generated in digital format.

## 5.1 Introduction

In the recent years, biosensor research has put much efforts into the development of point-of-care testing (POCT) devices [1]. POCT is a rapidly developing field involving near-patient, bedside, ancillary, or in-field testing and monitoring. It enables a wide range of bioanalytes to be tested easily and quickly without the use of laboratory-based equipment or well-trained personnel [2]. Amongst the point-of-care devices, sensors and biosensors based on colorimetric [3–5] and electrochemical [6–10] detection techniques have attracted great interest. This was simply because of their operational simplicity, affordability, long shelf-life, high selectivity, and sensitivity [11–13]. Considerable efforts have also been channelled towards developing patient self-testing devices for their health monitoring such as pregnancy testing, blood pressure monitoring, detection of drugs of abuse, and monitoring blood glucose.

The personal glucose meters (PGMs) [8, 14, 15], and lateral flow tests (LFTs) [16] are the most successful examples of POCT devices. They have been widely applied in household setups due to their miniature sizes, affordable prices, reliable and reproducible results, and simple operation [14, 16]. PGMs have been used for the monitoring and quantifying of blood glucose by diabetes sick persons. However, most recent research has explored the use of PGMs for the quantification and detection of non-glucose analytes such as drugs of abuse, disease biomarkers and heavy metals [14, 15, 17]. LFTs have also been used to develop both presumptive and confirmatory detection platforms for various bioanalytes including Covid-19 [18]. The use of nanoparticles and enzymes for colorimetric detection in LFTs has received enormous research attention. Traditionally, liposomes are used as drug delivery vehicles [19–22]. Recently, liposomes have been used as carriers for signal enhancing labels including glucose [5, 8] for sensing applications. Rongrong's group [5] successfully studied the formulation of liposomes encapsulating glucose using PMG for colorimetric immunoassay of streptomycin. In their work, they used a molar ratio of 50:10:1 of soybean phospholipids, cholesterol, and phosphoethanolamine. The PGM was used to detect streptomycin in a colorimetric immunoassay. Juan's group [8] also reported a PGM-based immunosensing strategy suitable for complex systems with signal amplification using surfactant-responsive cargo release from glucose-encapsulated liposomes. PGMs were used for the detection of aflatoxin where a

sandwich immunoassay approach was utilized. The glucose-loaded liposomes were conjugated with antibodies to specifically bind to the antigen (aflatoxin).

Many challenges still exist despite the successful use of liposomes as cargo carriers for the sensing indicators like glucose [5, 8], nanoparticles [23], and enzymes [14]. Some of the challenges include: (i) low concentrations of glucose encapsulated, which may affect the immunoassay sensitivity and later the limit of detection; (ii) stability at physiological conditions which can also result in a false reading; and (iii) uncontrolled release or leakage of the encapsulated glucose which can lead to a false reading. The challenges above can directly affect the selectivity and much more the sensitivity of the sensing system. Hence, the need for the development of a more robust liposomal formulation that will be more stable and thus allowing for controlled release sensing probes.

In this chapter, the preparation of glucose-encapsulating nanoliposomes (GENLs) for controlled release studies and detection of PSA was studied. The GENLs were prepared using two different lipid formulations, **F1** and **F2**. **F1** formulation contained phosphatidylcholine (PC), cholesterol (CHO), and oleylamido-4-butanoic acid (OABA). **F2** formulation contained PC, cholesteryl hemisussinate (CHEMS), and OABA. Both **F1** and **F2** formulations had a mole ratio of 20:7:1. The choice of the lipids used was motivated by literature in cases of PC, CHO, and CHEMS. Liposomes formed from the combination of PC and CHO [21,24] have shown facile formation, while those involving CHEMS [24, 25] have shown pH sensitivity. Therefore, CHEMS would exhibit high stability and pH sensitivity due to its fusogenic properties. OABA was used due to its modifiable head group and for the attachment of polyclonal anti-PSA antibodies (anti-PSA-pAb) for sensing. The quantification of glucose encapsulated in GENLs for the detection of PSA was studied using nanoparticles (Pd|PdO), PGM, and HRP and compared for sensing of PSA.

This chapter was set out to achieve the following aim of the thesis:

(e) To develop an ultrasensitive comparative detection of PSA using glucose-encapsulated nanoliposomes bioconjugated with anti-PSA polyclonal antibody nanobioprobes.

## 5.2 Experimental

### 5.2.1 Materials and methods

L-α-phosphatidylcholine was purchased from Avanti Polar Lipids. Oleylamine, succinic anhydride (SA), polycarbonate membranes, D-glucose, 3,3',5,5'-tetramethylbenzidine (TMB), horseradish peroxidase (HRP), glucose oxidase from Aspergillus Niger (GOx, EC 1.1.3.4), cholesteryl hemisussinate (CHEMS), cholesterol (CHO), 1-ethyl-3-(3-dimethylaminopropyl) carbodiimide hydrochloride (EDC), N-hydroxysulfosuccinimide (sulfo-NHS), disodium hydrogen phosphate ($Na_2HPO_4$), potassium dihydrogen phosphate ($KH_2PO_4$), sodium hydroxide (NaOH), hydrochloric acid (HCl), hydrogen peroxide ($H_2O_2$), absolute ethanol (EtOH) and palladium (II) chloride ($PdCl_2$) were purchased from Sigma Aldrich. The EDC and sulfo-NHS solutions were prepared fresh before use. Float-A-Lyzer® with a proper MWCO (12 kDa) was used to remove physically adsorbed glucose not encapsulated within the liposomes. The monoclonal anti-prostate specific antibodies (anti-PSA-mAb), polyclonal anti-prostate specific antibodies (anti-PSA-pAb), and prostate-specific antigens (PSA) were purchased from Biorad Laboratory Ltd. Oleylamine-5-butanoic acid (OABA) was synthesized and characterized following the method reported in **Scheme 5.1.** The successful formation of OABA was confirmed using FT-IR and $^1$H NMR. Palladium nanoparticles (Pd|PdO) were also synthesized and characterized**.**

The particle size and shape of the prepared GENLs and Pd|PdO nanoparticles were characterized using dynamic light scattering (DLS) and transmission electron microscopy (TEM). The liposomes were diluted in double-distilled water in the ratio of 1:100 GENLs to water respectively. For DLS, a disposable cuvette was used and Zeta potential measurements were done in a disposable folded capillary cell (DTS 1060). TEM analysis was done by dropping the aliquot of the diluted GENLs on a formvar carbon-coated copper grid and allowed to dry at room temperature overnight before analysis. Pd|PdO nanoparticles were further characterized for chemical composition using X-ray photoelectron spectrometer (XPS).

### 5.2.2 Equipment

A Multiskan Sky Microplate Spectrophotometer was used to obtain the absorption spectra. Malvern Zetasizer Nano-ZS90 series S equipped with a 633 nm He/Ne laser was used to measure the hydrodynamic size and Zeta potential. Transmission electron microscopy (TEM) micrographs were obtained using a Zeiss Libra 120 TEM operating at 80 kV. Perkin–Elmer Universal AT08-98-u98-R Sampling accessory spectrum 100 FT-IR spectrometers was used to collect Infra-red spectra for the synthesized compound. Proton Nuclear Magnetic Resonance ($^1$H NMR) data was obtained using a Bruker 400 MHz NMR spectrometer in $CDCl_3$. The NMR data was analysed using MestreNOVA software for integration and peak picking.

A Kratos Axis Ultra DLD X-ray Photoelectron Spectrometer having a monochromatic $Al_\alpha$ X-ray source was used to acquire the XPS analysis equipped with the charge neutralizer. Both the survey and high resolution core-level spectra were used to acquire the chemical composition of Pd|PdO nanoparticles. The XPS was operated at a pressure below $5.0 \times 10^{-9}$ Torr in an argon environment. XPS survey spectra were collected using the following parameters: emission current was kept at 12 mA and the anode voltage at 15 kV; the pass energy was at 80 eV with the width 1200 eV, centre at 596.5 eV, and step size of 1 eV and dwell time of 100 ms. The quantitative analysis of the survey spectra was conducted by measuring the peak area of Pd 3d, C 1s, and O 1s. Pass energy of 40 eV and a step size of 0.1 eV was used to acquire the high resolution core-level spectra. All spectra binding energies were normalized for charge correction using the carbon (C 1s) at 284.9 eV as a reference point. The curve fitting was done using Vision processing software and Gaussian-Lorentzian peak shape after performing a linear background correction for each of the elements studied. Personal glucose meters (PGMs), Accu-Check Instant (Roche Diabetes Care) were purchased from Clicks Grahamstown local pharmacy.

### 5.2.3. Synthesis

#### 5.2.3.1 Synthesis of oleylamido-4-butanoic acid (OABA), Scheme 5.1

Oleylamido-4-butanoic acid (OABA) was obtained from reacting oleylamine (1.00 g, 3.74 mmol) and succinic anhydride (1.87 g, 18.60 mmol) in ethanol. The reaction mixture was stirred at room temperature for 24 hrs to afford a white precipitate. The precipitate was then filtered and washed with cold ethanol before recrystallization in acetone.

Yield = 1.20 g (87.5%) FT-IR: ($\nu$, $cm^{-1}$): 3301 (N-H), 3000 (=C-H), 2879 (C-H), 1688, 1634 (C=O); 1553 (N-H), 1057 (C-O-C), 1009 (C-C, cyclic). $^{1}H$ NMR (400 MHz, $CDCl_3$) $\delta$ [ppm]: 5.88 (t, 1H, N-H), 5.33–5.37 (t, 2H, C=C-H), 3.17 (td, 2H, C-H), 2.73-2.80 (t, 4H, C–H), 1.95-1.97 (td, 4H, C-H), 1.57 (q, 2H, C–H), 1.49 (tq, 2H, C-H), 1.43 (q, 2H, C-H), 0.879 (t, 3H, C-H).

#### 5.2.3.2 Preparation of D-glucose encapsulated liposomes

The liposomes were prepared following the two lipids formulations. The first formulation (**F1**) contained PC: CHO: OABA in the mole ratio of 20:7:1 respectively, while the second formulation (**F2**) was the same except the CHO was substituted with CHEMS. The glucose encapsulated nanoliposomes (GENLs) were prepared by the thin-film hydration method as reported in the literature [4, 20]. Briefly, a mixture of PC: CHEMS: OABA was solubilized in chloroform until a homogeneous solution. The solvent was then removed using a rotary evaporator under reduced pressure. The lipid thin film was dissolved in 5 mL of D-glucose solution (33.3 mM) while being agitated at 650 rpm with a magnetic stir bar to yield a turbid lipid suspension. The liposomal suspension was passed through a 200 µm polycarbonate nanoporous membrane to extrude the liposomes of uniform size. After extrusion, the formed GENLs solution was then dialyzed in PBS (pH 7.4) using a slide-A-Lyzer dialysis cassette (MWCO 12 kDa) at 4°C.

The choice of the lipid combination was motivated by the predetermined use of the liposomes. Phospatidylcholine was chosen as it is well known to form liposomes in the aqueous phase [24]. CHEMS is known to destabilize liposomes in acidic conditions and OABA was synthesized from oleylamine for the first time and was used to provide sites for the bioconjugation of the antibodies via the carbodiimide (EDC/NHS) chemistry [4]. CHO was used for **F1** formulation because of its ability to stabilize the liposomes and substitute for CHEMS in **F2** formulation. The same procedure for liposome formulation was followed.

#### 5.2.3.3 Confirmation of D-glucose encapsulation

The amount of glucose encapsulated within the liposomes was evaluated using colorimetric reaction (HRP or Pd|PdO) and PGM as signal generators. The rationale was that liposomes would release glucose upon lysis using Triton-X 100 (surfactant) or in acidic buffer (pH 5.0) conditions. For colorimetric determination, the released glucose from the liposomes would be enzymatically catalysed by glucose oxidase (GOx) enzyme to gluconic acid and hydrogen peroxide ($H_2O_2$) would be produced as by-product. The produced $H_2O_2$ would then oxidize HRP via a two-electron oxidation process to produce HRP (+5) and $H_2O$. In the presence of chromagen like TMB (electron donor), HRP (+5) will be reduced to HRP (+3) and TMB is oxidized to 3,3',5,5'-tetramethylbenzidiimine (TMBDI), blue colour product with an absorption maxima at 370 nm and 652 nm under UV-Vis [3, 26–28]. For a control experiment, no Triton-X was added to a solution and no lysis occurred which in turn resulted in no glucose released for the enzymatic reaction colour development. To carry out the peroxidase analysis, 50 µL of GENLs were mixed with 200 µL (1.0 $mg.mL^{-1}$) of GOx, 50 µL of TMB (0.50 $mg.mL^{-1}$). After 2 min of gentle shaking at room temperature, 50 µL of Triton-X (0.10 $mg.mL^{-1}$) was added and followed by 50 µL of HRP (10 $ng.mL^{-1}$). The mixture was incubated at room temperature for 5 min, the blue colour developed. Triton-X 100 was not added to the control experiment henceforth no colour change was observed.

#### 5.2.3.4 pH Effect on GENLs

The pH effect on GENLs was studied by adjusting the pH of the liposomal solution from pH 5.0 – pH 7.0 at 0.5 intervals. After which the aliquot of each pH value was incubated for 30 min and then analyzed under UV-vis in the presence of GOx, TMB and HRP to give an absorbance as described in *Section 5.2.4*.

#### 5.2.3.5 Bioconjugation of anti-PSA polyclonal antibody (anti-PSA-pAb) to GENLs

The bioconjugation of the anti-PSA-pAb to the GENLs was achieved via carbodiimide chemistry. The activation of the OABA carboxylic acid groups was done by adding EDC (5.5 μmol) and sulfo-NHS (0.14 mmol) onto 5 mL of GENLs (20 $mg.mL^{-1}$) in PBS (pH 7.4). The reaction mixture was agitated and allowed to react. After 2 hrs, the liposomes were dialyzed to remove unreacted EDC and sulfo-NHS. Then, 100 μL of anti-PSA-pAb (1.0 $mg.mL^{-1}$) was added into the EDC/sulfo-NHS activated liposomal solution and allowed to react overnight at 4°C. The unconjugated anti-PSA-pAb in pH 7.4 was separated by dialysis using a 35 kDa MWCO membrane. 1% BSA was also incubated with GENLs-anti-PSA-pAb to block non-specific binding sites to yield GENLs-anti-PSA-pAb|BSA. The bioconjugated GENLs were separated by dialysis using the 35 kDa MWCO membrane.

#### 5.2.3.6 Synthesis of Pd|PdO nanoparticles

The synthesis of Pd|PdO nanoparticles was done using hydrothermal method as follows: a mixture of $PdCl_2$ (90 mg, 0.50 mmol) and HCl (100 mL, 32% v/v) in 45 mL ultra-pure water was magnetically stirred for 30 min to form a homogenous solution to form $H_2PdCl_4$. Into this solution, NaOH (0.32 g, 8.0 mmol) was added and the reaction mixture was stirred for further 30 min. $H_2PdCl_4$ was involved in the hydrolytic decomposition transformation into palladium hydroxide [29]. Lastly, 10 mL of 50% $H_2O_2$ was added dropwise into the reaction mixture under reflux with continuous stirring for 48 hours. The reaction mixture was cooled to room temperature, centrifugated at 9000 rpm and washed with deionised water and ethanol several times before drying in the oven for 12 hrs.

#### 5.2.3.7 Detection of human PSA by ELISA using GENLs for signal generation

Positive control wells of high binding polystyrene were modified by adding 50 µL of anti-PSA-mAb (10 ng.mL$^{-1}$) dissolved in sodium carbonate (pH 9.6) and incubated at 4°C, overnight. The wells modified with anti-PSA-mAb acted as capture for PSA. The microplate wells were allowed to equilibrate to room temperature and washed three times with PBS (pH 9.6). For blocking non-specific binding sites, 300 µL of blocking buffer PBS (pH 9.6) containing 1% BSA was incubated for 1 hr at room temperature to yield wells modified with anti-PSA-mAb|BSA. The wells were washed three times with PBS (pH 9.6) followed by PBS (pH 7.4). The negative control wells were modified with only 300 µL of blocking buffer containing 1% BSA.

For analyte capture or sensing, 50 µL of the target analyte (PSA) in varying concentrations was dissolved in PBS (pH 7.4), added to each corresponding microplate well and incubated for 1 hr to yield well/anti-PSA-mAb|BSA|PSA. Following this incubation, the microplate wells were washed three times with PBS (pH 7.4) to remove the unbound PSA. For the detection, 50 µL of the as-prepared antibody-nanoliposomes (GENLs-anti-PSA-pAb|BSA) (20 mg.mL$^{-1}$) was added to the wells and incubated for 30 min at room temperature to yield sandwich immunoassay. The unbound antibody-nanoliposomes were washed three times with PBS (pH 7.4). The negative wells were treated the same way except the anti-PSA-mAb step was deliberately omitted. In the negative wells, we expected no PSA capture and then no sandwich immunoassay formation.

### 5.2.4 Three signal generation mechanisms investigated

#### 5.2.4.1 Colorimetric detection of PSA using HRP

(i) PBS (pH 5.0) or 1% Triton-X 100 (surfactant) solution 20 µL was added to the microplate wells to lyse the GENLs-anti-PSA-pAb|BSA and release D-glucose encapsulated within the liposomes. (ii) The microwell plates were agitated for 30 min. (iii) GOx (10 µL, 2.0 mg.mL$^{-1}$), 10 µL of TMB (0.45 mM) was added to the solution followed by 10 µL of HRP (10 ng.mL$^{-1}$).

(iv). The mixture was allowed to react with gentle shaking for 30 min upon which, a blue colour developed and (v) the UV-vis spectra measured.

Only the microplate wells with the detecting liposomes (sandwich immunoassay) showed blue colour development. The negative control wells were without the analyte (PSA) also without the anti-PSA-mAb and no liposomes were captured leading to no colour development.

#### 5.2.4.2 Colorimetric detection of PSA using Pd|PdO nanoparticles

The first two steps involving lysis of liposomes and agitation as discussed in *Section 5.2.4.1* using PBS (pH 5.0) or triton-X 100 was followed leading to the release of glucose. After 30 min of incubation, a solution containing 10 µL TMB (0.45 mM), 20 µL of acetate buffer (pH 4) and 10 µL of Pd|PdO (1.0 $mg.mL^{-1}$) was added to the microplate wells. The mixture was subjected to gentle shaking for 20 min before UV-vis measurements were done. The blue colour developed in the wells containing PSA due to the sandwich immunoassay formation. Similar to *Section 5.2.4.1*, the blue colour intensity increased with the increasing concentration of PSA. Also microwells without PSA and those without capture antibodies (anti-PSA-mAb) did not show observable blue colour development.

#### 5.2.4.3 Detection of PSA using PGM

Using the PGM, the previous procedure for lysing liposomes in *Section 5.2.4.1* was followed. After which, 3 µL aliquot of the lysis solution was drawn out of the microwell and placed on the glucose testing strip for measurement. The obtained PGM digital output increased with increasing PSA concentration. The measurement of glucose concentration in relation to PSA concentration using PGM was conducted at room temperature and in triplicates. The microwells without PSA and those without anti-PSA-mAb show undefined value as no glucose was present and PGM could not display the value.

## 5.3 Results and discussion

### 5.3.1 Synthesis of OABA, Scheme 5.1

As one of the components for the preparation of GENLs, OABA was synthesized to introduce the carboxylic functional group. The amine functional group of oleylamine was converted into carboxylic acid group by reacting with succinic anhydride via the amide bond formation. The characterization of the OABA was conducted using FTIR and $^{1}$H NMR.

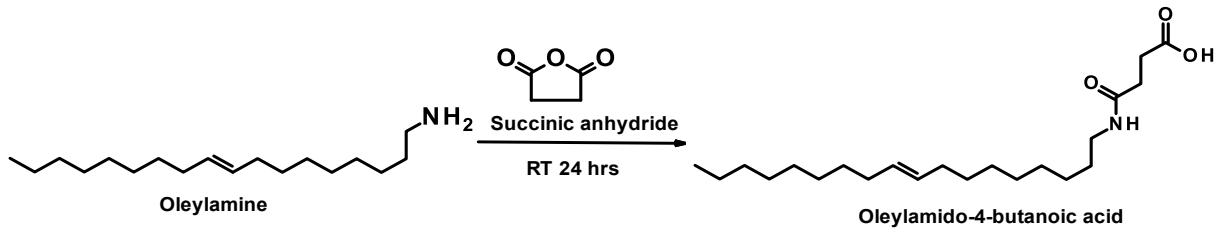


**Scheme 5.1:** The synthesis of oleylamido-4-butanoic acid from oleylamine and succinic anhydride.

**Figure 5.1** shows the IR spectra for the synthesis of OABA and its starting materials. From the IR spectra of the product, the functional groups confirmed the successful formation of OABA. The carbonyl (C=O) vibrational bands splits into two for the amide bond at 1634 $cm^{-1}$ and the carboxylic acid group at 1688 $cm^{-1}$ of the AOBA. The carbonyl vibrational band at around 1774 $cm^{-1}$ for the succinic anhydride disappeared. The sharp vibrational bands observed at 3301 $cm^{-1}$ and at 1553 $cm^{-1}$ were for the amine (N-H) stretch due to an amide group formed during the reaction between succinic anhydride and oleylamine. The formation of a carboxylic acid (-COOH) was observed and a stretch at 1688 $cm^{-1}$ confirming the formation of AOBA by the opening of succinic anhydride. The cyclic C-C and the ether (C-O-C) bonds of the succinic anhydride at 1009 $cm^{-1}$ and 1057 $cm^{-1}$ also disappeared confirming ring opening.

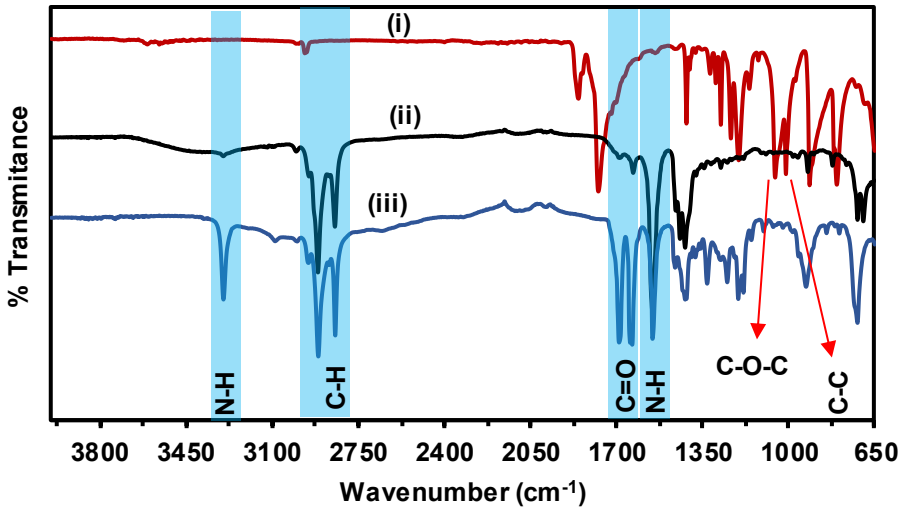


**Figure 5.1:** FT-IR spectra of (i) succinic anhydride, (ii) oleylamine, and (iii) oleylamido-4-butanoic acid.

The proton NMR ($^1$H NMR) was used to characterize the purity of OABA. **Figure 5.2** shows the $^1$H NMR of the synthesized OABA measured dissolved in $CDCl_3$. The $^1$H NMR analysis showed a clean spectrum with the protons integrating and confirming the proposed structure as shown in **Scheme 5.1**. The presence of the four new protons due to C-H at 1.95-1.97 ppm confirmed the chain elongation due to the successful amide bond formation between succinic anhydride and oleylamine to form OABA. Furthermore, a proton due to the amide bond was also observed at 5.88 ppm. The other protons due to the oleylamine backbone chain were observed with a minor shift and integrated correctly confirming the successful formation of OABA with high purity.

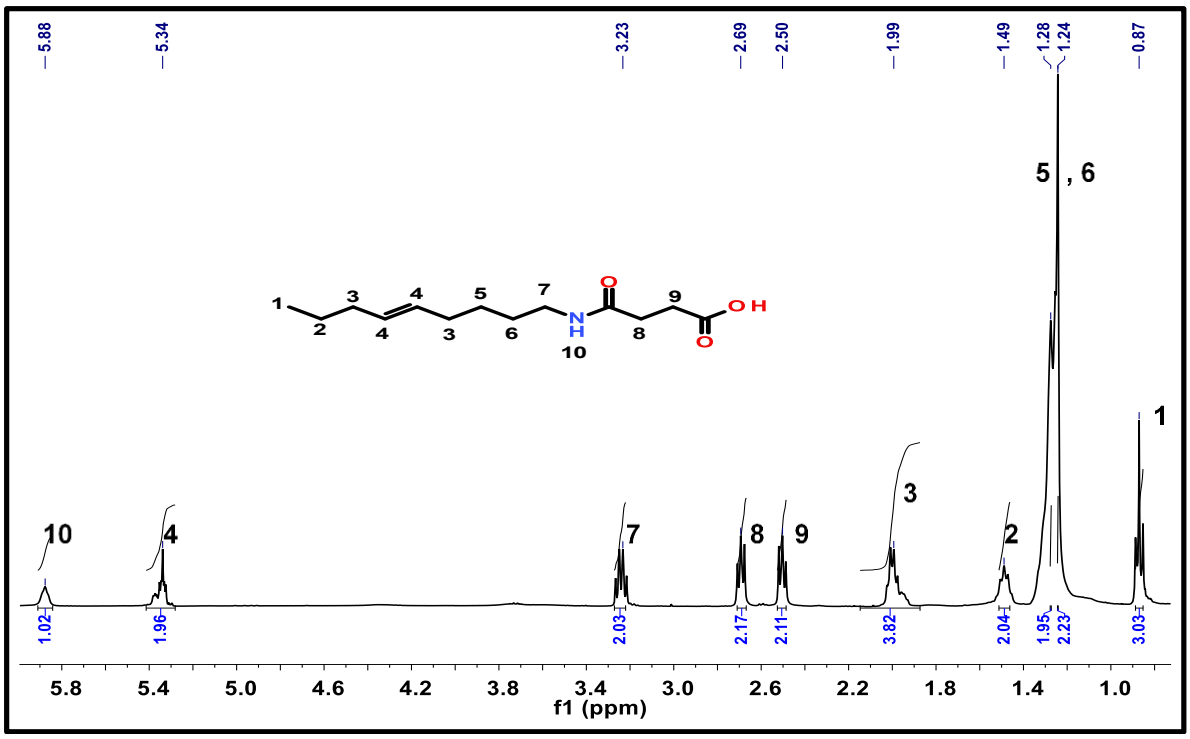


**Figure 5.2:** Proton NMR ($^1$H NMR) of OABA synthesized from succinic anhydride and oleylamine measured in $CDCl_3$.

### 5.3.2 Characterization of glucose-encapsulated nanoliposomes (GENLs)

The DLS results in **Fig. 5.3(a)** show that the liposomes have a uniform diameter of 109 nm for **F1** formulation and 164 nm for **F2** formulation. Both formulations had a polydispersity index (PDI) of 0.2. The TEM image of liposomes for **F2** is shown in **Fig. 5.3(b)** and for **F1** is shown as an inset. The liposomes were observed to be spherical with slight deformation and appeared as individual particles with the sizes of approximately 150-200 nm for **F2** formulation and 80-110 nm for **F1** formulation. The GENLs for **F1** was observed to be smaller than those of **F2** which contained CHEMS. This was attributed to the larger cross-sectional surface area occupied by the more negatively charged carboxylic group on the CHEMS than that of the alcohol group on the CHO. In addition, CHEMS contained a longer carbon chain length arising from the succinate moiety which contributes to the increase in the size of the GENLs [30].

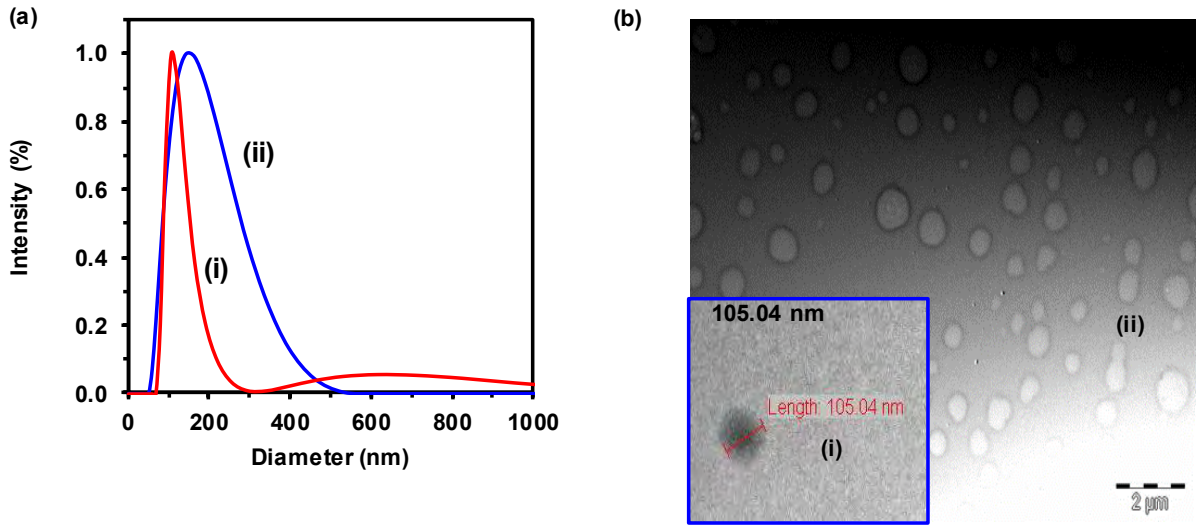


**Figure 5.3:** (a) DLS spectra and (b) TEM micrographs of (i) PC:CHO:OABA (**F1**) and (ii) PC:CHEMS:OABA (**F2**).

### 5.3.3 Confirmation of D-glucose encapsulation

**Figure 5.4(a)** shows the UV–vis spectra of the solutions containing (i) GENLs, GOx, and TMB, (ii) GENLs, GOx, TMB and HRP, (iii) GENLs, GOx, TMB, HRP, and 1% Triton-X. There was no observable signal in **Fig 5.4(a)(i)**. A small signal was observed for **Fig. 5.4(a)(ii)** and due to small amount of glucose on the surface of liposomes. The solution in which Triton-X was added, in **Fig. 5.4(a)(iii)**, resulted in the development of an intense blue colour and the UV-vis absorption spectrum showed an intense peak with absorption maxima at 652 nm. The blue colour of the solution confirmed the oxidation of TMB to TMBDI due to the release of glucose that was encapsulated in the core of the liposomes. Triton-X as a surfactant destabilized the liposomes which led to the release of D-glucose into the solution. The mechanism of colour development is as described in section 2.4 above. It is well-known that TMB oxidizes to TMBDI in the presence of hydrogen peroxide and HRP [3, 26, 27]. **Figure 5.4(b)** shows the UV-vis spectra of the solutions using (i) **F1** and (ii) **F2** GENLs in the presence of GOx, TMB, HRP, and 1% Triton-X. The spectra showed that the absorption intensity of **F2** was higher than that for **F1**. **F2** therefore contained a higher amount of encapsulated D-glucose molecules than

**F1**. The higher amount of the encapsulated D-glucose was due to the increased size of GENLs formed containing CHEMS.

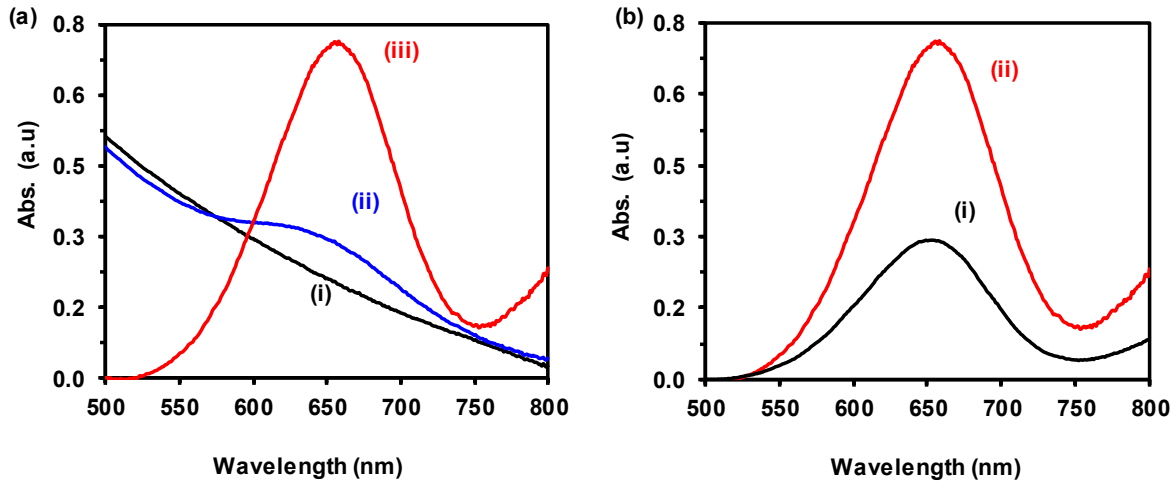


**Figure 5.4:** UV–vis spectra of the solutions containing **(a)** GENLs (50 µL) + GOx (200 µL, 1.0 mg.mL$^{-1}$) and (i) TMB (50 µL, 0.50 mg.mL$^{-1}$), (ii) TMB (50 µL, 0.50 mg.mL$^{-1}$) + HRP (50 µL, 10 ng.mL$^{-1}$); (iii) TMB (50 µL, 0.5 mg.mL$^{-1}$) + HRP (50 µL, 10 ng.mL$^{-1}$) + 1% Triton-X (50 µL). **(b)** GENLs (50 µL, 1.0 mg.mL$^{-1}$) + GOx (200 µL, 1.0 mg.mL$^{-1}$) + TMB (50 µL, 0.50 mg.mL$^{-1}$) + HRP (50 µL, 10 ng.mL$^{-1}$) + 1% Triton-X (50 µL) solutions of (i) **F1** and (ii) **F2** liposomes.

### 5.3.4 Encapsulation Efficiency

The calibration curve of known glucose concentration in **Fig. 5.5** was used to determine the concentration of D-glucose from the lysed liposomes after dialysis. The absorbance of the used volume of the liposomal suspension was recorded five times. This gave the mean value of 0.48 ± 0.02 a.u and a very low standard deviation. The mean was then recorded as the representative value of the absorbance of liposomal suspension. This value was then fitted into the calibration curve to calculate the concentration of glucose after dialysis. **Equation (5.1)** below was used to determine the percentage encapsulation efficiency (%EE) of D-glucose in the liposomes and it was found to be 60%.

$$\%EE = \frac{Abs_a}{Abs_b} x\ 100 \qquad (\mathbf{5.1})$$

where $Abs_a$ is the concentration of D-glucose after dialysis, $Abs_b$ is the concentration of D-glucose before dialysis. The amount of D-glucose was quantified from the encapsulation efficiency and it was found to be 1.71 ± 0.32 mg per 1 mg of the liposomal lipids.

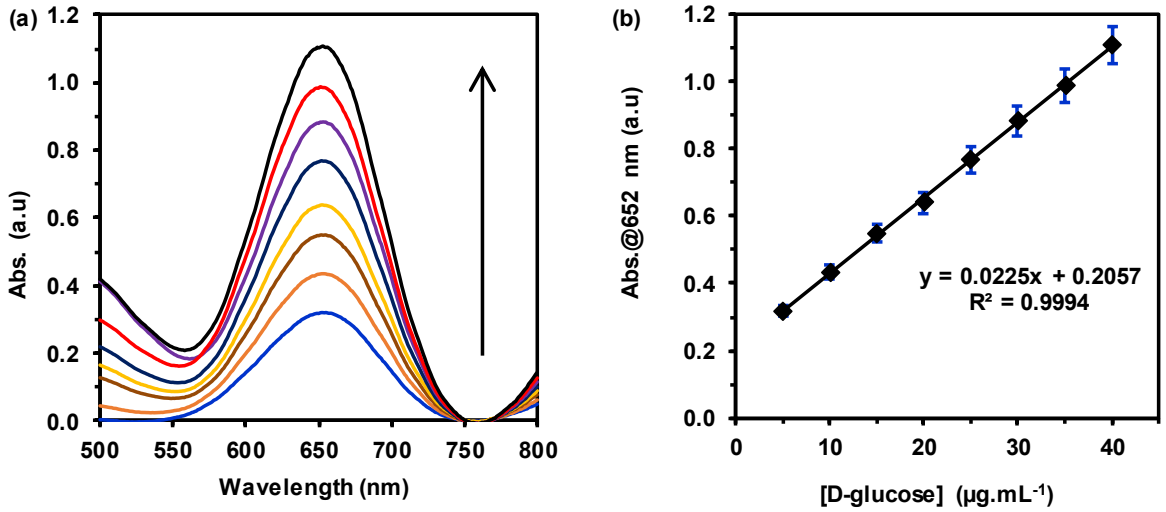


**Figure 5.5:** (a) UV-vis spectra at different glucose concentrations and (b) the corresponding calibration curve of known glucose concentration.

### 5.3.5 Effect of pH on liposomes encapsulated liposome

**Figure 5.6(a)** shows the effect of pH on the GENLs measured by UV-vis following absorbance of the blue color product (TMBDI). The absorbance was observed to decrease with increasing pH, with pH 5 having the highest absorbance and pH 7.5 having the lowest absorbance. The changes in absorbance were attributed to the amount of glucose released due to the disruption of the liposomes at pH 7.5 to pH 5.0. The released glucose was then used in the conversion of TMB to TMBDI as described above. Therefore, the more liposomal disruption, the more glucose was released and the higher the absorbance. The percentage of glucose released (%Glucose Release) at the respective pH was calculated using modified **Eq. (5.2)** reported in literature [24].

$$\%\text{Glucose Release} = \frac{A_{pH} - A_0}{A_{100} - A_0} \times 100 \qquad \textbf{(5.2)}$$

where $A_0$ is the absorbance at pH 7.4, $A_{pH}$ is the absorbance following incubation at acidic buffer pH and $A_{100}$ is the absorbance after the addition of Triton-X.

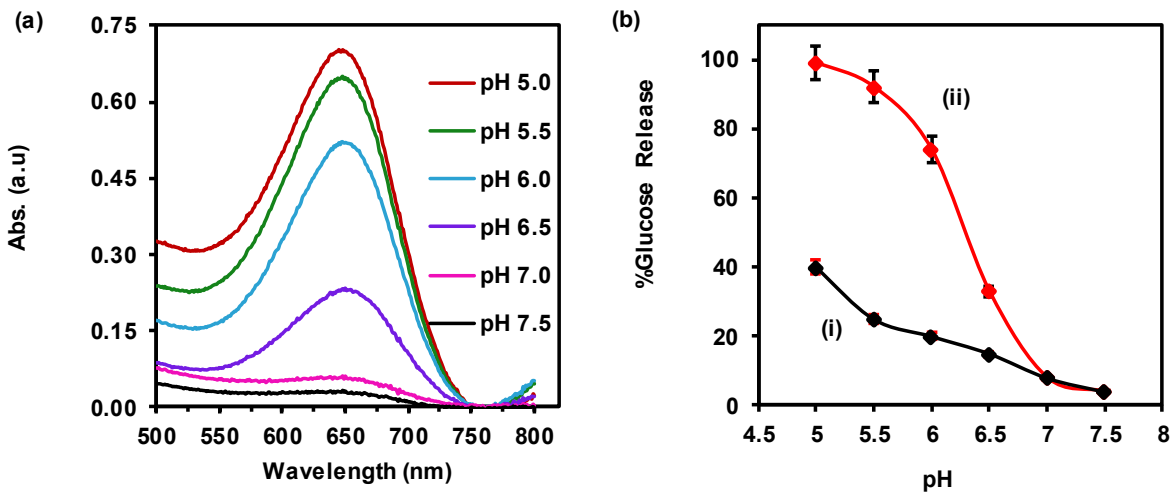


**Figure 5.6:** (a) UV-vis spectra at different pH conditions, from pH 7.5 to pH 5.0 for **F2** and (b) %Glucose Release at varied pH conditions from pH 7.5 to pH 5.0 for (i) **F1** and (ii) **F2**.

The intensity of the UV-vis spectra increased with the increase in the acidity of the solution from pH 7.5 to pH 5.0 with the maximum absorption observed at pH 5.0. This indicated the pH-responsive nature of the liposomes. The intensity of the absorbance at pH 7.5 and pH 7.0 was much lower for both liposomal formulations (**F1** and **F2**) indicating that the GENLs were stable at physiological pH, hence, no glucose was released. **Figure 5.6(b)** shows the amount of glucose released at a particular pH. It was observed that **F2** liposomal formulation showed a 99% of D-glucose release at pH 5.0, whilst at pH 7.5 less than 5% of D-glucose was released. On the contrary, the GENLs for **F1** liposomal formulation showed 40% of D-glucose release at pH 5.0. This suggested that **F1** GENLs were more stable at pH 5.0 than those of **F2**. In this work, the pH sensitivity of GENLs for **F2** liposomal formulation was attributed to the presence of CHEMS which exhibited fusogenic properties under acidic pH [31]. GENLs for **F2** were then further studied for the effect of pH on the size and shape using DLS and TEM.

**Figure 5.7** shows that the morphology of the **F2** liposome formulation under TEM were spherical, monodispersed, and stable at pH 7.5 to pH 6.5. The morphology of the liposomes was irregular in shape and aggregated from pH 6.0 to pH 5.0. This indicated that there was a disruption of the liposomal structure at acidic pH conditions triggering the release of glucose

and rearrangement of lipid formulations. The liposomes then aggregated and precipitated due to exposure of hydrophobic chains in an aqueous solution.

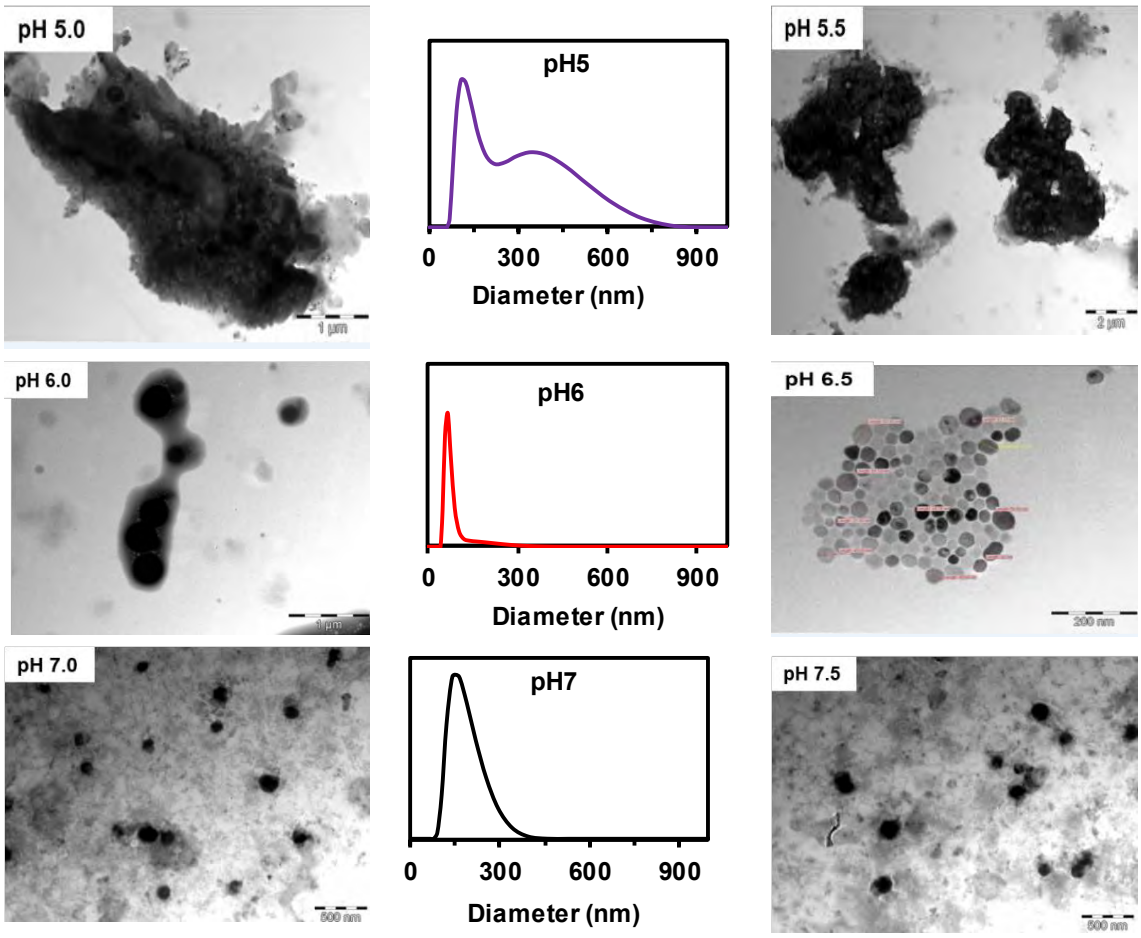


**Figure 5.7:** TEM images of **F2** liposomal formulations in varying pH conditions (pH 5.0 - pH 7.5).

The **F2** liposome formulation in **Fig. 5.7** shows stability at pH 7.0 and pH 7.5 in terms of size and distribution. The sizes at pH 7.0 and pH 7.5 were about 164 nm and monodispersed. The liposomes at pH 6.5 change the shape to more spherical and their size decreases to an average of 64 ± 5 nm. The size reduction resulted in the release of glucose with some glucose entrapped between the lipids. The middle column of **Fig. 5.7** shows the DLS at pH 5.0, pH 6.0, and pH 7.0. The DLS shows that the liposomes at pH 7.0 maintained the initial size (as prepared). This was confirmed from the TEM image where the liposomal particles are observed to be spherical and monodispersed. The liposomes at pH 6.0 showed size reduction and they were mono dispersed whereas at pH 5.0 they showed polymodal distribution under DLS with an average size of 450 nm which agreed with the TEM image at pH 5.0 that showed aggregation.

### 5.3.6 Quantification of encapsulated D-glucose using the PGM

The personal glucose meter (PGM) was also used to quantify precisely the amount of D-glucose encapsulated in the liposomes as shown in **Fig. 5.8**. About 5 µL of the dialyzed GENLs suspension was added into a microwell and diluted with 200 µL of PBS (pH 7.4). After 30 min of lysis time, 3 µL of the mixture was drawn out and placed on the measuring strip on the PGM and the glucose quantified. The control experiment **Fig. 5.8(a)**, contained 5 µL of GENLs and 200 µL of PBS (pH 7.4) and **Fig. 5.8(b)** contained 5 µL of GENLs and 200 µL of PBS (pH 5.0). It was observed that the solution diluted with PBS (pH 7.4) gave an undefined read-out due to a very low concentration of glucose and undetectable using the PGM. The aliquot in the well diluted with PBS (pH 5.0) gave a 5.5 mM reading. This further confirmed that the as-prepared GENLs were stable at pH 7.4 and disrupted at pH 5.0 releasing the encapsulated glucose. The 5.5 mM reading on the PGM indicated that the GENLs contained 2 mg of D-glucose per 1 mg of the lipids. This was similar to the value obtained using encapsulation efficiency and reported to be 1.71 ± 0.32 mg per 1 mg of the lipids.

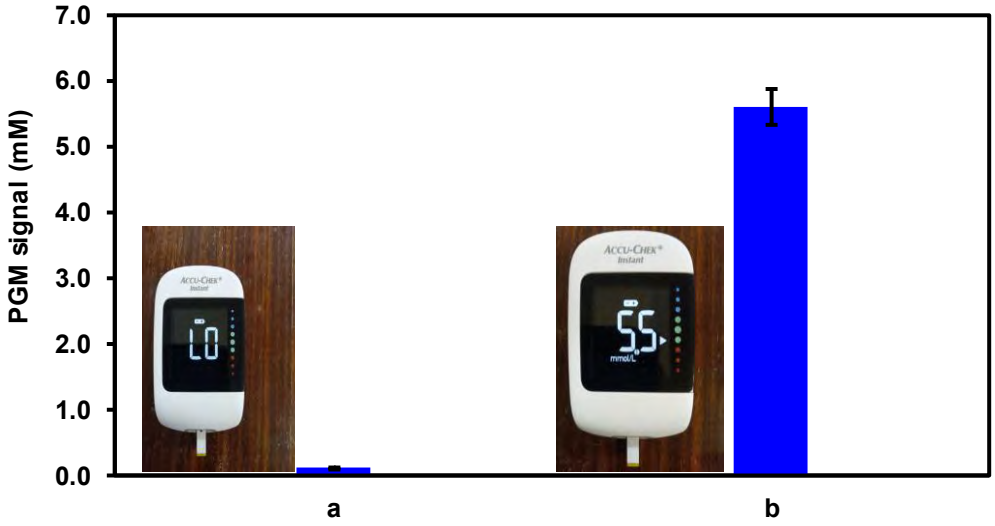


**Figure 5.8:** Bar graph of the reading on the PGM for the experiment containing 5 µL of GENLs and (a) 200 µL of PBS (pH 7.4) and (b) 200 µL of PBS (pH 5.0). Inset shows the PGM images showed reading at PBS (a) pH 5.0 and (b) pH 7.4.

### 5.3.7 Bioconjugation of anti-human PSA polyclonal antibody to the GENLs

The bioconjugation of anti-PSA polyclonal antibody (anti-PSA-pAb) to the GENLs was confirmed by DLS and Zeta potential. The effect of the antibody on the size and zeta potential was investigated. **Figure 5.9(a)** shows the DLS of the unconjugated (GENLs) and the conjugated (GENLs-anti-PSA-pAb) liposomes. The DLS plots show that there was a change in the diameter of the liposomes. The GENLs-anti-PSA-pAb showed a mean diameter of 190 ± 4 nm, whilst that of the GENLs show 164 ± 5 nm. The increase in size was attributed to the presence of the conjugated anti-PSA-pAb on the surface of the GENLs. The Zeta potential was further used to confirm the changes in the surface charge due to the introduction of the anti-PSA-pAb. The surface charge increased from -30 ± 5 mV for GENLs to -5 ± 2 mV for GENLs-anti-PSA-pAb as shown in **Fig. 5.9(b)**. The changes in the surface charge from -30 ± 5 mV to -5 ± 2 mV confirmed the presence of the anti-PSA polyclonal antibody and the neutralization of the OABA carboxylic acid functional groups. The anti-PSA polyclonal antibody was covalently bonded onto the GENLs via the carboxylic acid groups on the surface of the liposomes introduced by OABA. The DLS results did not show disruption of GENLs confirming their excellent stability.

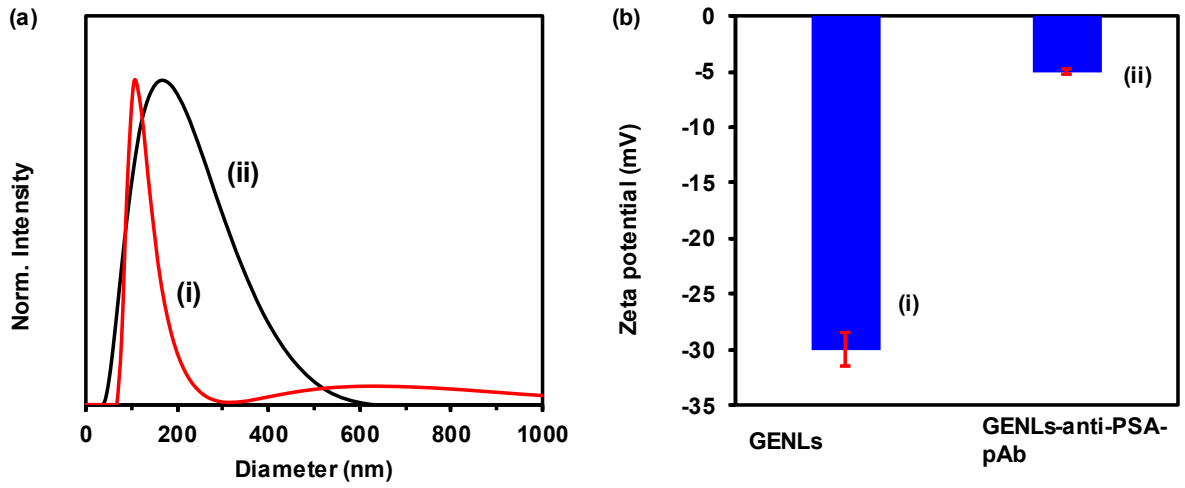


**Figure 5.9:** (a) DLS and (b) Zeta potential of the (i) GENLs and (ii) GENLs-anti-PSA-pAb.

### 5.3.8 Characterization of Pd|PdO nanoparticles

#### 5.3.8.1 UV-vis, DLS and TEM characterization of Pd|PdO nanoparticles

The formation of Pd|PdO nanoparticles was characterized using UV-vis absorption. **Figure 5.10(a)(i)** shows the UV-vis spectrum of palladium (II) chloride ($PdCl_2$) having an absorption peak due to $Pd^{2+}$ at around 483 nm. This peak disappears after the formation of the Pd|PdO nanoparticles indicating the conversion of $Pd^{2+}$ to $Pd^0$ [32]. Pd|PdO nanoparticles formation was also characterized using DLS and TEM. **Figure 5.10(b)** shows the DLS spectrum of the Pd|PdO nanoparticles in which the hydrodynamic average radius was found to be 8.0 ± 0.5 nm with a polydispersity index (PDI) of 0.11. The nanoparticles were small and monodispersed with regards to the small PDI. The TEM images shown in **Fig. 5.10(c)** with its corresponding histogram distribution in **(d)** shows that the Pd|PdO nanoparticles have a mean width of 7.0 ± 1.6 nm. These results agree with the DLS results.

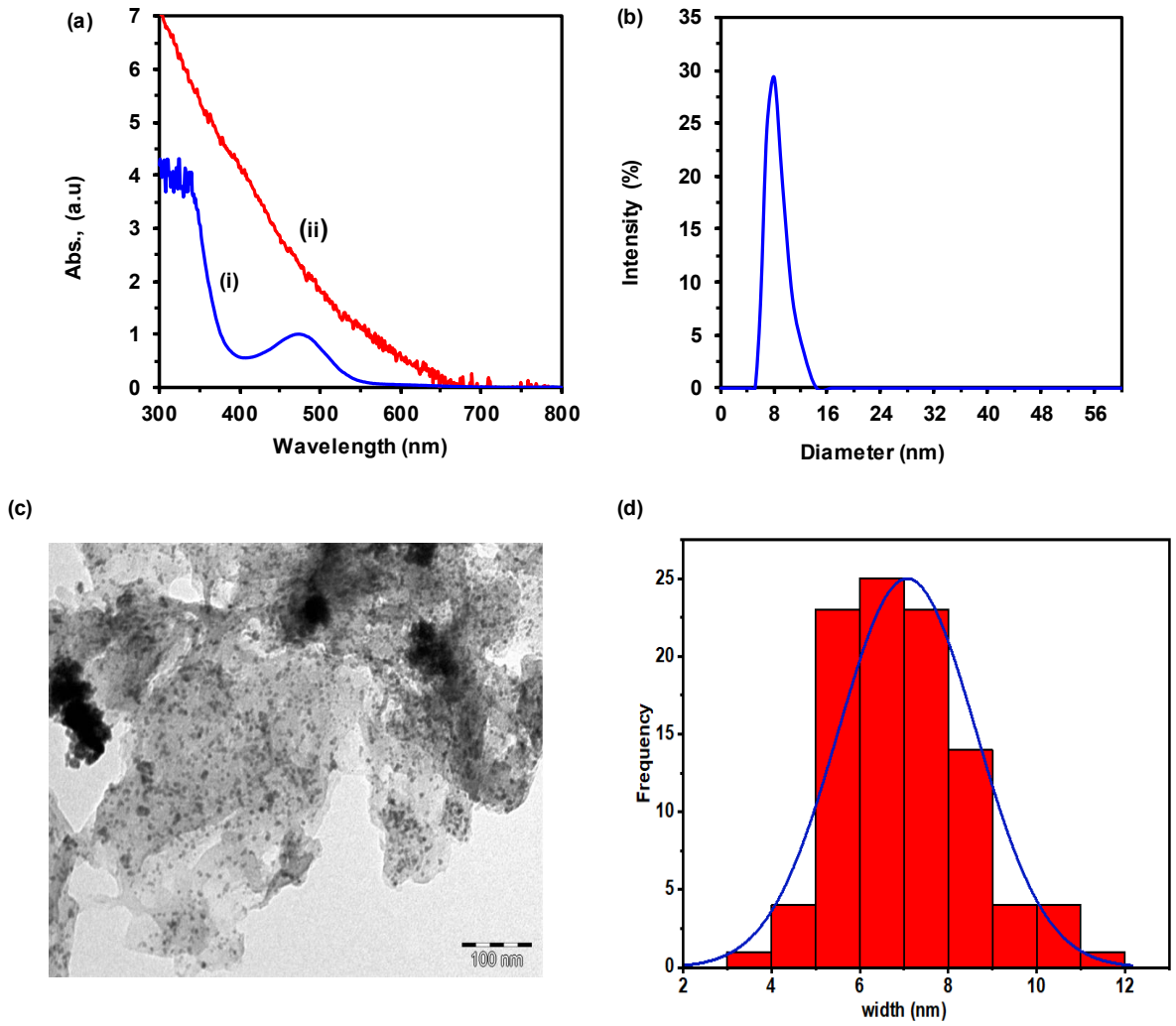


**Figure 5.10:** (a) UV-vis spectra of (i) $PdCl_2$ and (ii) Pd|PdO nanoparticles (b) DLS, (c) TEM micrograph and (d) histogram distribution for Pd|PdO nanoparticles.

### 5.3.8.2 XPS characterization of Pd|PdO nanoparticles

**Figure 5.11(a)** displays the XPS survey spectrum of the Pd|PdO nanoparticles which shows the presence of the presence of Pd 3d (12%) at 336.0 eV, O 1s (54.5%) at 531.0 eV and C 1s (22%) at 284.9 eV [33]. The presence of Pd 3d (12%) and the dominance of O 1s (32%) suggest the successful formation of the Pd|PdO nanoparticles. The high resolution core-level spectra of the Pd 3d, O 1s and C 1s is shown in **Fig. 5.11 (b)**, **(c)**, and **(d)** respectively. The high resolution core-level spectrum of the Pd 3d shows a doublet at 335.2 eV and 340.5 eV which is due to the presence of the metallic palladium nanoparticles ($Pd^0$). The other doublet shown at 335.7 eV

and 341.4 eV was due to the palladium ions ($Pd^{2+}$). The presence of $Pd^{2+}$ confirmed the formation of the PdO due to the oxidation of the $Pd^{0}$ surface [34]. The peaks at 339.0 eV and 344.2 eV are due to the residue palladium (II) hydroxide, $Pd(OH)_2$ and could also be due to the hydrate palladium oxide [33,35].

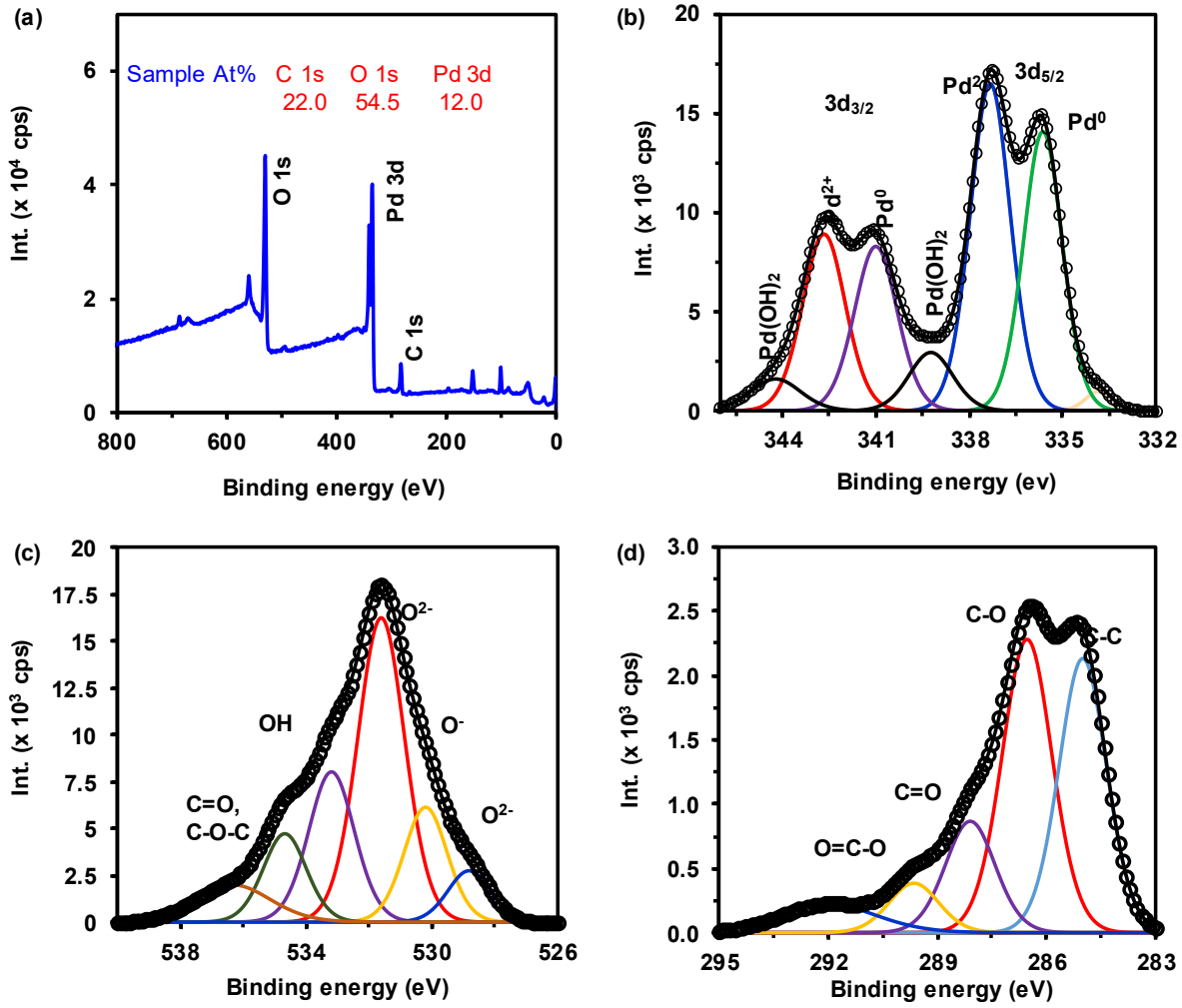


**Figure 5.11:** XPS (a) survey and high resolution core-level spectra of (b) Pd 3d, (c) O 1s and (d) C 1s.

**Figure 5.11(c)**, shows the O 1s high resolution core-level spectrum centred at 531.6 eV which was deconvoluted into six components. The components observed for O 1s were at 528.8 eV for lattice oxygen ($O^{2-}$), chemisorbed oxygen ($O^{2-}$), surface oxygen ($O^{2-}$) and oxygen due to chemisorbed hydroxyl groups from the sodium hydroxide (NaOH) and $H_2O_2$ used in the preparation of the Pd|PdO nanoparticles was observed (OH) at 533.4 eV [36]. The presence of the lattice and the surface oxygen species confirmed the presence of the Pd|PdO nanoparticles.

The O 1s component at 535 eV was assigned to the carbon-oxygen (C-O) bond or organic material contamination [33] due to ethanol used in the washing step. The organic material contamination was further observed on the C 1s high resolution spectrum in **Fig. 5.11(d)** which showed that the peaks at 284.9 eV and 288.0 eV are due to C-C and C-O respectively. The peaks at 286.5 eV and 291.9 eV are due to C-O and O=C-O respectively. The presence of these peaks justifies the presence of the ethanol as organic material.

### 5.3.9 Detection of prostate-specific antigen (PSA)

#### 5.3.9.1 Optimisation of D-glucose release and reaction time for the PSA colorimetric detection

**Figure 5.12** shows UV-vis spectra of glucose sensing in a microwell at varying times after the addition of the GOx and TMB and their corresponding line graph of Abs. (a.u) vs time (min), for (a) HRP and (b) Pd|PdO nanoparticles. For HRP in **Fig. 5.12(a)**, the UV-vis spectra in the presence of GOx, TMB and glucose at different pH values show the increase in absorbance with time up to 30 min then it decreased afterward. The optimum reaction time was 30 min and was used in the quantitative determination of PSA concentrations. For Pd|PdO nanoparticles in **Fig. 5.12(b)**, the UV-vis spectra of glucose sensing in the presence of GOx, TMB, acetate buffer pH 4.0 showed an increase in absorbance with time. The absorbance increased up to 20 min and then decreased afterward.

The optimum reaction time in Pd|PdO nanoparticles system was 20 min and 10 min faster than that of HRP. The faster reaction time was observed in the Pd|PdO nanoparticles as compared to the HRP and was attributed to the increased catalytic reactive sites present in the Pd|PdO. Pd|PdO nanoparticles displayed enzyme (HRP)-like activity and can be evaluated as enzyme or peroxidase mimetics. The signal intensity was lower than that of HRP. The effect of pH on the HRP enzyme catalysis has been studied [37]. The Pd|PdO nanoparticles are novel materials and these were studied for the effect of pH. The effect of buffer on the Pd|PdO nanoparticles system was best in acetate buffer compared to PBS. **Figure 5.12(c)** was used to investigate the effect of varying pH of acetate buffer. The optimum pH was found to be at pH 4.0. The highest

absorbance value was obtained at pH 4.0 and this was the optimum for Pd|PdO enzyme catalysis. The optimum conditions observed for each system were now applied for the quantitative detection of PSA.

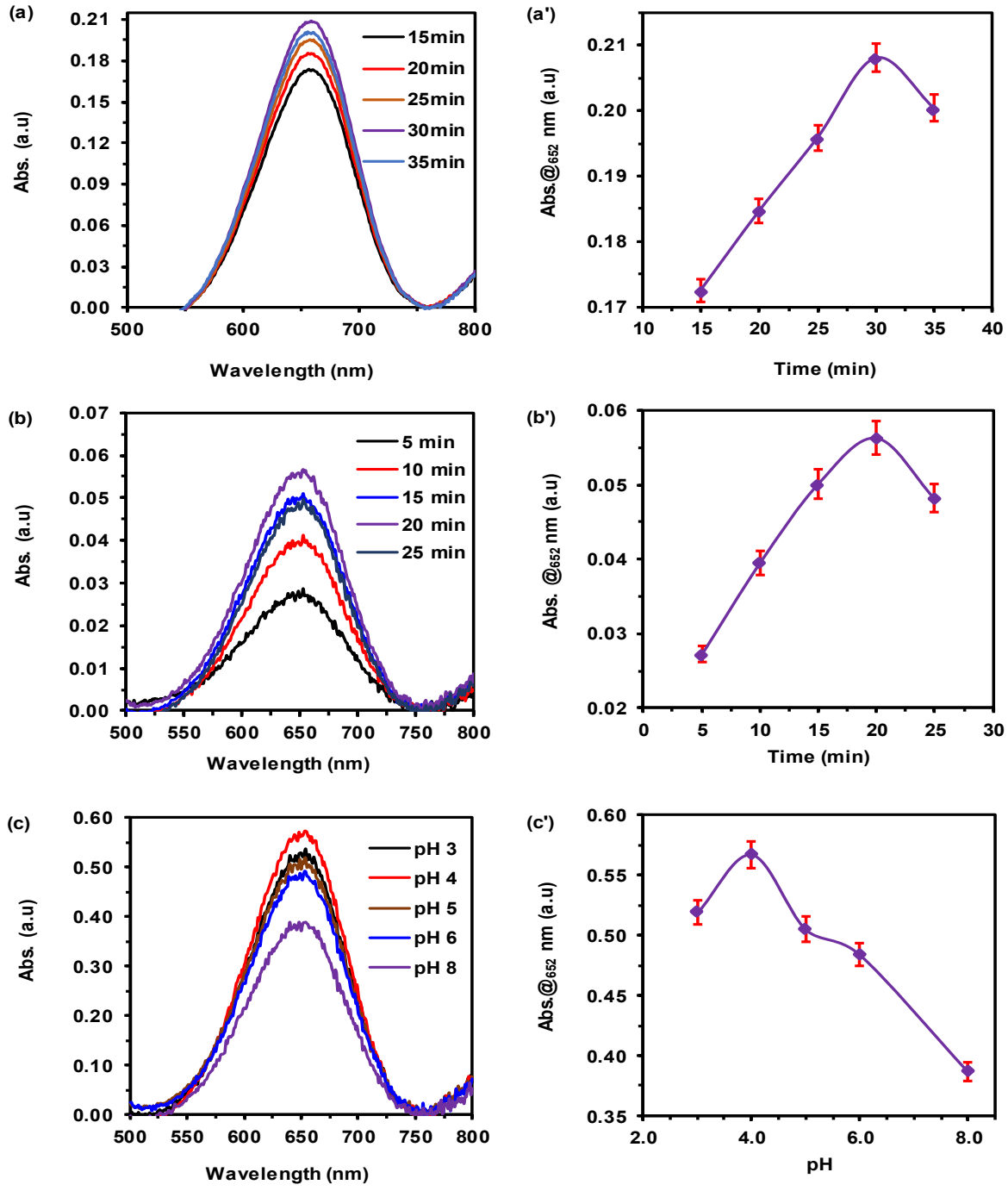


**Figure 5.12:** UV-vis spectra of glucose detection at the microwell containing GOx and TMB using (a) HRP, (b) Pd|PdO nanoparticles, and (c) UV-vis spectra Pd|PdO nanoparticles in the presence of GOx, TMB and glucose at different acetate buffer pH values.

### 5.3.9.2 Quantitative detection of PSA

The quantitative detection of PSA using HRP and Pd|PdO nanoparticles was achieved by using the optimized experimental conditions for each system. The standard solutions of PSA in a concentration range of 0.10 pg.mL$^{-1}$ to 100 mg.mL$^{-1}$ were added to the microwell containing the capture monoclonal antibody (anti-PSA-mAb|BSA). After thorough washing of the uncaptured PSA, GENLs-anti-PSA-pAb were then added to form a sandwich immunoassay. After thorough washing of the unbound GENLs-anti-PSA-pAb, a solution of Triton-X or PBS (pH 5.0) was added to lyse the liposomes. A solution mixture containing GOx; TMB and HRP or Pd|PO nanoparticles was added to the microwell. The release of D-glucose in the presence of GOx, TMB, and HRP or Pd|PdO nanoparticles produced a blue colour that absorbs at 652 nm as discussed above. The quantitative detection of PSA in this study was also carried out using the PGM. The PGM was used in this work to develop a point-of-care testing model for digital monitoring of PSA.

**Figure 5.13** shows UV-vis absorption spectra of the quantitative detection of PSA using (a) HRP and (b) Pd|PdO nanoparticles and (c) PGM quantitative signal (bar graph) systems with their respective calibration curves of absorbance versus [PSA]. It was observed from **Fig. 5.13(a)** and **(b)** that the absorption intensity increased with an increase in the concentration of PSA from 0.10 pg.mL$^{-1}$ to 100 mg.mL$^{-1}$ on both the HRP and the Pd|PdO nanoparticles. This indicated that the absorption signal was dependent on the concentration of PSA. **Figure 5.13(c)** shows the bar graph of PGM measurement reading at different PSA concentrations. The respective calibration curves show that the readings were linearly dependent to the [PSA] for all the detection systems, that is, (a′) HRP, (b′) Pd|PdO nanoparticles, and (c′) PGM. A linear relationship was obtained [PSA] concentrations between 0.10 pg.mL$^{-1}$ to 100 mg.mL$^{-1}$. The comparative study of the detection of PSA showed that limits of detection (LOD) were found to be 0.050 fg.mL$^{-1}$, 0.160 fg.mL$^{-1}$, and 0.250 fg.mL$^{-1}$ for HRP, Pd|PdO, and PGM respectively. The LOD was calculated based on **Eq. (5.3)** as reported in literature [38,39] :

$$LOD = \frac{3.SD_b - b}{\mathrm{m}} \qquad \textbf{(5.3)}$$

where $SD_b$ is a standard deviation of the absorbance or the PGM reading of the sample without PSA, b is the y-intercept of the linear gragh and m is the slope of the slope of the linear gragh.

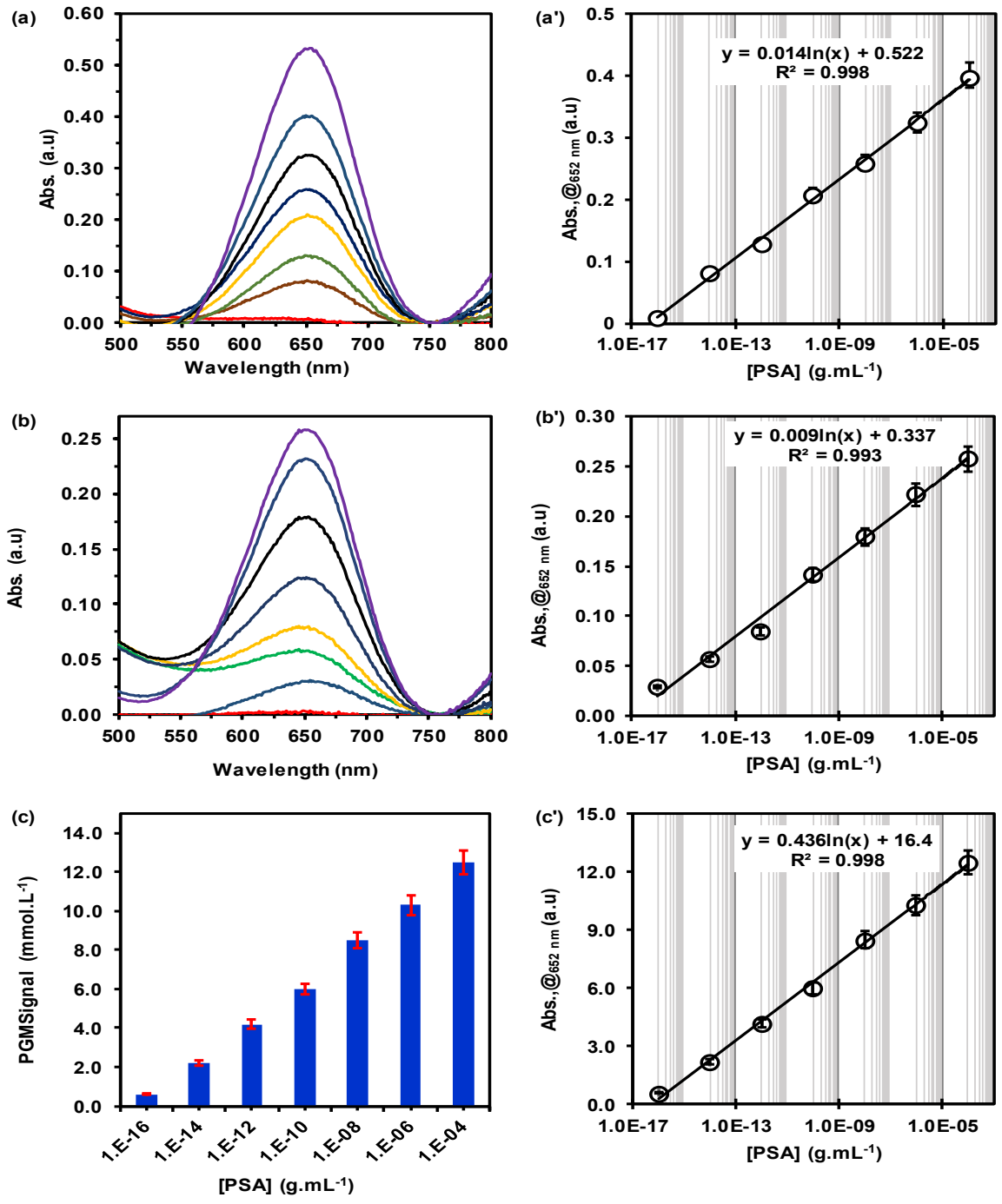


**Figure 5.13:** UV-vis absorption spectra and the corresponding calibration curves for the quantitative detection PSA using (a) HRP and (b) Pd|PdO nanoparticles, (c) the bar graph for the quantitative detection of PSA using PGM, and the calibration curve of PGM reading versus the [PSA].

The increase in absorbance within the studied concentration range of PSA was linear with the regression **Eqs. (5.4) - (5.6)** for HRP, Pd|PdO nanoparticles and PGM respectively:

$$Abs_{@652nm} = 0.014\ln(x) + 0.522 \ (R^2 = 0.99) \qquad \textbf{(5.4)}$$

$$Abs_{@652nm} = 0.009\ln(x) + 0.337 \ (R^2 = 0.99) \quad \textbf{(5.5)}$$

$$PGM_{signal} = 0.436\ln(x) + 16.40 \ (R^2 = 0.99) \quad \textbf{(5.6)}$$

The LOD was compared with the PSA ELISA kit which has been reported [40] to have the LOD of 0.50 ng.mL$^{-1}$ PSA (Biocell Biotechnol. Co., Ltd., Zhengzhou, China). The high loading of glucose into nanoliposomes allowed for high sensitivity on the PGM. High production of $H_2O_2$ for the signal amplification in case of the HRP and Pd|PdO system, hence, low LOD values. The reported commercial human PSA ELISA used enzyme-antibody bioconjugate hence, higher LOD value as compared to values obtained in this work. The LOD of the immunosensor developed in here was also compared with other nanomaterials-based biosensors for the detection of PSA as shown in **Table 5.1.** The comparison table clearly shows that the sandwich immunosensors developed in this work have achieved both the low LOD$_s$ in femtograms per milliliter of PSA and a very wide linear concentration range (LCR). In addition, the use of PGMs in this study enabled the digitization of the acquisition of results which is a very high-end advantage over other nanomaterial-based biosensors for the detection of PSA.

**Table 5.1:** A comparison of different nanomaterials-based biosensors for the detection of PSA.

| Materials used | Sensing material | Linear concentration range | LOD | Refs |
|---|---|---|---|---|
| Multi-CAT-AuNP-Ab$_2$ | Colorimetric | 0.050 to 20 ng.mL$^{-1}$ | 0.03 ng.mL$^{-1}$ | [41] |
| Au-PSA-SPMB | Colorimetric | 0.10 to 100 ng.mL$^{-1}$ | 10 ng.mL$^{-1}$ | [42] |
| AuNP/PSA-CAT/MMP | Colorimetric | 1.0 pg.mL$^{-1}$ to 100 ng.mL$^{-1}$ | 1 pg.mL$^{-1}$ | [43] |
| SQA-Iron(iii) | Colorimetric | 1.0 pg.mL$^{-1}$ to 30 ng.mL$^{-1}$ | 0.5 pg.mL$^{-1}$ | [44] |
| Au@Cu | Colorimetric | 1.0 pg.mL$^{-1}$ to 1.0 µg.mL$^{-1}$ | 0.27 pg.mL$^{-1}$ | [45] |
| GENLs-anti-PSA-pAb | Colorimetric (HRP) | 0.10 fg.mL$^{-1}$ to 0.10 mg.mL$^{-1}$ | 0.050 fg.mL$^{-1}$ | TW |
| GENLs-anti-PSA-pAb | Colorimetric (Pd\|PdO) | 0.10 fg.mL$^{-1}$ to 0.10 mg.mL$^{-1}$ | 0.160 fg.mL$^{-1}$ | TW |
| GENLs-anti-PSA-pAb | Digital (PGM) | 0.10 fg.mL$^{-1}$ to 0.10 mg.mL$^{-1}$ | 0.250 fg.mL$^{-1}$ | TW |

**TW**: This work; **SQA**: squaric acid; **PSA-ACT**: Human prostate specific antigen complex; **MMP**: Magnetic microbeads; **AuNP**: Gold nanoparticles; **Au-PSA-SPMB**: Gold surface- PSA substrate peptide–magnetic beads.

**Multi-CAT-AuNP-Ab$_2$:** Polyclonal Goat Anti-Human PSA/Catalase-Labeled gold nanoparticles.

## 5.4. Conclusions

The glucose encapsulating liposomes were successfully prepared using two formulations labelled **F1** and **F2**. TEM images and DLS results showed spherical morphology with a mean diameter of 109 nm and 164 nm for lipid formulation **F1** and **F2** respectively. Horseradish peroxidase (HRP), Pd|PdO nanoparticles, and PGM were successfully used to quantify the formation of the D-glucose encapsulated in the liposomes and for the detection of PSA. The sandwich immunoassay was developed for the detection of PSA using GENLs-anti-PSA-pAb. The prepared GENLs-anti-PSA-pAb were evaluated for pH 5.0 and 1% Triton X controlled-release of the encapsulated D-glucose. The prepared GENLs from the formulation **F2** in this study have shown release at pH 5.0 or the use of 1% Triton X with high stability at pH 7.4. The sandwich immunoassay for the detection of PSA was further developed. The absorbance signal due to oxidized TMB at 652 nm showed a linear increase with an increase in the [PSA] when HRP or Pd|PdO nanoparticles were used. The PGM signal also showed a linear increase in digital values for glucose release from the liposomes and related to the PSA concentrations. The limits of detection were calculated to be 0.050 $fg.mL^{-1}$, 0.060 $fg.mL^{-1}$, and 0.10 $fg.mL^{-1}$ for HRP, Pd|PdO nanoparticles and PGM; respectively. This study demonstrated successfully, the preparation of immunoliposomes for pH and surfactant release of encapsulated glucose. The developed immunosensor also showed good detection of PSA using sandwich immunoassays.

## 5.5 References


[1] P.B. Luppa, C. Müller, A. Schlichtiger, H. Schlebusch, Point-of-care testing (POCT): Current techniques and future perspectives, TrAC - Trends Anal. Chem. 30 (2011) 887–898.

[2] W. Jung, J. Han, J.W. Choi, C.H. Ahn, Point-of-care testing (POCT) diagnostic systems using microfluidic lab-on-a-chip technologies, Microelectron. Eng. 132 (2014) 46–57.

[3] R. Guo, Y. Wang, S. Yu, W. Zhu, F. Zheng, W. Liu, D. Zhang, J. Wang, Dual role of hydrogen peroxide on the oxidase-like activity of nanoceria and its application for colorimetric hydrogen peroxide and glucose sensing, RSC Adv. 6 (2016) 59939–59945.

[4] Y. Tao, M. Li, B. Kim, D.T. Auguste, Incorporating gold nanoclusters and target-directed liposomes as a synergistic amplified colorimetric sensor for HER2-positive breast cancer cell detection, Theranostics. 7 (2017) 899–911.

[5] R. Ren, G. Cai, Z. Yu, D. Tang, Glucose-loaded liposomes for amplified colorimetric immunoassay of streptomycin based on enzyme-induced iron(II) chelation reaction with phenanthroline, Sensors Actuators, B Chem. 265 (2018) 174–181.

[6] R.A. Dorledo de Faria, L.G. Dias Heneine, T. Matencio, Y. Messaddeq, Faradaic and non-Faradaic electrochemical impedance spectroscopy as transduction techniques for sensing applications, Int. J. Biosens. Bioelectron. 5 (2019) 29–31.

[7] J.S. Daniels, Label-free impedance biosensors: opportunities and challenges, Electroanalysis. 19 (2008) 1239–1257.

[8] J. Tang, Y. Huang, H. Liu, C. Zhang, D. Tang, Novel glucometer-based immunosensing strategy suitable for complex systems with signal amplification using surfactant-responsive cargo release from glucose-encapsulated liposome nanocarriers, Biosens. Bioelectron. 79 (2016) 508–514.

[9] J. Cecchetto, F.C.B. Fernandes, R. Lopes, P.R. Bueno, The capacitive sensing of NS1 Flavivirus biomarker, Biosens. Bioelectron. 87 (2017) 949–956.

[10] A. Ebrahimi, P. Dak, E. Salm, S. Dash, S. V. Garimella, R. Bashir, M.A. Alam, Nanotextured superhydrophobic electrodes enable detection of attomolar-scale DNA concentration within a droplet by non-Faradaic impedance spectroscopy, Lab Chip. 13 (2013) 4248–4256.

[11] C.C. Liu, Electrochemical based biosensors, Biosensors. 2 (2012) 269–272.

[12] N.E. Stein, H.V.M. Hamelers, G. van Straten, K.J. Keesman, Effect of toxic components on microbial fuel cell-polarization curves and estimation of the type of toxic inhibition, Biosensors. 2 (2012) 255–268.

[13] J.E. Oliveira, L.H.C. Mattoso, E.S. Medeiros, V. Zucolotto, Poly(lactic acid)/carbon nanotube fibers as novel platforms for glucose biosensors, Biosensors. 2 (2012) 70–82.

[14] B. Lin, D. Liu, J. Yan, Z. Qiao, Y. Zhong, J. Yan, Z. Zhu, T. Ji, C.J. Yang, Enzyme-Encapsulated Liposome-Linked Immunosorbent Assay Enabling Sensitive Personal Glucose Meter Readout for Portable Detection of Disease Biomarkers, ACS Appl. Mater. Interfaces. 8 (2016) 6890–6897.

[15] J. Joo, D. Kwon, H.H. Shin, K.H. Park, H.J. Cha, S. Jeon, A facile and sensitive method for detecting pathogenic bacteria using personal glucose meters, Sensors Actuators, B Chem. 188 (2013) 1250–1254.

[16] M. Pohanka, Point-of-Care Diagnoses and Assays Based on Lateral Flow Test, Int. J. Anal. Chem. 2021 (2021) 6685619 (1-9).

[17] Y. Xiang, Y. Lu, An invasive DNA approach toward a general method for portable quantification of metal ions using a personal glucose meter, Chem. Commun. 49 (2013) 585–587.

[18] J.R. Choi, Development of Point-of-Care Biosensors for COVID-19, Front. Chem. 8 (2020) 517-527.

[19] W. Guo, T. Lee, J. Sudimack, R.J. Lee, Receptor-Specific Delivery of Liposomes Via Folate-Peg-Chol, J. Liposome Res. 10 (2000) 179–195.

[20] C.I. Nkanga, R.W. Krause, X.S. Noundou, R.B. Walker, Preparation and characterization of isoniazid-loaded crude soybean lecithin liposomes, Int. J. Pharm. 526 (2017) 466–473.

[21] V. Van Tran, J.Y. Moon, Y.C. Lee, Liposomes for delivery of antioxidants in cosmeceuticals: Challenges and development strategies, J. Control. Release. 300 (2019) 114–140.

[22] C.H.A. Boakye, K. Patel, R. Doddapaneni, A. Bagde, S. Marepally, M. Singh, Novel amphiphilic lipid augments the co-delivery of erlotinib and IL36 siRNA into the skin for psoriasis treatment, J. Control. Release. 246 (2017) 120–132.

[23] A.A. Yetisgin, S. Cetinel, M. Zuvin, A. Kosar, O. Kutlu, Therapeutic Nanoparticles and Their Targeted Delivery Applications, Mol. . 25 (2020) 2193-2225.

[24] J.J. Sudimack, W. Guo, W. Tjarks, R.J. Lee, A novel pH-sensitive liposome formulation containing oleyl alcohol, Biochim. Biophys. Acta - Biomembr. 1564 (2002) 31–37.

[25] H. Ibaraki, T. Kanazawa, C. Oogi, Y. Takashima, Y. Seta, Effects of surface charge and flexibility of liposomes on dermal drug delivery, J. Drug Deliv. Sci. Technol. 50 (2019) 155–162.

[26] J. Liang, J. Wang, L. Zhang, S. Wang, C. Yao, Z. Zhang, Glucose oxidase-loaded liposomes for: In situ amplified signal of electrochemical immunoassay on a handheld pH meter, New J. Chem. 43 (2019) 1372–1379.

[27] L. Shayne, T.K. Omatsu, S.M. Ohammadi, M.M. Aeki, A.I. Shida, H.T. Ani, M.T. Okeshi, Peroxidase-based Assays, 32 (2016) 815–818.

[28] Immunochemistry Technologies LLC, HRP Redox Reaction Driven TMB Color Development, (2020). https://immunochemistry.com/educational-material/hrp-redox-reaction-driven-tmb-color-development/. (Date accessed 01/01/2022).

[29] H. Lu, L. Zhang, J.H. Zhong, H.G. Yang, Partially Oxidized Palladium Nanodots for Enhanced Electrocatalytic Carbon Dioxide Reduction, Chem. - An Asian J. 13 (2018) 2800–2804.

A. Dickey, R. Faller, Examining the contributions of lipid shape and headgroup charge on bilayer behavior, Biophys. J. 95 (2008) 2636–2646.

[30] I.M. Hafez, P.R. Cullis, Cholesteryl hemisuccinate exhibits pH sensitive polymorphic phase behavior, Biochim. Biophys. Acta - Biomembr. 1463 (2000) 107–114.

[31] S.V. Markandeyaa, C. Sridhara, R.K. Babub, S.B. Diwakarc, B. Yamajalad, Synthesis and characterization of Glucosamine stabilized Palladium (Pd0) nanoparticles as efficient catalyst for reduction of nitro arenes. SMC Bulletin. 9 (2018) 103-109.

[32] M. Muniz-Miranda, A. Zoppi, F. Muniz-Miranda, N. Calisi, Palladium oxide nanoparticles: Preparation, characterization and catalytic activity evaluation, Coatings. 10 (2020) 207-217.

[33] A. Bin Yousaf, M. Imran, M. Farooq, P. Kasak, Interfacial Phenomenon and Nanostructural Enhancements in Palladium Loaded Lanthanum Hydroxide Nanorods for Heterogeneous Catalytic Applications, Sci. Rep. 8 (2018) 1–9.

[34] M. Muniz-Miranda, F. Muniz-Miranda, S. Caporali, N. Calisi, A. Pedone, SERS, XPS and DFT investigation on palladium surfaces coated with 2,2′-bipyridine monolayers, Appl. Surf. Sci. 457 (2018) 98–103.

[35] Y. Sun, J. Liu, N. Yang, Y. Zhu, One-Dimensional Heterostructured Palladium Oxide-Cobalt Oxide Catalyst for the Catalytic Oxidation of Methane, ChemCatChem. 9 (2017) 738–745.

[36] R.W. Bally, T.C.J. Gribnau, Some Aspects of the Chromogen 3,3',5,5'-Tetramethylbenzidine as Hydrogen Donor in a Horseradish Peroxidase Assay, Clin. Chem. Lab. Med. 27 (1989) 791–796.

[37] A. Shrivastava, V. Gupta, R. Article, Methods for the determination of limit of detection and limit of quantitation of the analytical methods, Chronicles Young Sci. 2 (2011) 21–25.

[38] D. Mwanza, S. Mvango, S. Khene, T. Nyokong, P. Mashazi, Exploiting Click Chemistry for the Covalent Immobilization of Tetra (4-Propargyloxyphenoxy)

Metallophthalocyanines onto Phenylazide-Grafted Gold Surfaces, Electrochim. Acta. 254 (2017) 89–100.

[39] Z. Gao, L. Hou, M. Xu, D. Tang, Enhanced Colorimetric Immunoassay Accompanying with Enzyme Cascade Amplification Strategy for Ultrasensitive Detection of Low-Abundance Protein, Sci. Rep. 4 (2015) 1–8.

[40] Z. Gao, M. Xu, L. Hou, G. Chen, D. Tang, Magnetic bead-based reverse colorimetric immunoassay strategy for sensing biomolecules, Anal. Chem. 85 (2013) 6945–6952.

[41] G.A.R.Y. Suaifan, C. Esseghaier, A. Ng, M. Zourob, Ultra-rapid colorimetric assay for protease detection using magnetic nanoparticle-based biosensors, Analyst. 138 (2013) 3735–3739.

[42] C. Cao, X. Li, J. Lee, S.J. Sim, Homogenous growth of gold nanocrystals for quantification of PSA protein biomarker, Biosens. Bioelectron. 24 (2009) 1292–1297.

[43] W. Lai, D. Tang, J. Zhuang, G. Chen, H. Yang, Magnetic bead-based enzyme-chromogenic substrate system for ultrasensitive colorimetric immunoassay accompanying cascade reaction for enzymatic formation of squaric acid-iron(III) chelate, Anal. Chem. 86 (2014) 5061–5068.

[44] Y. Liu, Z. Zhang, J. Yu, J. Xie, C.M. Li, A concentration−dependent multicolor conversion strategy for ultrasensitive colorimetric immunoassay with the naked eye, Anal. Chim. Acta. 963 (2017) 129–135.

# CHAPTER 6

# 6. Discussions

## 6.1 Electrografting of isophthalic acid monolayer and covalent attachment of antibody onto carbon surfaces: construction of capacitive biosensor for methotrexate detection

### 6.1.1. Synthesis of 5-diazoium tetrafluoroborate isophthalic acid salt (5-DIPA) from 5-aminoisophthalic acid (5-AIPA).

The synthesis protocol for 5-DIPA from 5-AIPA was carried out following the reaction scheme shown in **Scheme 3.1**. The successful synthesis of 5-DIPA was characterized using the FT-IR (**Fig. 3.1**) and $^{1}H$ NMR (**Fig. 3.2**). The convention of the amino functional group to the diazonium functional group ($-N\equiv N^{+}$) was observed by the appearance of the vibrational band at 2270 $cm^{-1}$. The successful formation of the diazonium salt did not affect the carboxylic groups. This was observed by the dominant presence of the carbonyl C=O vibrational bands at 1700 $cm^{-1}$ for both the product and starting material. The proton NMR showed the presence of the singlet peak at 7.73 ppm and a triplet peak at 7.93 integrating to 2 and 1 protons respectively. This confirmed the successful synthesis of the 5-DIPA with high purity.

### 6.1.2. Electrode modification

#### 6.1.2.1. Electrografting of 5-DIPA onto GCE and SPCE

Glassy carbon and screen-printed carbon electrode were both modified by electrografting of 5-DIPA using CV as shown in **Fig. 3.3**. For GCE, two reduction peaks at around +0.30 and -0.25 V were observed due to the radical generation and attachment onto the electrode surface respectively. The two reduction peaks disappeared during the second scan due to the passivation of the conducting electrode surface. A similar trend was observed during the electrografting of the SPCE with 5-DIPA. This trend confirmed the electrografting of 5-DIPA on both the GCE and the SPCE.

The surface coverage of IPA on the GCE and the SPCE electrode surfaces were calculated using **Eq. (3.5)** and they were found to be $\Gamma_{IPA} = 3.82 \times 10^{-12}$ mol.cm$^{-2}$ and $\Gamma_{IPA} = 1.17 \times 10^{-11}$ mol.cm$^{-2}$ respectively. These surface coverage values were found to be much smaller indicating the formation of the thin monolayer film due to the blocking effect of the carboxylic acid groups on position 1 and 3 of the diazonium salt used. The formation of a thin monolayer film was important for the development of the highly sensitive capacitive immunosensor for the detection of MTX.

The electrografted electrodes were both functionalized with the anti-MTX monoclonal antibodies using carbodiimide chemistry. To confirm the successful functionalization of the antibodies onto the IPA grafted monolayer, XPS (**Fig. 3.5** and **Fig 3.6**) was used. The carboxylic acid component at 289.3 eV (5.6%) on the bare GC was observed to increase to14.8 % on the GC-IPA surface which further increased after the formation of GC-IPA-anti-MTX-pAb. The increase of the carbonyl (C=O) component indicated the successful electrografting and the subsequent immobilization of the anti-MTX-pAb to form GC-IPA-anti-MTX-pAb surface. The O 1s analysis showed that there was an increase of the component at 532.7 eV after the immobilization of the anti-MTX-pAb due to the presence of the amide and the peptide bond on the anti-MTX-pAb. The N 1s was characterized by the increase in the intensity of the peaks. This was attributed to the presence of the amino acids and the peptide bonds on the anti-MTX-pAb.

### 6.1.2.2. Molecular docking and molecular dynamics simulation conformational analysis

Molecular docking and molecular dynamics simulation conformational analysis were used to study the conformational behaviour of the anti-methotrexate monoclonal antibody (apo protein before and after binding to the methotrexate (ligand). The crystal structure antibody-MTX had a good binding affinity between the anti-MTX monoclonal antibody and the MTX with a docking score of -8.207 kcal.mol$^{-1}$. This was due to the strong hydrophobic and pi-pi interactions between the MTX pteridine ring and the anti-MTX antibody heavy chain residue (**Fig.3.7 (a)).** Furthermore, the simulations revealed that the antibody showed the high radius of gyration (a measure of structural conformation). The radius of gyration (Rg) of the antibody was observed to reduce in the presence of the ligand MTX due to the interaction between the protein and the ligand (**Fig. 3.7(c)(ii)**). The compact antibody-MTX formed. The changes in

the Rg confirmed the structural conformation changes that occur when the MTX interacts with the anti-MTX polyclonal antibody. The simulated structural conformational changes indicated that there would be electrochemical capacitive changes during the interaction of the MTX and the anti-MTX on the immunosensing electrode surface, resulting in the highly sensitive and selective capacitive detection of MTX on the immunosensor GCE/SPCE-IPA-anti-MTX-pAb.

#### 6.1.2.3 Detection of MTX using modified GCE/SPCE-IPA-anti-MTX-pAb|BP

The detection of MTX was done using non-Faradaic electrochemical impedance spectroscopy. The EIS raw data was analysed using SVD to elucidate the changes in capacitance due to changes in the structural conformations of the anti-MTX-pAb on the immunosensor before and after binding. The score plots (**Fig. 3.8** and **3.9**) of the imaginary vs the real, u (1), showed clusters of MTX scores separated from the PhB alone. This was attributed to the high selective and specific interaction between the MTX and the anti-MTX antibody. The separation of the MTX spiked PhB and the PhB alone (blank) was observed to be higher on the SPCE than that on the GCE due to increased surface area on the SPCE which increases the number of binding sites for MTX. The effect of the blocking on the selectivity and specificity of the MTX-anti-MTX antibody interaction was studied (**Fig. 3.10**). The score plots obtained on the immunosensor without the blocking polymer showed no separation between the MTX scores and the blank due to the presence of unspecific binding of the MTX to the antibodies. Therefore, the blocking polymer (BP) was used to improve the specificity and the selectivity of the immunosensor towards MTX.

The calibration curves in **Fig. 3.11(a,b)** generated using the principle component analysis showed $R^2$ of 0.99 for both GCE-IPA-anti-MTX-pAb|BP and SPCE-IPA-anti-MTX-pAb|BP due to excellent correlation between the measured MTX concentration and the predictions. The $R^2$ of 0.99 indicated decrease in the relative error as compared to the reported studies. The decrease in the relative error is attributed to the formation of the thin film monolayer that improved the sensitivity of the immunosensor towards the capacitive detection of MTX. The LOD where found to be 7.0 $pmol.L^{-1}$ and 5.5 $pmol.L^{-1}$ for GCE-IPA-anti-MTX-pAb|BP and SPCE-IPA-anti-MTX-pAb|BP respectively. The lower limits of detection indicated the high sensitivity and selectivity of the immunosensors developed.

## 6.2 Label-free capacitive immunosensor based on a stable thin-film monolayer of isophthalic acid for detection of prostate-specific antigen

### 6.2.1 Electrografting of 5-DIPA onto gold electrode

The electrografting of 5-DIPA was also done on the gold electrode for the development of the label-free capacitive immunosensor based on a stable thin-film monolayer of isophthalic acid for detection of prostate-specific antigen (PSA). The passivation of the gold electrode conducting surface was monitored by the gradual decrease in the reduction peak (**Fig. 4.1**) at 0.13 V till it reached constant during electrografting. The electroreduction response (ERR%) showed the plateau (**Fig. 4.1(b)**) of the electroreduction of the diazonium salt indicating that no grafting was taking place at the plateau although electroreduction was occurring. This confirmed the non-occurrence of the multilayer formation due to the blocking of the radical attachment at position 1 and 3 of the diazonium moiety. The IPA monolayer on the gold electrode surface showed a high pH response. This was observed by the decrease in both the peak current and the increase in the peak-to-peak separation at pH 7.0 and pH 8.0 while showing the opposite trend at pH 4.0. Because the pKa (3.69) of the IPA layer is much lower than pH 7.0 and pH 8.0 hence, deprotonation occurred forming $COO^-$ which then repel the negatively charged $[Fe(CN)_6]^{3-/4-}$redox probe (**Fig. 4.2 (a)**). The monolayer of IPA was used as the anchoring layer for the immobilization of the anti-PSA antibodies as shown in (**Scheme 4.1**). The characterization of the gold modified surface was studied using cyclic voltammetry (CV), electrochemical impedance spectroscopy (EIS) and X-ray photoelectron spectroscopy (XPS). After the formation of the immunosensor (AuE-IPA-anti-PSA-mAb|BSA), both the CV and EIS showed that the immobilization of the anti-PSA antibodies onto the IPA monolayer was successful. This was noticed by the observed increase in both the peak-to-peak separation and the charge transfer resistance from the IPA monolayer to the immunosensor at pH 7.0 as shown in **Table 4.1**.

### 6.2.2 XPS analysis of the AuE-IPA and AuE-IPA-anti-PSA-mAb|BSA surfaces

The XPS survey spectrum of the electrografted gold electrode (AuE-IPA) (**Fig.4.4 (i)**) showed the persistent presence of the peaks due to gold (Au 4f, Au 4p and Au 4d) indicating the IPA

monolayer formed was an ultrathin film. The subsequent immobilization of the anti-PSA antibodies onto the IPA monolayer via the carbodiimide chemistry showed the drastic disappearance of the peaks due to gold indicating the successful immobilization of the anti-PSA antibodies.

The high resolution core-level XPS analysis of the C 1s showed the presence of the gold-carbon (Au-C) peak at 284.4 eV indicating the successful electrografting of the ultrathin monolayer of IPA onto the gold electrode. After immobilization of the anti-PSA monoclonal antibody on the AuE-IPA surface, the O 1s high resolution spectra (**Fig. 4.5 (b')**) showed the components due to O-H (72.4%), C-O (19.2%), and O=C (8.5%) were observed to increase in intensity by 10 folds indicating an increased amount of carbonyl groups due to the amino acid groups on the anti-PSA monoclonal antibodies. The N 1s high resolution analysis showed components due to N-H (398.1 eV) and $N^+$ (402.6 eV) accounting for the presence of the amino groups due to the anti-PSA antibodies present on the AuE-IPA-anti-PSA-mAb|BSA surface. The changes in the N 1s in **Fig. 4.5(b")** showed chemical environment from that of the AuE-IPA ($N_2$) to the AuE-IPA-anti-PSA-mAb (N-C, $N^+$, and N-H) further confirmed the successful immobilization of the anti-PSA monoclonal antibody on the AuE-IPA via the EDC/NHS chemistry.

### 6.2.3 Capacitive detection of PSA

Prior to the analytical performance studies of the developed label-free capacitive immunosensor based on a stable thin-film monolayer of isophthalic acid for detection of PSA, the number of cyclic voltammograms for electrografting of IPA; the amount of the anti-PSA antibodies immobilized and the time of incubation of the AuE-IPA-anti-PSA-mAb|BSA were optimized.

#### 6.2.3.1 Optimisation of the assay parameters for the detection of PSA

The non-Faradaic electrochemical capacitance ($C_{nFC}$) calculated as shown in **Eq. 4.5** and **4.6** was used as a measure for the determination of the optimal parameters for the construction of the immunosensor. **Table 6.1** shows the summary of the optimized conditions.

**Table 6.1:** Summary of the optimized conditions for the fabrication of PSA immunosensor, AuE-IPA-anti-PSA-mAb|BSA

| Parameter | Initial condition | Studied range | Optimal value |
|---|---|---|---|
| CV scans | 4 scans | 4 to 24 scans | 20 scans |
| Amount of anti-PSA-mAb | 5.0 µg.mL$^{-1}$ | 5 to 30 µg.mL$^{-1}$ | 20 µg.mL$^{-1}$ |
| Incubation time | 3 min | 3 to 21 min | 15 min |

### 6.2.3.2 Detection of PSA using the Nyquist plots of complex capacitance (C'' vs C')

To detect PSA using the Nyquist plots of complex capacitance (C'' vs C'), the acquired non-Faradaic EIS data (**Fig. 4.8 (a)**) was converted to the capacitance plane in Matlab using **Eq. (4.5)** and **(4.6)**. The plots of C'' vs C' (**Fig. 4.7 (b)**) showed that the semicircle representing the total capacitance before incubation in PSA concentration ($C_{PBS}$) was wider than the semicircle after incubation ($C_{PSA}$) of the immunosensor in PBS containing 10.0 fg.mL$^{-1}$ of PSA. The decrease in the semicircle (capacitance) was attributed to the binding of PSA to the $PSA_{Ab}$ on the electrode. The analytical performance was studied using the relative response percentage (RR%) shown in **Eq. (4.7)** and was used to construct a linear curve against PSA concentration range from 10.0 fg.mL$^{-1}$ and 0.10 mg. mL$^{-1}$. The LOD and LOQ were calculated to be 2.3 fg.mL$^{-1}$ and 7.6 fg.mL$^{-1}$ with $R^2 = 0.99$. The value of $R^2$ is much closer to 1 indicating the low relative error making this method more reliable.

### 6.2.3.3 Detection of PSA using the complex capacitance

With an assumption that the immunosensor behaves like a super capacitance, then the capacitance is only affected by the imaginary part of impedance. The relationship between the complex capacitance and the imaginary part of impedance was shown in **Eq. (4.9)**. This relationship was used to convert the imaginary part of impedance to the complex capacitance. The plot of complex capacitance data versus log of frequency was shown in **Fig. 4.9**. The capacitance was observed to decrease linearly with an increase in the PSA concentration due to the binding of the PSA antigen to the immobilized anti-PSA-mAb antibody immobilized on the electrode surface. The RR% was also used to measure the analytical performance (**Fig.**

**4.9(b)**) and it showed a linear curve against PSA concentration ranging from 10.0 fg.mL$^{-1}$ to 0.10 mg.mL$^{-1}$. The limit of detection was calculated to be 7.6 fg.mL$^{-1}$ with the $R^2$ of 0.99. The increase in the LOD as compared to the previously discussed method in *Section 6.2.3.2* was an indication of the introduction of the error due to the assumption that the sensing platform formed a perfect capacitor. However, the method is still reliable as it has also shown that it can detect PSA at a wide concentration range with its LOD in femtograms per milliliter.

#### 6.2.3.4 Detection of PSA using the Randles circuit ($R_SC$) fitting

With the assumption made above, the Randles circuit fitting of the circuit comprising of a solution resistance and a capacitance as double layer capacitance connected in series was also used to assess the analytical performance of the immunosensor towards the capacitive detection of PSA. In this case, the capacitance data was collected directly from the fitted and simulated $R_SC$ circuit and it was observed that there was a linear decrease in the capacitance with an increase in the logarithmic concentration of PSA as shown in **Fig. 4.10(a)**. The limit of detection was calculated from the RR% vs [PSA] in **Fig. 4.10(b)** and it was found to be 3.3 fg.mL$^{-1}$ with the $R^2$ value of 0.99. Many studies have claimed difficulties with using the circuit fitting model for monitoring capacitance changes during non-Faradaic EIS detection. Therefore, the successful use of this system in this study indicates a great achievement in the development of affinity-based EIS immunosensors for both anticancer drugs and cancer bioanalytes.

## 6.3. Ultrasensitive detection of prostate-specific antigen using glucose-encapsulated nanoliposomes anti-PSA polyclonal antibody as detection nanobioprobes

### 6.3.1. Synthesis of oleylamido-4-butanoic acid (OABA)

The synthesis protocol for OABA was carried out following the reaction scheme shown in **Scheme 5.1**. The successful synthesis of OABA was characterized using FT-IR (**Fig. 5.1**) and $^1$H NMR (**Fig. 5.2**). The conversion of the amino functional group to the amide group (O=C-

NH) was observed by the appearance of the vibrational bands at 3301 $cm^{-1}$ and 1533 $cm^{-1}$. The successful formation of the product was also observed by the splitting carbonyl (C=O) vibrational bands into two, one for the amide (1634 $cm^{-1}$) and the other for the carboxylic acid (1688 $cm^{-1}$). The proton NMR showed the presence of four new peaks between 1.95-1.97 ppm due to C-H of the attached succinate moiety. Moreover, a triplet peak at 5.88 ppm integrating to one proton was assigned to the N-H due to the amide bond formed. This confirmed the successful synthesis of OABA and the absence of foreign peaks indicated its high purity. OABA was then used as one of the lipids in preparation of glucose encapsulated liposomes mainly for the introduction of the carboxylic acid group for the covalent attachment of the anti-PSA polyclonal antibodies via EDC/NHS coupling.

### 6.3.2. Characterization of glucose-encapsulated nanoliposomes (GENLs)

GENLs were prepared using two formulations, **F1** and **F2** and were characterized using DLS (**Fig. 5.3(a)**) which showed that the liposomes had a diameter of 109 nm and 164 nm respectively with a polydispersity index of 0.2 indicating that the liposomes were highly monodispersed. The TEM images in **Fig. 5.3(b)** showed that the liposomes were spherical and their individual particle sizes were ranging from 150-200 nm. GENLs for **F2** were found to be bigger than the **F1** because the CHEMS in **F2** provided a larger cross-sectional surface area due to the presence of the negatively charged carboxylic groups and the extra carbon chain length from the succinate moiety contributed to the increase in the size of the **F2** GENLs.

The stability of GENLs at different pH values ranging from pH 7.5 to pH 5.0. UV-vis absorption spectra in **Fig. 5.6(a)** showed that the absorbance decreased with increasing pH. At pH 5.0, the UV-vis spectra recorded the highest absorbance indicating the maximum disruption of liposomes at pH 5.0 while being stable at pH 7.5 which recorded the lowest. The stability of the GENLs at different pH values was further studied using DLS and TEM (**Fig. 5.7**). The GENLs at pH 6.5 to pH 5 showed increased size on DLS and aggregation on TEM images indicating the instability of GENLs at these pH values. Whilst, the DLS and TEM images of GENLs at pH 7.5 showed no changes in both the size on DLS and aggregation on TEM images, indicating that they were highly stable at this pH.

### 6.3.3 Confirmation of D-glucose encapsulation

The confirmation of D-glucose encapsulation in nanoliposomes was done using colorimetric reaction involving HRP or Pd|PdO reacting with TMB to produce a blue coloured product whose intensity was measured on UV-vis spectrometer. The personal glucose meter was also used to quantitatively determine the D-glucose encapsulation. The GENLs were lysed by using Triton-X 100 or PBS pH 5.0 in the presence of TMB, GOx and HRP resulting in a blue colour change. The blue colour was due to the oxidation of TMB in the presence of hydrogen peroxide produced from the oxidation of the released glucose. The hydrogen peroxide oxidized the HRP to HRP(+5) which gets reduced to HRP(+3) and oxidizes TMB to TMBDI (blue product). The produced blue colour product show absorption at 652 nm under UV-vis and the absorption was used to confirm the encapsulation of D-glucose in **Fig. 4.5 (a)**. The same UV-vis procedure was used to compare the amount of glucose encapsulated in the **F1** and **F2** GENLs. **Figure 5.4(b)** showed that **F2** had a higher intensity in absorbance than **F1** GENLs indicating that **F2** GENLs had a higher amount of D-glucose encapsulated due to their bigger size. Thereafter, the **F2** GENLs were further used for the development of the sandwich immunoassay for the detection of PSA.

The encapsulation efficiency was calculated using **Eq. (5.1)** and was found to be 60% translating to about 1.7 mg per 1 mg of the liposomal lipids. The quantification of the encapsulated D-glucose was also done using the personal glucose meter (**Fig. 5.8**). An aliquot of the GENLs at pH 5.0 and pH 7.4 was placed on the measuring strip on the personal glucose meter. The aliquot at PBS pH 5.0 showed a reading of 5.5 $mmol.L^{-1}$ indicating the successful release of D-glucose due to lysis of GENLs at pH 5.0. The one at PBS (pH 7.4) gave ununderfined read-out indicating that the liposomes remained intact at pH 7.4.

### 6.3.4 Bioconjugation of anti-human PSA polyclonal antibody to the GENLs

DLS (**Fig. 5.9**) showed a 26 nm increase in diameter of GENLs suggesting successful bioconjugation of anti-PSA antibodies. This was further confirmed by the changes in surface charge which decreased in negativity from -30 ± 5 mV for GENLs to -5 ± 2 mV indicating the

presence of the anti-PSA polyclonal antibodies on the GENLs surfaces yielding GENLs-anti-PSA-pAb.

### 6.3.5 Characterization of Pd|PdO nanoparticles

The Pd|PdO nanoparticles were characterized using UV-vis (**Fig. 5.10(a)**); DLS (**Fig. 5.10(b)**); TEM (**Fig. 5.10(c)** and **(d)**) and XPS (**Fig. 5.11**). The UV-vis characterisation showed the disappearance of the absorption peak at 483 nm after the reduction of the palladium (II) chloride to form the palladium nanoparticles indicating the conversion of the $Pd^{2+}$ to $Pd^{0}$. DLS spectrum of the Pd|PdO nanoparticles showed hydrodynamic average radius of 8 ± 0.5 nm with a polydispersity index (PDI) of 0.11. This was confirmed with the TEM micrograph which showed that the Pd|PdO nanoparticles had a mean width of 7.0 ± 1.6 nm, hence confirming the successful formation of the Pd|PdO nanoparticles. The chemical composition of the formed Pd|PdO nanoparticles was studied using XPS analysis. The peaks obtained at 335.2 eV and 340.5 eV corresponded to the formation of the palladium nanoparticles ($Pd^{0}$). Other peaks at 335.7 eV and 341.4 eV correspond to the presence of the $Pd^{2+}$. The occurrence of the peaks due to $Pd^{0}$ was clear indication of the formation of the nanoparticles. However, the surface of these nanoparticles showed the presence of $Pd^{2+}$ which was an indication of surface oxidation. This was further confirmed by the occurrence of the peaks due to different oxygen species at 528.8.6 eV ($O^{2-}$) and 533.4 eV (-OH). Hence, confirming the formation of the Pd|PdO nanoparticles.

### 6.3.6. Detection of prostate-specific antigen (PSA)

#### 6.3.6.1 Optimisation of D-glucose release and reaction time for the PSA colorimetric detection

The reaction time of the HRP and Pd|PdO nanoparticles towards the colorimetric detection of PSA was investigated (**Fig. 5.12**). There was an increase in the absorbance with an increase in time of response for both HRP and Pd|PdO nanoparticles. However, the Pd|PdO nanoparticles

showed a faster response than the HRP in terms of their peroxidase-like activity. The optimum reaction pH of the acetate buffer used for the detection of PSA using the Pd|PdO nanoparticles was found to be pH 4.0. **Table 6.2** showed the summary of the optimized conditions for the detection of PSA in a sandwich immunoassay.

**Table 6.2:** Summary of the optimized conditions for the performance of the HRP and Pd|PdO toward their peroxidase-like activity.

| **Parameter** | **Initial condition** | **Studied Range** | **Optimal value** |
|---|---|---|---|
| Time of HRP response | 15 min | 15 to 35 min | 30 min |
| Time of Pd\|PdO response | 5 min | 5 to 25 | 20 min |
| pH of acetate buffer | 3 | 3 to 8 | 4 |

### 6.3.6.2 Quantitative detection of PSA

The use of GENLs for the quantitative detection of PSA was studied in combination with HRP in **Fig. 5.13(a)**, Pd|PdO nanoparticles in **Fig. 5.13(b)** and PGM in **Fig. 5.13(c)**. For colorimetric detection of PSA, both HRP, Pd|PdO nanoparticles exhibited an increase in the absorption intensity with an increase in the logarithmic concentration of PSA from 0.10 $fg.mL^{-1}$ to 0.10 $mg.mL^{-1}$. This indicated that the absorption signal was dependent on the logarithmic concentration of PSA. The same trend was observed on the detection of PSA using PGM. The comparative study of the detection of PSA using GENLs in combination with HRP, Pd|PdO nanoparticles and PGM showed that limits of detection (LOD) were found to be 0.050 $fg.mL^{-1}$, 0.160 $fg.mL^{-1}$, and 0.250 $fg.mL^{-1}$ respectively. The use of Pd|PdO nanoparticles proved to be a viable substitute for HRP because it gave the LOD in the same range as that of HRP but at a faster reaction time. Whilst, PGM enabled the digitization of the acquisition of results which is a very high-end advantage over other nanomaterial-based biosensors for the detection of PSA. Also the use of PGM demonstrated their possible repurposing for PSA detection.

# CHAPTER 7

## 7. Conclusions and future perspectives

### 7.1 Conclusions

In this thesis, we presented a new protocol of surface modification following an electrografting method to form a thin monolayer film of 5-diazonium isophthalic acid (IPA) on glassy carbon electrode (GCE), screen-printed carbon electrode (SPCE), and gold electrode (AuE). The modified surfaces were activated with carbodiimide to immobilize anti-methotrexate (MTX) antibodies on carbon electrodes to yield GCE/SPCE-IPA-anti-MTX-pAb|BP. Whilst, the AuE was activated similarly and immobilized with the anti-PSA antibodies to yield AuE-IPA-anti-PSA-mAb|BSA. The stepwise modification and immobilization of antibodies on the electrode surfaces was confirmed by CV, EIS and XPS.

The electrografting of 5-DIPA on carbon electrodes showed complete passivation of the redox processes of the $[Fe(CN)_6]^{3-/4-}$. However, the surface coverage of the IPA thin monolayer film was found to be much lower when compared with literature confirming the formation of an ultrathin monolayer film. Unlike on carbon surfaces, the electrografting of the 5-DIPA on the gold electrode showed the gradual passivation of the conducting surface. This was attributed to the blocking of the formation of the thick multilayer due to the presence of the carboxylic acid functional groups at positions 1 and 3 of the diazonium moiety. The difference in the eletrografting behaviour between the carbon and gold electrode surface was that, gold surface showed gradual passivation attributed to the high conducting nature of gold as compared to carbon. CVs and EIS of $[Fe(CN)_6]^{3-/4-}$ on gold modified electrode showed a slight difference in the electron transfer rate between bare and the modified gold electrode. This was conclusive of the formation of an ultrathin monolayer film formed as confirmed by various experiments. Further confirmation of the formation of thin monolayer film was achieved by XPS. The XPS analysis showed the presence of the carbide (Au-C) along with the persisting peaks due to gold binding energy proving the successful electrografting of 5-DIPA onto the gold electrode and the formation of an ultrathin monolayer film.

The sensor surfaces containing anti-MTX-pAb antibodies were used for capacitive detection of methotrexate (MTX) while the one containing anti-PSA was used for capacitive detection of PSA. EIS data analysis for the capacitive detection of PSA was accomplished using SVD. The MTX interacted with the immobilized anti-MTX antibody leading to antibody conformation changes resulting in change in capacitance. Molecular dynamics confirmed the conformational changes of the anti-methotrexate antibody alone and after binding to the MTX. These conformational changes were observed electrochemically using sensitive impedance measurements for the detection of MTX. The changes in capacitance increased with increasing concentration of MTX for both GCE-IPA-anti-MTX-pAb and SPCE-IPA-anti-MTX-pAb showing a clear separation between the blank and phosphate buffer containing MTX. The $R^2$ (0.99) for analytical performance was found to have a lower relative error when compared to recent studies that applied SVD for capacitive biosensor. This shows improvement in the development of the immunosensing platform for the capacitive biosensors due to formation of ultrathin insulation monolayer.

The EIS data for the capacitive detection of PSA on gold electrode was achieved using Nyquist plots of capacitance generated from the complex impedance data; complex capacitance calculated from the imaginary part of the impedance plotted against the log of frequency; and capacitance as the double layer capacitance from the circuit fitting ($R_SC$). ). All the three data analysis techniques showed an excellent linear range between 10.0 $fg.mL^{-1}$ and 0.10 $mg.mL^{-1}$. The LOD was found to be 2.3 $fg.mL^{-1}$ ($R^2 = 0.99$), 7.6 $fg.mL^{-1}$ ($R^2 = 0.99$) and 3.3 $fg.mL^{-1}$ ($R^2 = 0.99$) for the Nyquist plots of capacitance, complex capacitance and capacitance from the circuit fitting (RsC) respectively. It was observed that the values of LODs acquired from respective method of EIS data analysis increased with respective assumptions made. Hence, it was concluded that the LODs were affected by the errors introduced by the assumptions. Thus, making the use of the complex capacitance Nyquist plots more favourable because no assumption was made, the total EIS data was converted to the total capacitance. However, this does not rule out the other two methods as they show comparable LODs too. The use of the circuit fitting model to monitor capacitive changes of a bioaffinity response was a great achievement in this thesis because this has been found to be very difficult by most research groups.

Therefore, capacitive detection of both MTX and PSA using electrografting of IPA as an anchoring block for the immobilization of the antibodies provided a much-needed solution to the challenge of a receptor immobilization in the development of biosensors for point-of-care testing devices. To the best of our knowledge, this method has been reported for the first time in this thesis. Furthermore, the robustness of the method was observed by the application of various EIS data treatment and analytical methods which gave comparable limits of detection with improved relative error indicating ultrasensitive, high selectivity and specificity.

The glucose encapsulating bioconjugated nanoliposomes were successfully prepared and characterized using DLS and TEM. Horseradish peroxidase (HRP), Pd|PdO nanoparticles, and PGM were successfully used to characterize the formation of the D-glucose encapsulating nanoliposomes for the detection of PSA. The prepared GENLs from the formulation **F2** in this study showed release of D-glucose at pH 5.0 or when 1% Triton X was used but showed high stability at pH 7.4. During the detection of PSA using the sandwich immunoassay, the absorbance of the oxidized TMB at 652 nm showed a linear increase with an increase in the [PSA] for HRP or Pd|PdO nanoparticles. The PGM signal also showed a linear increase in digital values for glucose-related to the PSA concentrations. The limits of detection were calculated and were found to be 0.05 $fg.mL^{-1}$, 0.06 $fg.mL^{-1}$, and 0.10 $fg.mL^{-1}$ for HRP, Pd|PdO nanoparticles and PGM respectively. This study demonstrated successfully the preparation of immunoliposomes for pH and surfactant release of encapsulated glucose. The use of liposomes as nanocarriers in combination with HRP, Pd|PdO nanoparticles and PGM is clearly an improvement in the colorimetric detection and digitization of PSA monitoring. Pd|PdO nanoparticles proved to be viable substitutes for expensive natural HRP with improved reaction time.

### 7.2 Future Perspectives

Both colorimetric and electrochemical detection designed in this thesis for PSA and MTX still requires the use of real samples and validation with clinical samples. Also the monitoring during the chemotherapy treatment would be vital.

- For MTX, the detection of compounds that have similar structure and sub-structure such as Folic acid (60% similarity), aminopterin (52% similarity), pralatrexate (65% similarity), and $N^{10}$-methyl-4-amino-4-deoxypteroic acid (66% similarity) is ongoing. The use of molecular dynamic simulations will be of major interest and used in the ongoing studies. In addition, the study using anti-MTX aptamers for aptasensor detection of MTX would be ideal to compare the sensitivity and specificity of the two biological molecules (aptamers and antibodies).
- The detection of PSA is a much needed milestone for the diagnosis of prostate cancer but due to its non-specificity there is a further need for the detection of total PSA, free-PSA and complex-PSA. The differences between the three biomarkers is crucial in the definitive diagnosis of prostate cancer. The use of ratio of free-PSA to complexed-PSA and use of threshold analysis will assist in determining the positive prostate cancer diagnosis for the benign prostate cancer diagnosis. The detection of other biomarkers for prostate cancer would also be investigated for multiplexed detection which will result in the definitive diagnosis. Molecular dynamics and simulation will be investigated for protein-protein (i.e. PSA and Antibody) interaction to elucidate the mode of their interactions.

Both of these studies are subject of our continued investigation towards the development of an affordable diagnostic device for the diagnosis of cancer and monitoring of effective chemotherapeutic treatment using MTX.